

The Effect of Moisture on the Granular Characteristics of Polymetallic Nodules in the Context of Bulk Handling

Offshore and Dredging Engineering

Floris Doorn 4390083

Tuesday 3rd May, 2022



The effect of moisture on the granular characteristics of polymetallic nodules in the context of bulk handling

by

Floris Doorn

to obtain the degree of Master of Science
at the Delft University of Technology,
to be defended publicly on Thursday May 12, 2022 at 10:00 AM.

Student number: 4390083

Thesis committee: Dr. ir. R. L. J. Helmons, TU Delft, supervisor
Dr. ir. D. L. Schott, TU Delft
Ir. E. De Hoog, TU Delft, Royal IHC

An electronic version of this thesis is available at <http://repository.tudelft.nl/>.



Abstract

In recent decades, a significant amount of the research into deep sea polymetallic nodule mining has been conducted on the collecting vehicle and the riser system accommodating transport from the seabed to the mining support vessel. The topside operation, however, is less commonly described in the literature. This part of the operation deserves attention because it significantly impacts project risk and cost.

After initial investigation the main research question was formed:

What is the effect of moisture on the granular characteristics of polymetallic nodules in the context of bulk handling?

Royal IHC provided a container with around 50 kg of polymetallic nodules from the Clarion Clipperton Zone. These nodules have been used in earlier research, focused on the degradation of nodules in transport from the seabed to the sea surface. Resulting in broken and damaged nodules. Therefore these are a good representation of nodules coming from the vertical transport system.

The degraded nodules provide a unique opportunity to gain an understanding of the bulk behavior of the nodules once they have arrived on the ship.

Four experimental setups were used to understand the granular characteristics of degraded polymetallic nodules in a non-destructive manner. In the first setup, particle properties such as density, porosity, and water content have been measured. The second setup identifies the shape of degraded nodules. The third setup measures the angle of repose for different nodule sizes and water content. The last setup measures the friction factor for different nodule sizes and water content, while changing the sliding surface between steel or rubber. Lastly, clay has been added to the sliding surface experiment.

Considering the angle of repose tests and the sliding and rolling friction angle, it is evident that the difference between dry and fully saturated nodules is minimal. For the friction angle: The maximum deviation between dry, saturated and CCZ clay is 8 % on steel and 9 % on rubber, corresponding to $\pm 2^\circ$. For the angle of repose, the difference between dry and saturated is negligible. It is concluded that the moisture content only contributes minimal level to bulk behaviour of nodules.

Preface

I would like to thank a number of people who have made it possible for me to present this master's thesis. First of all my daily supervisor Rudy Helmons, his weekly input has given me the structure to continue working every time. Secondly, I would like to thank Dingena Schott for her knowledge and enthusiasm at the progress meetings, and finally Edwin de Hoog for helping me obtain the nodules and for his keen eye during the progress meetings.

Apart from the TU Delft supervisors, I would like to thank Patty and Pauline for answering all my questions and planning all the meetings.

Lastly, I would like to thank my friends and family, who always have confidence in me.

F.A. Doorn
Delft, April 2022

Contents

Nomenclature	i
List of Figures	iii
List of Tables	vi
1 Introduction	1
1.1 Deep sea mining in general	1
1.2 Problem definition	4
1.3 Research questions	5
1.4 Outline of this thesis	5
2 Theory	7
2.1 Overview of the mining setup	7
2.1.1 Seafloor mining tool	9
2.1.2 Vertical transport system	9
2.1.3 Cleaning process and storage	11
2.1.4 Ship to ship transport	13
2.1.5 SWOE	14
2.2 Comparison of dewatering strategies	15
2.2.1 Sedimentation	15
2.2.2 Filtration	18
2.2.3 Thermal drying	21
2.2.4 Overview of dewatering strategy at sea	21
2.2.5 Dewatering on land or at sea	23
2.3 Effect of water on material properties	25
2.3.1 Solids in slurry	28
2.3.2 Granular behavior	29
2.3.3 Moisture in coarse granular material	32
2.4 Conclusion	37
3 Nodule properties	38
3.1 Polymetallic nodules sample	38
3.2 Density measurements	39
3.3 Methods	39
3.4 Results	40
3.5 Discussion	42
3.6 Conclusion and recommendation	43
4 Measuring particle shape	44
4.1 Methodology	44
4.2 Method	45
4.3 Results	46
4.4 Discussion	48
4.5 Conclusion and recommendations	48

5	Measuring the angle of repose	49
5.1	Introduction	49
5.2	Methods	49
5.3	Results	51
5.4	Discussion	51
5.5	Conclusion and recommendations	52
6	Measuring the sliding/rolling friction angle	53
6.1	Introduction	53
6.2	Methods	55
6.3	Results and discussion	60
6.4	Conclusion	69
7	Design implications	73
7.1	Storage & transport	73
8	Conclusion and recommendation	74
8.1	Theory	74
8.2	Experiments	75
8.3	main research question	76
	Appendix A Literature	78
	Appendix B Experimental methods	79
B.1	PSD and properties	79
B.2	Particle properties	80
B.3	Angle of repose	80
B.4	Rolling and sliding friction angle	84
B.4.1	Single nodule test	84
B.4.2	Bulk tests free	86
B.4.3	Confined bulk tests	87
B.4.4	Surface roughness measurements	88
B.4.5	Added mass tests	91
B.4.6	All tests combined	92
	Bibliography	94

Nomenclature

Acronyms

AR	Aspect Ratio
CCZ	Clarion Clipperton Zone
CT	Computed Tomography
DEM	Discrete Element Method
IOM	Interoceanmetal Joint Organization
MSV	Mining Support Vessel
NIOZ	Royal Netherlands Institute for Sea Research
PSD	Particle Size Distribution
SWOE	Sediment, Waste and Other Effluents
TML	Transportable Moisture Limit
TRL	Technology readiness level
VTs	Vertical Transport System

Greek Symbols

α	Angle of repose	[°]
μ	Coefficient of friction	[-]
ν_f	kinematic viscosity of the liquid	[m ² /s]
ψ	Shape correction factor	[-]
ρ_d	Dry nodule density	[g/cm ³]
ρ_l	Density liquid	[g/cm ³]
ρ_s	Specific nodule density (mineral density)	[g/cm ³]
ρ_w	Saturated nodule density (wet density)	[g/cm ³]
ρ_{mix}	Density slurry	[g/cm ³]
ρ_{situ}	Volumetric density	[g/cm ³]
σ'	Effective stress	[Pa]
σ_α	Normal stress	[Pa]
σ'_T	Stress	[Pa]
τ	Shear strength	[Pa]

τ_c	Cohesion of the bulk material	[Pa]
τ_s	Shear strength of the bulk material	[Pa]
θ	Sliding/rolling friction angle	[°]

Roman Symbols

C_D	Drag coefficient	[-]
c_m	The mass concentration	[-]
c_v	The volume concentration	[-]
d	Particle size	[m]
e	Void ratio	[-]
F_d	Drag force	[N]
F_f	Friction force	[N]
F_s	Static friction force	[N]
g	Gravitational acceleration	[m/s ²]
m_d	Mass of a nodule, without water	[g]
m_s	Mass of the particular solids	[g]
m_w	Mass of a nodule, including air and water	[g]
m_{total}	Total mass of the solids and water combined	[g]
n	Porosity	[-]
N	Normal force	[N]
Re_p	Reynolds number	[-]
V	Volume	[cm ³]
V_s	Volume of the particular solids	[m ³]
v_{th}	Hindered terminal settling velocity	[m/s]
V_{total}	Total volume of the solids and water combined	[m ³]
v_{ts}	Terminal settling velocity	[m/s]
v_t	settling velocity	[m/s]
w	Water content	[-]
W	Weight of sliding mass	[N]
w_n	Natural water content	[-]

x	Hindered settling exponent	$[-]$
p	Pore pressure	$[\text{Pa}]$

List of Figures

1.1	Manganese nodules on the seabed off the southeastern U.S., 2019 (NOAA). .	2
1.2	Polymetallic nodule provided by IHC.	2
1.3	Sub-sea mineral deposits with emphasis on the Clarion-Clipperton Zone[1] . .	3
1.4	The MV Black Rose capsized as a result of cargo liquefaction[2]	4
2.1	Schematic overview of a mining operation.	7
2.2	schematic picture of the process flow. Solid lines represent the main flow (Nodules) and dashed lines represent secondary flow (SWOE). Blue arrows show the general direction of the flow [3].	8
2.3	The flowchart shows the three different transport systems. The colour represents the current TRL of the system. With mechanical, there is an option to have batch production and semi-continuous production [4].	11
2.4	The change of particle size in the vertical fluidization experiment of de Hoog et al.[5].	12
2.5	Overview topside treatment of nodules.	13
2.6	The left photo shows ship to ship transport via a conveyor system, the right picture shows a hydraulic transport.	13
2.7	Flowchart interface between mining support vessel and transport vessel. . . .	14
2.8	Schematic representation of a spiral classifier.	16
2.9	Hydrocyclone: (a)Principle flows. (b)Forces acting on an orbiting particle (JKMRC, The University of Queensland).	17
2.10	Diagram of filtration: oversize particles in the feed cannot pass through the lattice structure of the filter, while fluid and small particles pass through, becoming filtrate.	18
2.11	Example of a vibrating dewatering screen[6].	19
2.12	Example full scale filter press, the pressing takes place in the vertical white plates. (Dutch filtration).	20
2.13	Schematic view of filter press (Judd Water & Wastewater Consultants). . . .	20
2.14	Detailed flowchart of the possible dewatering process. The pink colour represents the hardware where the separation takes place. The yellow colour represents states the location of the product.	22
2.15	(a) Shows the proposed dewatering setup of Blue nodules[7] and (b) Shows the proposed dewatering setup of Chatham Rock Phosphate Limited[8].	23
2.16	The Location of B2 InterOceanmetal Joint Organization (IOM) area and H22 and H11 exploration blocks against the background of Clarion–Clipperton Zone Exploration Areas for Polymetallic Nodules[9].	27
2.17	Schematic overview of the three regimes which the nodules will encounter during the journey from the riser system to the ship storage.	27
2.18	Definition of particle aspect ratio AR. For Spherical particles, the Aspect ratio is 1[10].	31
2.19	Particle degradation mechanisms [11].	32
2.20	Susceptibility to liquefaction is related to the relative density of a material: Loosely packed granular materials tend to contract when loaded. Untrained conditions lead to an increase in pore pressure.	33
2.21	Schematic depiction of the steps for dynamic separation.[12]	34

3.1	Before and after sieving.	39
3.2	Schematic overview of volume and mass measurement of a batch of nodules. .	40
3.3	Moisture dissipation during the time in the oven.	42
3.4	Density measurements from the literature.	42
4.1	The left image shows the setup, and the right image shows the scanning process.	46
4.2	Qlone digital scan.	47
4.3	Comparison Qlone 3D printed scan and nodules with dimensions.	47
5.1	Schematic overview of angle of repose. α represents the angle of repose. . . .	49
5.2	Two views of the angle of repose setup.	50
5.3	Gopro camera distortions [13].	51
5.4	Results of 18 angle of repose test with dry nodules and 18 tests of saturated nodules.	51
6.1	Forces acting on a body on an inclined plane.	54
6.2	Static friction and dynamic friction[14].	54
6.3	Inclined surface tester in operation.	55
6.4	Inclined surface tester for a saturated test.	56
6.5	Overview of the inclined surface tester experiments. The surfaces which were used for the tests were steel and rubber. Furthermore, the tests were conducted with dry, saturated and CCZ clay-rolled nodules	57
6.6	Single nodule test setting, left side shows the 50 - 70 mm class, the right side shows the 16-25 mm class.	57
6.7	Bulk-free example, left shows the E (16-25 mm) batch and the right side shows the B(50-70 mm) class.	58
6.8	The batches of nodules used in the bulk-free tests are shown here. Top left shows the F(10-16 mm)batch, E(16-25 mm) batch on the bottom left side. B(50-70 mm) batch on the top right and the C(30-50 mm) batch on the bottom left. Particle sizes had a dry and a saturated batch.	58
6.9	Bulk confined example.	59
6.10	Added mass test schematic.	59
6.11	3D printed sled for the added weight test and the gips/glued blocks of nodules.	60
6.12	Single nodule box and whisker plot: Rubber on the left side and steel on the right side.	61
6.13	Surface roughness of 3 different surface roughness values and the corresponding friction angle: steel smooth ($0.46 \mu m$), steel rough($1.16 \mu m$) and rubber($1.35 \mu m$).	62
6.14	Box plot of free bulk tests, all test were repeated 8 times.	63
6.15	Confined bulk box and whisker plot.	64
6.16	Friction angle vs particle size.	65
6.17	Added mass box and whisker plot, for rolling and sliding test together.	66
6.18	Histogram added mass, rolling and sliding.	66
6.19	Interaction between a hard solid surface and rubber [15].	67
6.20	Abrasion marks on steel plate and on the plaster mold.	68
6.21	The histogram of all the tests conducted on rubber and steel.	69

6.22	Box and whisker plot of all inclined surface tester with rubber as surface. Input values and count can be found in table 6.5.	71
6.23	Box and whisker plot of all inclined surface tester with steel as surface.	72
7.1	Example of a bucket wheel self offload system on a trailing hopper dredge to offload material in a dry state (Reimerswaal dredging).	73
A.1	Dewatering setup Chatham Rock Phosphate Limited[8].	78
B.1	Particle size distribution and a histogram.	80
B.2	Settings of the oven: Temperature is set at 105°C, ventilation at 20%, timer at 24 hours and ventilation flap was set to 100% to remove moisture from the oven.	80
B.3	Shows a saturated angle of repose test with the angle measurement tool in matlab.	81
B.4	Angle of repose histogram and test results.	83
B.5	CCZ sediment used to simulate sediment effects on nodules.	84
B.6	Single nodules histogram.	85
B.7	Bulk free data plotted.	86
B.8	Confined bulk histogram.	87
B.9	The left graph shows a example of cross section of a surface. The right figure shows the measuring device.	88
B.10	Surface roughness results.	89
B.11	3D model of sledge for added weight testing.	91
B.12	Histogram of all the tests combined.	92
B.13	Table with friction factor instead of angle.	93

List of Tables

1.1	Chemical composition of GSR samples, valuable metals in mass percentages.[3]	3
2.1	Estimated nodule, sediment and water flow on the seabed to collector stage [3].	9
2.2	Estimated flow inside riser system [3].	11
2.3	Settling times of nodules according to Sanjay et al [16].	16
2.4	Differences between centrifugal and gravitational classifiers[17].	18
2.5	Nodule properties of 205 Nodules samples taken from the Clarion Clipperton region, location H22 [18].	26
2.6	Bulk properties retrieved from four dredged samples of an expedition in 2014 with 2309 kg of nodules being retrieved[18] using mainly intact nodules. The values can have a significant relevance as comparison material for bulk properties taken from degraded nodules.	30
3.1	Classification nodules.	38
3.2	Measurements for density.	41
3.3	Particle properties.	41
4.1	Validation Qclone.	47
6.1	Single nodule test.	61
6.2	Bulk angle of bulk-free test.	63
6.3	Confined bulk table.	64
6.4	The statistics and histogram of all the tests. All values have angle[°] as unit. The corresponding coefficient of friction can be found in appendix B.13. . . .	69
6.5	Summary of of inclined surface tester results.	72
B.1	PSD input values.	79
B.2	Input data for figure 6.13.	90

1 - Introduction

The chapter begins with basic information about deep sea mining and polymetallic nodules in section 1.1, giving some history and information about the main reason for this topic. The problem description is defined in section 1.2. The objective, primary and secondary research questions are given in section 1.3. The chapter ends with 1.4, where the outline of this master thesis is provided.

1.1 Deep sea mining in general

The rapid economic development of this world causes an increased demand for raw materials, especially the materials needed for renewable energy and storage. This is further complicated by the dominance of one single player supplying the raw materials. China controls the battery chemical industry, with the biggest market share for all of the five main battery materials: lithium, nickel, manganese, cobalt and graphite. Diversifying the global supply chain would require significant investment from regions such as Europe and North America, according to the latest Battery Metals Outlook from research company BloombergNEF[19]. In addition, land-based mines all over the world struggle to cope with demand, decreasing ore grades and unstable governments in the mining areas[20].

Deep sea mining can potentially alleviate these struggles by providing an additional stream of locally mined ores from potentially independent areas.

History

Even though the ocean covers 70% of the earth, it remains a relatively unexplored frontier. Exploration of the possibilities of exploitation of the seabed started in the fifties[21]. There was a particular interest in metal-bearing nodules, which are potato sized rock concretions covering large parts of the ocean. The most common name for these nodules is manganese nodules or polymetallic nodules. An interesting feature of the nodule mineral deposits is that they are two-dimensional, and can therefore be collected from the seabed surface. Figure 1.1 shows the abundance of nodules at the seafloor, typically ranging between 3000 and 5000 meters in depth.

After the fifties, interest in nodule collection ebbed away, when metal prices decreased and the technical challenge of nodule collection seemed too high. Only in recent years, high demand for rare metals, and technology advancements, have changed the tide, that now nodule collection is economically viable.[22]

Nodule composition

Polymetallic nodules contain manganese, nickel, cobalt, copper, and rare earth elements[23]. According to the International Seabed Authority¹ description [24], “polymetallic nodules are rock concretions formed of concentric layers of iron and manganese hydroxides around a core. The core may be microscopically small and is sometimes completely transformed into manganese minerals by crystallization. When visible to the naked eye, it can be a small shell of microfossil (radiolarian or foraminifer), a phosphatized tooth of a shark, basalt debris or

¹Made up of 167 Member States, and the European Union, the International Seabed Authority is mandated under the UN Convention on the Law of the Sea to organize, regulate and control all mineral-related activities in the international seabed area for the benefit of mankind as a whole.

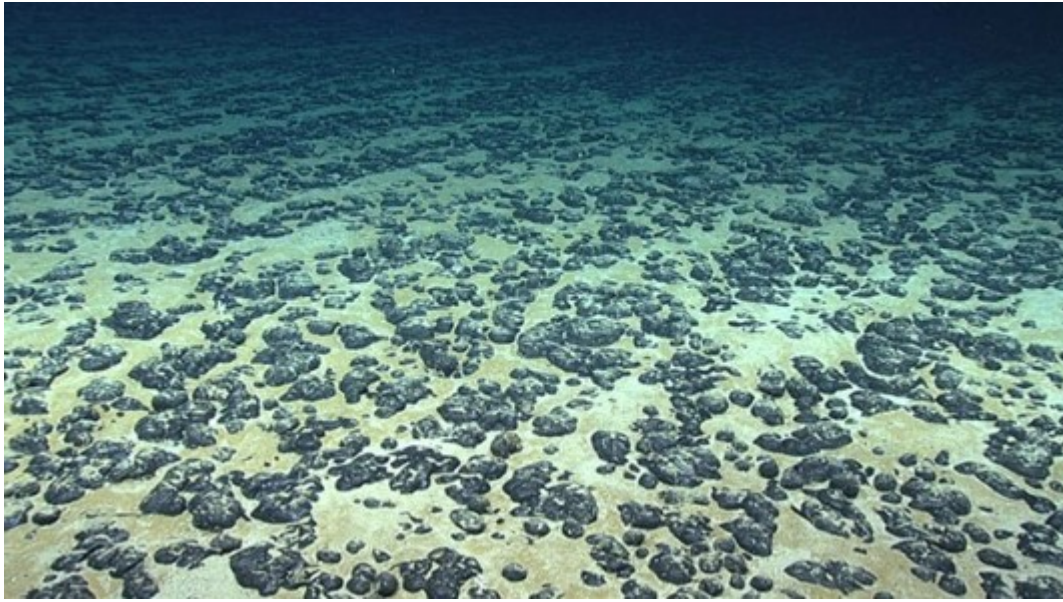


Figure 1.1: Manganese nodules on the seabed off the southeastern U.S., 2019 (NOAA).

even fragments of earlier nodules. The thickness and regularity of the concentric layers are determined by the successive stages of growth. On some nodules they are discontinuous, with noticeable differences between the two sides. Nodules vary in size from tiny particles visible only under a microscope to large pellets more than 20 centimetres across. However, most nodules are between 5 and 10 cm in diameter, about the size of potatoes. Their surface is generally smooth, sometimes rough, mammilated(knobby) or otherwise irregular. The bottom, buried in sediment, is generally rougher than the top”.



Figure 1.2: Polymetallic nodule provided by IHC.

To give an overview of the chemical composition of manganese nodules, data provided by the GSR(Global Sea mineral Resources) is used. This data was gathered from 25 box-cores during two sampling campaigns to the CCZ license area in 2017[3]. Table 1.1 shows the result of gathered data.

From this table, the materials necessary for batteries: cobalt (Co) and nickel (Ni), are the most critical raw materials. Per nodule, the percentage present of this substance is not that high. However, when looking at the abundance of nodules on the seabed, it turns out that these are vast amounts of material. The following section expands on this.

Table 1.1: Chemical composition of GSR samples, valuable metals in mass percentages.[3]

Element	Quantity	Unit	Element	Quantity	Unit	Element	Quantity	Unit
Mn	27.09	%	La	100.8	ppm	Tb	4.7	ppm
Ni	1.308	%	Ce	294	ppm	Dy	25.2	ppm
Cu	1.127	%	Pr	30.7	ppm	Ho	4.7	ppm
Co	0.213	%	Nd	129.1	ppm	Er	12.7	ppm
Mo	0.058	%	Sm	31.8	ppm	Tm	1.9	ppm
Pt	0.083	g/t	Eu	7.7	ppm	Yb	12.1	ppm
Pd	6	ppb	Gd	29.8	ppm	Lu	1.8	ppm
Y	80.1	ppm						

Location

Nodule fields are found in the oceans all over the world to a greater or lesser extent. The area where the nodule fields are most abundant is the Clarion-Clipperton Zone (CCZ) in the Pacific Ocean, where nodules occur at water depths of 3700-5500 meters[18]. The average abundance in this zone is 10 kg/m^2 with abundance peaks of 38 kg/m^2 [25]. In an area of 4.5 million square kilometres, reserves of polymetallic nodules are estimated at 274 Mt for nickel and 44 Mt for cobalt, multiple times the global terrestrial reserves [1].

The environmental conditions consist of a saltwater environment in the deep sea, with pressures of ca. 500 bar and temperatures of ca. 2°C . These conditions necessitate the development of a highly robust technology for the future mining of polymetallic nodules[26]. Figure 1.3 shows the location of the nodule deposits around the world with emphasis on the Clarion-Clipperton Zone (CCZ).

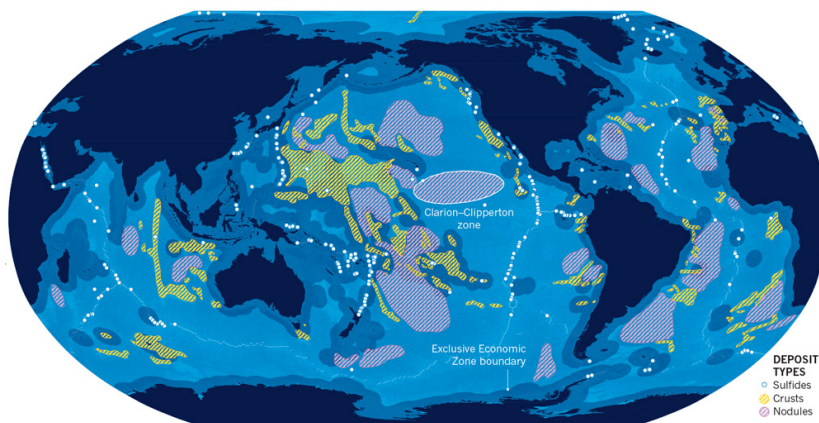


Figure 1.3: Sub-sea mineral deposits with emphasis on the Clarion-Clipperton Zone[1]

1.2 Problem definition

In recent decades, a significant amount of the research into deep sea polymetallic nodule mining has been conducted on the collecting vehicle and the riser system accommodating transport from the seabed to the mining support vessel. More recently, the focus of the research has shifted more towards the environmental impact and the scale-up of the operation. These are arguably essential parts of the deep sea mining operation. If transport proves to be technically impossible or the environmental impact is too high, the project would have no chance of success. The topside operation, however, is less commonly described in the literature. This part of the operation deserves attention because it can still significantly reduce project risks. An overview of the harvesting setup will be given in chapter 2.1.

Topside operation

The topside operation mainly consists of dewatering, storage and transport of the nodules.

- Dewatering is challenging in a confined and moving environment at sea. While dewatering is a common practice in the land-based mining industry, and wastewater and sludge treatment industry.
- The storage of the polymetallic nodules after the dewatering stage is another interesting topic. Little research has been conducted on how the nodules behave when stored into a storage hold; phenomena like liquefaction or dynamic separation could happen when the nodules are handled carelessly. These phenomena have caused many fatalities over the years on other bulk cargo types. Figure 1.4 shows the capsized MV Black Rose as a result of cargo liquefaction.
- The transport within the mining support vessel and between ships is the third topic of the topside operation. The behaviour of polymetallic nodules has not yet been mapped. This makes it challenging to create transport systems, i.e. transport belts and material chutes, suitable for moving this kind of bulk material.



Figure 1.4: The MV Black Rose capsized as a result of cargo liquefaction[2]

1.3 Research questions

This master thesis aims to provide an insight into the topside processes of a deep-sea polymetallic nodule mining operation. Therefore, the main research question is defined as follows:

What is the effect of moisture on the granular characteristics of polymetallic nodules in the context of bulk handling?

The secondary research questions, which are sorted per chapter, are formed as follows:

Theory

- What are effective strategies to dewater polymetallic nodules in a confined space on a mining support vessel.
- How do the dewatering strategies at sea compare to land based dewatering installations?
- What are the physical states and their corresponding aspects to consider when handling polymetallic nodules?

Experimental

- How do the **densities** of the IHC nodules compare to the nodules from other sites of which experiments are published in available literature?
- Is **photogrammetry** with Qlone an effective method for scanning polymetallic nodules?

Lab tests were used to clarify the behaviour of degraded polymetallic nodules in a dry and fully saturated condition.

- What is the **angle of repose** of degraded polymetallic nodules and how is it influenced by moisture content?
- What is the **sliding/rolling friction angle** of nodules placed on a steel slide and on a rubber conveyor system when taking into account different compaction states?
 - How does the particle size affect the friction angle?
 - What is the effect of moisture content on rolling/sliding friction angles?
 - What is the effect of adhesion forces of clay on and rolling/sliding friction angles?
- How does the normal force influence the rolling/sliding friction angle?
- What effect do the sliding nodules have on the sliding surface roughness?

1.4 Outline of this thesis

The thesis is divided into a theoretical part, an experiment-oriented part followed by an all-embracing conclusion.

The theoretical chapter consists of three sections: The first section gives an overview of the nodule mining operation. It starts from the collector vehicle at the seafloor, followed by the vertical transport system, the topside operations and the handling of sediments, waste and other effluents that will be returned deep sea.

The second section regards the dewatering operation. First, the three modes of dewatering, i.e. sedimentation, filtration and thermal drying, are discussed. After this section, an overview of the dewatering options for an effective dewatering strategy is provided. At the end of the chapter, the main differences between on-land dewatering and offshore dewatering are discussed.

The third section discusses the effects of water on material and properties of the nodules. This chapter is divided into three sub-sections: Solids in slurry, granular behaviour and moisture in large granular material.

The experiments-oriented chapters consist of four chapters in which four experimental setups were used to understand the granular characteristics of degraded polymetallic nodules in a non-destructive manner. The parameters that are obtained from these experiments are useful in the design of bulk handling equipment such as conveyors and chutes. This prevents overdesign or underdesign of the deep sea mining operation, which could lead to leading to higher costs or unsafe situations.

In the first setup, particle properties such as density, porosity, and water content have been measured. The second setup identifies the shape of degraded nodules. The third setup measures the angle of repose for different nodule sizes and water content. The last setup measures the friction angle for different nodule sizes and water content, while changing the sliding surface between steel or rubber. Lastly, clay has been added to the sliding surface experiment. The chapters elaborate on these different setups and their goals for which IHC provided 50 kg of polymetallic nodules used in the research of de Hoog and van Wijk [5, 27].

2 - Theory

This chapter consists of three sections: The first section gives an overview of the nodule mining operation. The second section regards the dewatering operation. The third section discusses the effects of water on material and properties of the nodules.

Secondary research questions of this chapter:

- What are effective strategies to dewater polymetallic nodules in a confined space on a mining support vessel.
- How do the dewatering strategies at sea compare to land based dewatering installations?
- What are the physical aspects to consider when handling polymetallic nodules?

2.1 Overview of the mining setup

The mining operation of polymetallic nodules from the seafloor comprises excavation, a vertical transport system from the seafloor to the sea surface, called a riser and the processing and shipping of the material afterwards. The mining system will be producing a mixture of seawater, fine seabed sediments and polymetallic nodules[5]. Figure 2.1 shows a schematic overview of the operation. It consists of a mining vehicle on the seabed, riser system, mining support vessel and a bulk carrier. The mining vehicle grabs the nodules from the bottom and sends them to the mining support vessel using a riser system, also called a VTS (Vertical Transport System). Subsequently, the nodules are separated from the water-sediment mixture, and then transported to the bulk carrier. Finally, sediment, water, waste and other effluents (SWOE) are discharged through a discharge pipeline.

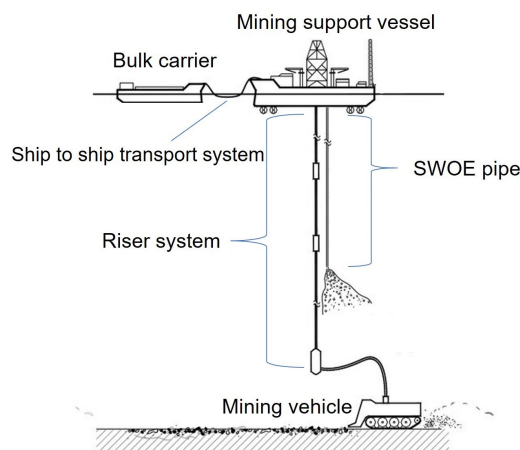


Figure 2.1: Schematic overview of a mining operation.

Process flow overview

Figure 2.2 shows a proposed process flow for nodule handling from seafloor to shore [3].

The nodules lie either on top or just below the sediment surface. Therefore, unwanted sediment and an excess of water will inevitably be entrained with the nodules while collecting. A system is developed which separates most of these unwanted substances directly at the seafloor. This sediment flow is represented by Stage 2 in figure 2.2. After the first separation, the mixture of nodules, water and a small amount of sediment will be pumped to the mining vessel through a riser system. Then, the mixture has to be dewatered for storage and shipment. This operation will also result in a waste stream which will be guided by a fallpipe to be discharged at considerable depth, to reduce environmental impact [28].

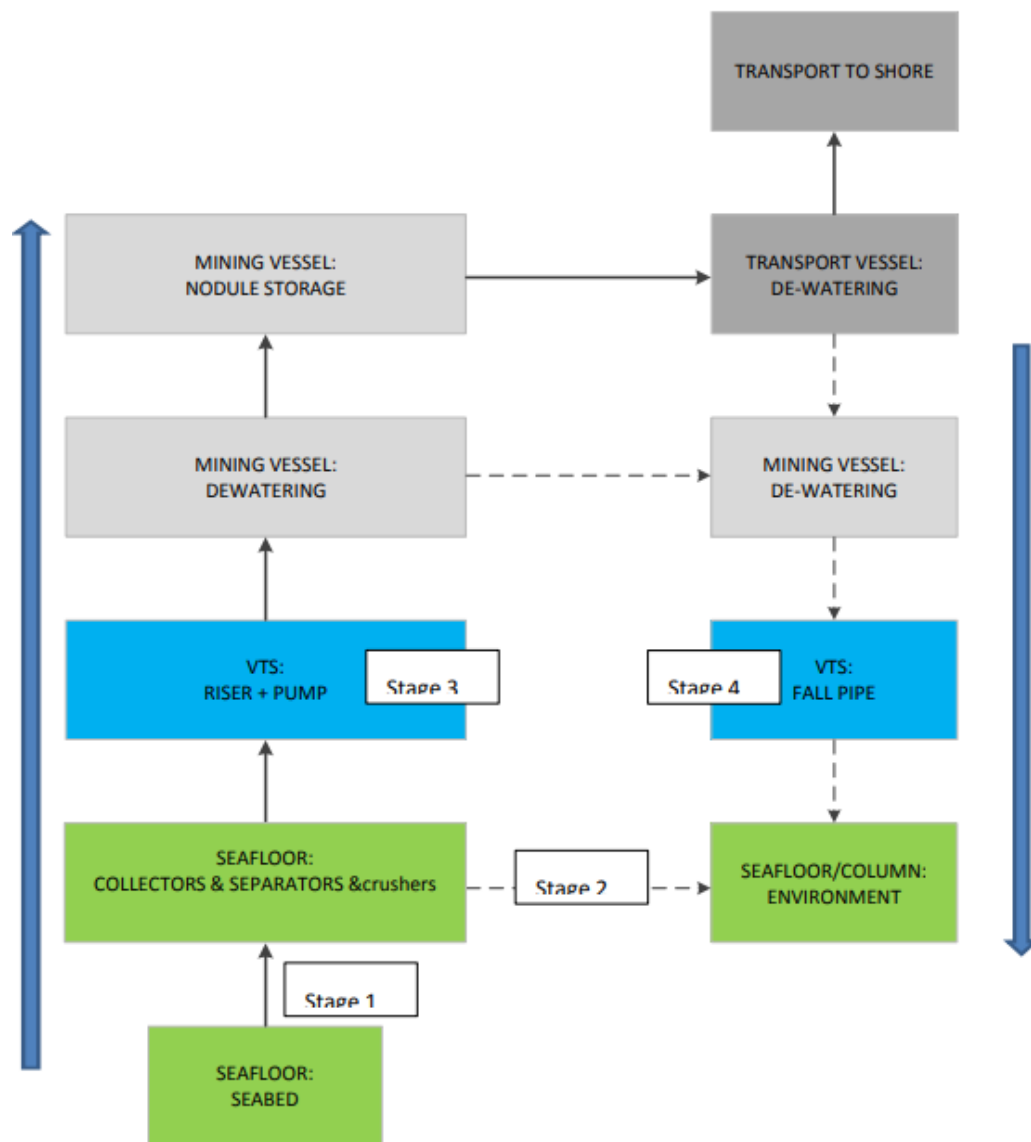


Figure 2.2: schematic picture of the process flow. Solid lines represent the main flow (Nodules) and dashed lines represent secondary flow (SWOE). Blue arrows show the general direction of the flow [3].

2.1.1 Seafloor mining tool

The polymetallic nodules lie on or just below the sediment surface; they can be harvested similar to a potato field. An uptake mechanism is used to collect the nodules[29]. According to literature, collection is currently done in three ways: Mechanical collection, hydraulic collection or a hybrid version. In mechanical collection, rake-like tools on drums guide the nodules toward the collector. In hydraulic collection, water jets are used to lift the nodules together with ambient sediments, which are subsequently sucked into the nodule collector [29, 30]. From the collector, a mixture of nodules, sediment and water is pumped toward the riser system. For both collection methods, before entering the riser, 90% of the sediment and excess of water will be separated immediately in the seafloor mining tool. This flow will be discharged behind the vehicle [3].

Table 2.1 indicates a prediction, provided by IHC and DEME-GSR, of mass and volume collection of sediment, nodules and ambient water during hydraulic and mechanical collection process [3, 29].

Table 2.1: Estimated nodule, sediment and water flow on the seabed to collector stage [3].

Collector type	Parameter	Nodule (wet)	Sediment (dry)	Water	Total
Mechanical	Mass [t/h]	467	805	2977	4249
	Volume [m^3/h]	230	322	2904	3456
Hydraulic	Mass [t/h]	492	805	23037	24335
	Volume [m^3/h]	243	322	22475	23040

2.1.2 Vertical transport system

The next step in the chain is the vertical transport system(VTS), also called riser system. The minerals need to be lifted from the sea bottom to the surface. The vertical distance travelled will be around 3000 to 5000 meters. There are a couple of different ways to achieve transport over this distance. This section will explain the three main modes of transportation to the surface: Mechanical, Air lift and Hydraulic transport. Unfortunately, up to now, no full scale deep-sea mining operation exists [31], so there is no practical comparison available.

Mechanical lifts

A mechanical lift is highly suitable to vertically move raw materials, such as a standard lift or bucket lift. These techniques have been used for centuries and have proven their reliability. Unfortunately, this technique also has a significant limitation. Lifting cables have a weight limit per length. For a short distance, these cables can lift high weights, and it is efficient, but when considering the deep sea mining distances, 3000 m to 5000 m, the weight of the cable system the starts to play a significant role. The lifting cable therefore creates problems for the production target and transport velocity [32].

A comparison between the different kinds of vertical transport shows that vertical transport by mechanical bucket lifting is the most energy efficient transport system of the

compared systems. A disadvantage of mechanical lift is that currently no winch exists which could meet the production targets.[4]

Air lift

Air lift transport is an effective and robust way of transporting goods over a vertical distance. The airlift system utilises a process of injecting air into the collection line and creating a three-phase mixture. Air reduces the density of the slurry and induces a flow driven by the pressure difference between the nodule feed point and the end of the VTS[33, 34]. A significant advantage of the air lift system is that there are no moving parts along the length of the riser, only air injections. The biggest disadvantages are that it is expensive to operate[30] and hard to control the air fraction, especially at the riser top; expanded gas needs to leave the system, which causes problems [4, 32],

Hydraulic transport

Hydraulic transport is the working horse for the dredging industry. It is a robust way of transporting large amounts of solids over large distances in a marine environment, by using centrifugal or positive-displacement pumps. The system is scalable with high production targets and has the highest technology readiness level. It comprises of hydraulic pumps located along a pipeline. The complexity however, comes with the moving parts inside the pumps. A high level of redundancy needs to be built-in to assure stable and reliable production [3, 27].

The two pump systems, centrifugal and positive-displacement, have slightly lower efficiencies than mechanical lifting and have some disadvantages when used in deep water, in case of centrifugal pumps, multiple pumps would be needed, whereas in case of positive displacement pumps, high pressures would be needed. Another disadvantage is the amount of water which has to be pumped to the surface in order to prevent clogging[27]. At the topside of the operation, this water has to be removed.

VTS design choice and implications

Looking at available literature in the riser development[4, 7, 27, 29], It can be concluded that hydraulic transport has the highest chance of reaching the level of full-scale operation first. This hydraulic method is also preferred by IOM (The Interoceanmetal Joint Organization), an intergovernmental consortium established to conduct exploration, evaluation and exploitation of polymetallic nodules in the Clarion-Clipperton Zone (CCZ) in the north-east Pacific[18]. Figure 2.3 gives an overview of the three different systems. The important differences between the air lift and the hydraulic lift are the amount of water that needs to be removed at the topside and potentially how much damage the nodules have incurred during transport.

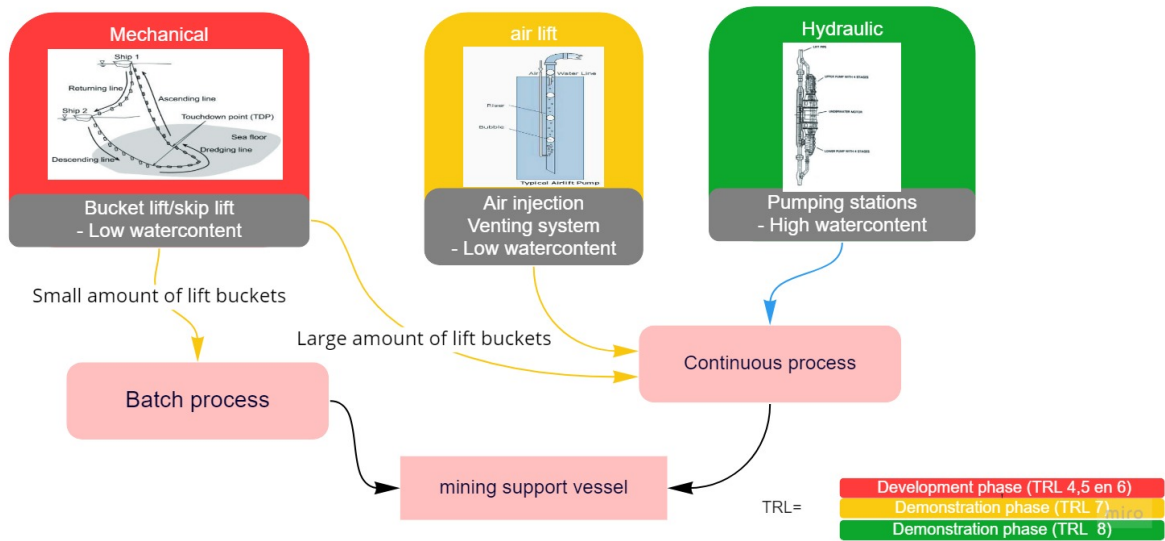


Figure 2.3: The flowchart shows the three different transport systems. The colour represents the current TRL of the system. With mechanical, there is an option to have batch production and semi-continuous production [4].

VTs production figures

Within the Blue nodules project[3], research was conducted on the hydraulic riser production estimates. Table 2.2 shows the result of that research. These numbers are important for further processes on the mining support vessel. During the transportation, due to the abrasive action and riser pumps action a fraction of the nodules experience abrasive, crushing and impacting forces. Hence, the particle size distribution of the transported nodules in the riser system will change to a more fine grained distribution at delivery on sea surface.[5, 35]

Table 2.2: Estimated flow inside riser system [3].

Collector type	Parameter	Nodule (wet)	Generated fines $<63 \mu m$	Sediment (dry)	Water	Total
Hydraulic	Mass [t/h]	491	2	81	1187	1761
	Volume [m^3/h]	242	1	32.2	1159	1433

2.1.3 Cleaning process and storage

The vertical transport system ensures that the nodules rise to the mining support vessel where the nodules will be temporary stored. However, as discussed in the previous section, the riser system brings along two challenges. The first one is water ($1159 m^3/h$) and sediment ($32 m^3/h$) accompanying the nodules. The mixture needs to be separated to ensure that the nodules are stored efficiently.

The second challenge is the impact of the riser system on the nodules. The nodules will have to endure multiple impacts with the pipeline and the pumps on the way to the surface.

Van Wijk and De Hoog have produced several papers in which they have investigated and analyzed the impact effects of the pumps and the pipeline on the nodules[5, 35, 36]. Figure 2.4 shows what happens when you move a load of nodules over different lengths of pipe. The large nodules will break and a fraction with small nodules, also called fines, is created. The experiments started with nodules of the 45–31.5 mm class and three consecutive experiments. At the end of the experiment, the nodules reduced in size and 10 % of the mass of the nodules reduced to fines.

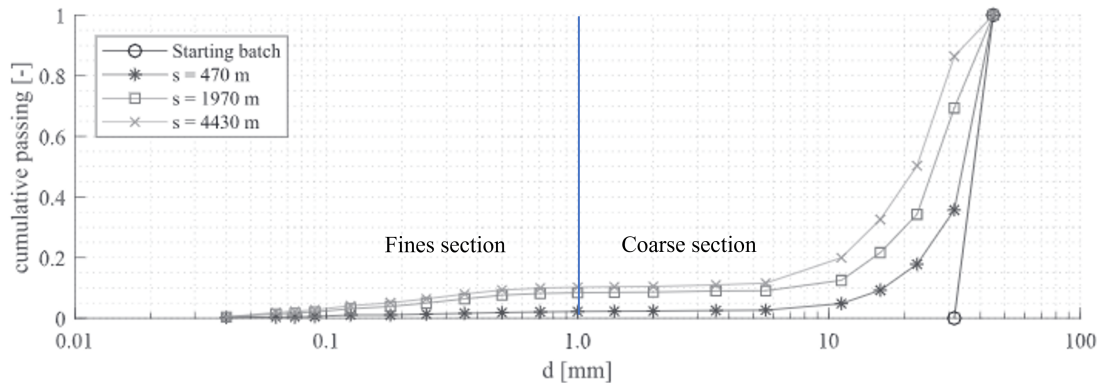


Figure 2.4: The change of particle size in the vertical fluidization experiment of de Hoog et al.[5].

Dewatering stages

Dewatering is necessary for efficient storage, the weight of the excess of water would decrease the loading capacity of the vessel and a high moisture level load behaves differently than dry bulk. Figure 2.5 shows an overview of the steps necessary to have efficient storage. On the left, the figure shows the incoming untreated product. The first step is to separate nodules larger than 1 mm from the free water. This results in a solids part and a slurry stream. The slurry stream consists of particles smaller than 1 mm, which are micronodules and sediment. According the papers from de Hoog en van Wijk [5, 27, 35], The micronodules are of slightly larger particle size ($< 1 \text{ mm}$) than the sediment ($< 0.1 \text{ mm}$). Since a separation step is required, a hydro cyclone could be an effective way to separate, creating a slurry with micronodules and a slurry with sediment. The sediment slurry leaves through the discharge system, and the micro nodule slurry is further processed in a final step. In the end, there will be a coarse nodules section without free water, a compacted fines section without free water, and a waste stream with the sediment. In section 2.3, the separation process is further explained.

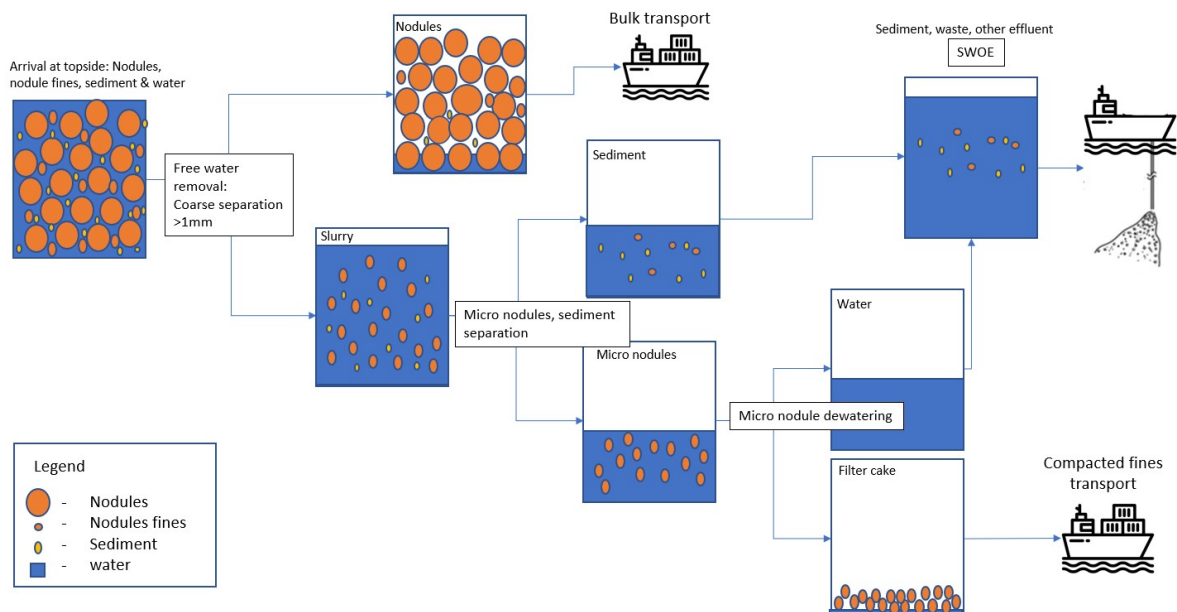


Figure 2.5: Overview topside treatment of nodules.

2.1.4 Ship to ship transport

The nodules on the mining support vessel have to be moved to the coast in order to process the raw materials. Since it concerns bulk material, it will be transported by bulk carriers.[7, 30] However, it is not yet entirely clear how the nodules arrive on the ship. There are two suggestions: Drained or hydraulic transport.

- **Drained transport:** The nodules in the storage hold of the mining support vessel are placed on a transport belt connected to the bulk carrier, as shown in figure 2.6 on the left.
- **Hydraulic transport:** The nodules out of the storage hold of the mining support vessel are re-watered and transported through a pipeline connected to the bulk carrier, as shown in figure 2.6 on the right hand side.



Figure 2.6: The left photo shows ship to ship transport via a conveyor system, the right picture shows a hydraulic transport.

Both systems have their advantages and disadvantages. The main advantage of hydraulic transport is that the ships remain at a distance from each other, because a pipeline can stretch

over a longer distance. This reduces the risk of ships colliding. The main disadvantage of the hydraulic transport is the requirement of an additional dewatering station on every bulk carrier that is to be used. When there is too much moisture in cargo, there is a possible danger for the stability of the cargo and, therefore, also the stability of a ship. Chapter 2.3 will further explain this limit. [7]

For the drained transport, the main advantage is the absence of needing additional dewatering stages at the bulk carrier. This also results in lower water content at the bulk carrier. The disadvantage of drained transport is that the ships have to be in close proximity to each other, which is a high risk operation considering the wave and weather conditions in the areas of interest. Figure 2.7 shows the possible steps of the ship to ship transport operation.

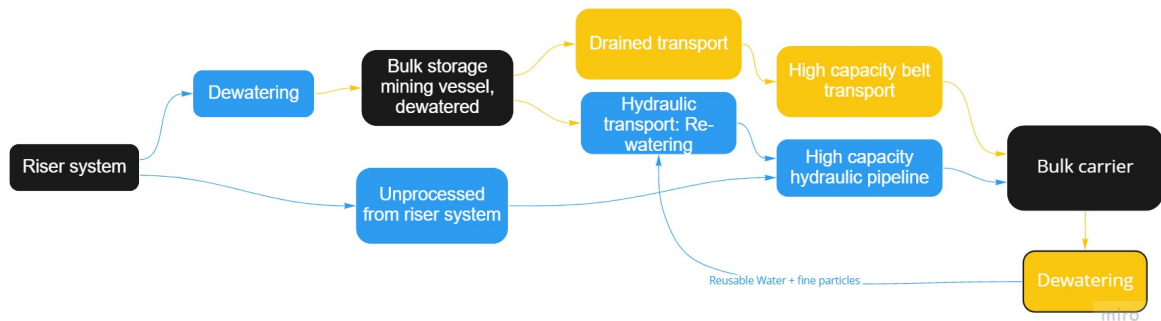


Figure 2.7: Flowchart interface between mining support vessel and transport vessel.

2.1.5 SWOE

Slurry containing nodules, sediment and water is pumped up the riser where the nodules are removed, and remaining material is pumped back to the seafloor. The latter is called SWOE: sediment, waste, other effluent. When there is a perfect separation at the mining vehicle there will be no sediment present in the SWOE. In practice, as stated in section 2.1.1 it can be expected that 10% of the sediment will reach the mining support vessel. When released in the ocean, the sediment will cause a plume which could harm the environment[1]. Because of the potential environmental damages in the depth zone from the surface to 1000 m, it is strongly recommended that discharges be released below the depth of the oxygen-minimum layer.[26, 37]

2.2 Comparison of dewatering strategies

As presented in chapter 2.1, it is not feasible to bring only the nodules to the surface. Any vertical transport system will deliver a mixture of nodules and water. Furthermore, subsea soil particles will probably be pumped into the vertical transport system[4]. A dewatering and classifying system needs to be built for two reasons:

- To remove the water and soil from the slurry so the nodules can be stored efficiently.
- To reduce the amount of fines in the SWOE, which results in less plume formation and therefore minimising environmental impact.

Dewatering methods can be broadly classified into three groups: sedimentation (gravity and centrifugal), filtration, and thermal drying [17]. Dewatering in mineral processing is usually a combination of these methods. The methods will be further explained in the first three sections in this chapter. The fourth section will combine the knowledge of the dewatering techniques, and a flowchart is given with a dewatering strategy for manganese nodules at sea. The last section will look at the differences between land based and offshore dewatering installations.

2.2.1 Sedimentation

The first separation process that will be discussed is the process which uses sedimentation. Sedimentation processes can be subdivided into two groups: gravity based and centrifugal.

Gravity sedimentation

Gravity sedimentation is the separation of minerals based upon the difference in density. A slurry has to be pumped into a reservoir and gravity will separate the solids from the liquid [16]. Using a sedimentation tank, the nodules can be separated from the water and sediment. The settling equation, which is shown in chapter 2.3.1, can determine how much time the slurry has to spend in the tank before the nodules have settled. Table 2.3, taken from Sanjay et al[16], shows an indication of the settling times for the nodules if they are larger than 1 mm and the fines smaller than 1 mm. This settlement is done in a batch process. First, a tank is filled with slurry, and after a certain time, the particles are settled, and the water can be pumped out, leaving the nodules. After this step, the nodules can be transported to the storage. Because of the continuous inflow of material to the mining vessel, it is necessary to have several settling tanks parallel so that the slurry stream can be diverted when one tank is full. This setup takes up large amounts of space and is therefore not preferred on a vessel[7, 16]. A rough estimate of the required ship volume or deck space illustrates the required space: First, the inflow rate of the slurry from the VTS is used, which is based on the production numbers of blue nodules[38]: An input of 100 kg/s dry bulk with a density ρ of 2000 kg/m³ and a volumetric concentration c_v of 0.20 results in a volume flow of 0.3 m³/s. Every hour, this would mean that 1080 m³/hour needs to be stored on the vessel. This would be a solution for the coarse material, since the settling time is only a couple of seconds, but the fines have long settling times. This would mean that a tank needs to be filled and then wait for 16 hours. So in this time, The riser system would have provided approximately 16.000 m³ of slurry. When considering that the vessel is a mining support vessel, this would seriously compromise the storage capacity of the vessel.

The fines sedimentation on a vessel has another setback: the ship moves due to the wind and waves; this creates water motion in the vessel and increases the settling time of small particles. The most significant advantage of gravity sedimentation is the low power usage: no additional pumps are required for the sedimentation[17].

Table 2.3: Settling times of nodules according to Sanjay et al [16].

Pulp density	Size fraction	Settling time(t_{avg})
10%	<1mm	16.5 h
	1-30mm	6.082s

Spiral Classifier

A technique to convert a batch sedimentation tank into a continuous system exists. A spiral or screw classifier can achieve this. Figure 2.8 shows a schematic representation of such a device: The slurry flows into the settling pond, from where a spiral pushes it above the waterline, which separates the nodules from the slurry. This method has some benefits and drawbacks in comparison to a regular settling tank. A significant advantage is that the technique works continuously; the inflow and discharge are continuous. A disadvantage is that it is impossible to separate the fines; there will be too much turbulence for the fines to sink to the bottom. Another type of separation method will be needed to separate the fines.

Chatham Rock Phosphate Limited (CRP) has proposed to mine phosphorite from the crest of the Chatham Rise (New Zealand), which would require a similar dewatering installation as a nodule mine operation for phosphate nodules. In the design phase of CRP operation, it was found that spiral classifiers are predicted to significantly improve the performance of the separation system.[8]

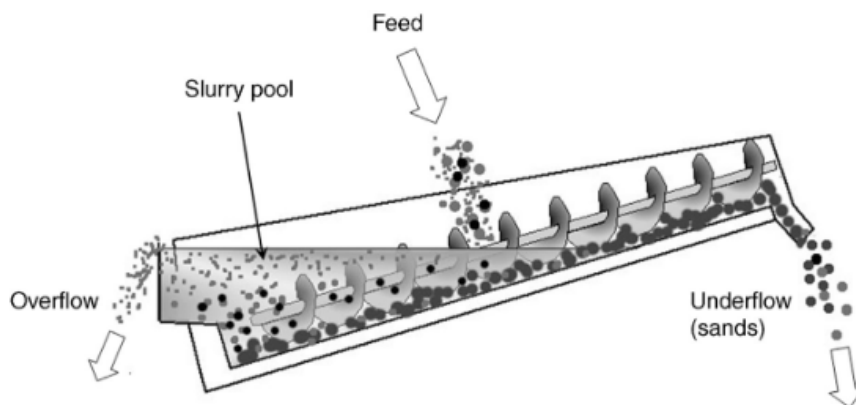


Figure 2.8: Schematic representation of a spiral classifier.

Centrifugal separation

Centrifugal separation can be regarded as an extension of gravity separation, as the settling rates of particles are increased under the influence of centrifugal force. Centrifugal separation

can be performed by hydrocyclones[17]. A cyclone is a device that separates particles by creating centrifugal forces in the slurry stream[39]. The hydro cyclone was patented in 1912 and has subsequently been widely used in the minerals processing industry as a classifier for size separation in the mineral extraction process. Its widespread use is due to its ease of operation, high capacity and efficiency.

Figure 2.9a displays the working principle of a hydrocyclone. A feed enters the tangential inlet at a high velocity near the top of the cylindrical section. The fluid is pushed towards the bottom in a spiralling fashion where it experiences a flow reversal and passes up as a central core. This central core actually flows toward a central overflow outlet in a reverse spiral.

The conventional understanding is that particles within the hydrocyclone's flow pattern are subjected to two opposing forces: an outward acting centrifugal force and an inward acting drag displayed in figure 2.9b. The centrifugal force developed accelerates the settling rate of the particles, thereby separating particles according to size, specific gravity and shape. Faster settling particles move to the wall of the cyclone, where the velocity is lowest, and migrate down to the underflow. Due to the action of the drag force, the slower settling particles move toward the zone of low pressure along the axis and are carried upward through the vortex finder to the overflow.[17]

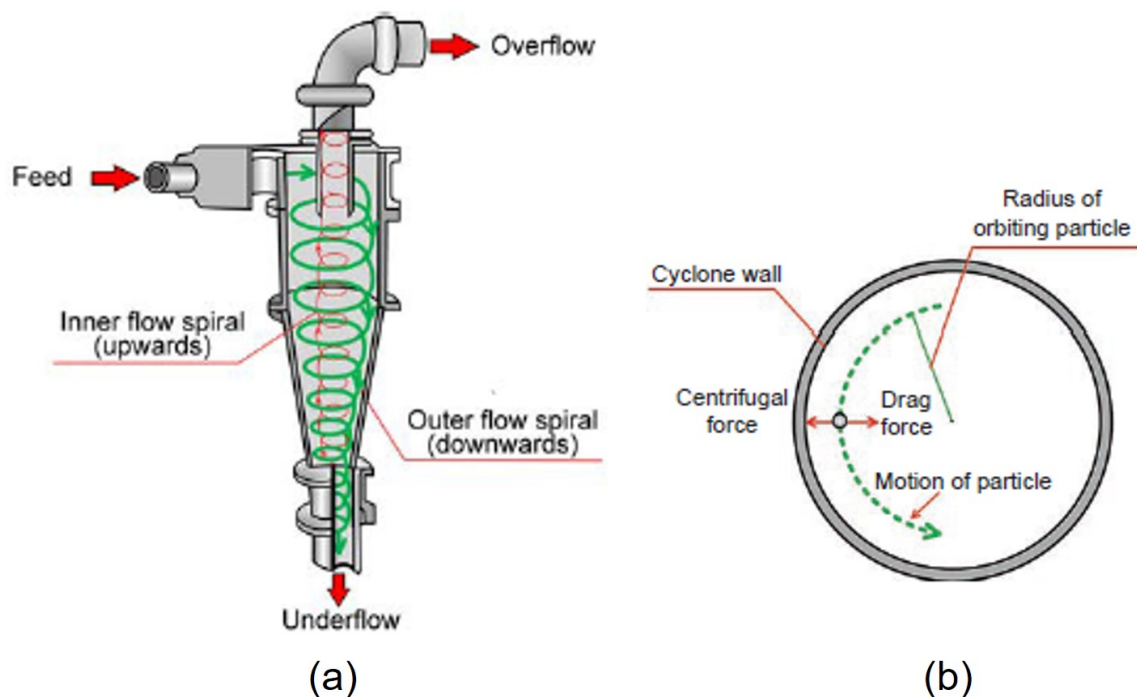


Figure 2.9: Hydrocyclone: (a) Principle flows. (b) Forces acting on an orbiting particle (JKMRC, The University of Queensland).

Table 2.4 outlines the critical differences between the two types of classifiers and further highlights the benefits of centrifugal classifiers: Due to the continuous feed, the capacity is not limited by the size of the sedimentation tank. The centrifugal force causes another advantage: smaller particles can be separated in a shorter time. A disadvantage of the centrifugal classifier is the energy consumption because of the high feed pressure required to achieve the separation

vortex. However, one can argue that the energy consumption disadvantage is outweighed by the small deck space requirement, initial investment costs and the robustness of the system[40].

Table 2.4: Differences between centrifugal and gravitational classifiers[17].

Item	Centrifugal Classifiers	Gravitational Classifiers
Capacity	High	Low
Cut-size	Fine-Coarse	Coarse
Capacity/cut-size dependency	Yes	No
Energy consumption	High(feed pressure)	Low
Initial investment	Low	High
Required area	Small	Large

Coagulation and flocculation

Coagulation and flocculation refer to processes that cause particles to aggregate or agglomerate (i.e., adhere or cluster together) to increase settling rates. To achieve this increased settling rate, chemicals need to be added to the slurry. These chemicals will increase the operational costs and can cause environmental impact if not carefully handled and separated from the waste stream. When looked at the reports of Blue Nodules (deep sea nodule mining at the CCZ) and Chatham Rock Phosphate Limited (mine phosphorite crest near New Zealand), it shows that the use of chemicals in their topside processing is not preferred[8, 28].

2.2.2 Filtration

Filtration is a process used to separate solids from liquids or gases using a filter medium that allows the fluid to pass through but not the solid[41]. Figure 2.10 shows this method in a basic diagram. This section is divided into a part about a vibrating screen and a filter press.

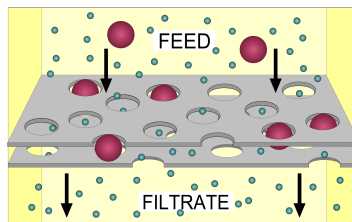


Figure 2.10: Diagram of filtration: oversize particles in the feed cannot pass through the lattice structure of the filter, while fluid and small particles pass through, becoming filtrate.

Vibrating plate

Vibrating dewatering screens are commonly used for solid-liquid separation applications in several industries such as mining, chemical and food. Materials such as sands, ores, pyrites, salts, coal, silt, granulates, abrasives and recycling materials, are commonly dewatered using vibrating screens[17, 42]. A more widespread application of vibrating screens is for size classification, especially in the mineral industries[43, 44].



Figure 2.11: Example of a vibrating dewatering screen[6].

Figure 2.11 shows a vibrating dewatering screen as used in the industry. A vibrating motor produces the vibration of the screen deck. The slurry is fed on one side of the screen. The water passes through the screen openings while the solids are conveyed to the other end of the screen. The vibration aids in the conveyance of solids. Sanjay et al.[16] experimented with the dewatering of nodules using a vibrating screen. The experimental results indicate that the dewatering screen was able to separate particles $>1\text{mm}$ effectively, leaving the underflow with only fine particles of size $<1\text{ mm}$. The angle of screen inclination was found to be the most influential parameter, followed by the flow rate.

While construction and operation of dewatering screens is simple, the theory is rather complex. With the lack of constant operating force like in centrifugal separators or pressure filters, the physics of solids dewatering can be closely modelled as a discontinuous centrifugal force. The vibrations of the screen offer acceleration and deceleration at short intervals. This force is responsible for the removal of the moisture associated with the solids besides the associated free water[45]. Other factors such as inclination also play a significant role. On an inclined dewatering screen, the accelerations along with a portion of the gravitational force will cause the material to travel towards the discharge end. In contrast, the water is being screened out utilizing proper screening media.

Filter press

For the separation of small particles like micronodules ($<0.5\text{ mm}$), a filter press could be used. A frequently used horizontal filter design is shown in figure 2.12. Filter plates are suspended vertically from a steel frame, with a filter cloth hung between them. The plates are held together, and the press is opened and closed by a hydraulic piston. The slurry is pumped into the press to fill each chamber. Dewatering starts immediately, and the filtrate

is removed. When the chamber is full of material, membranes on one side of the chamber are pressurized to hold the filter cake in place and squeeze out water. At the end of this “feeding cycle”, the main dewatering cycle is activated by forcing pressurized air through the cake; this pushes the water out with pressures typically around 8 bar. At completion, the press is opened, the plates separate, and the cake falls by gravity onto a conveyor. Afterwards, the chambers close, and the cycle repeats.



Figure 2.12: Example full scale filter press, the pressing takes place in the vertical white plates. (Dutch filtration).

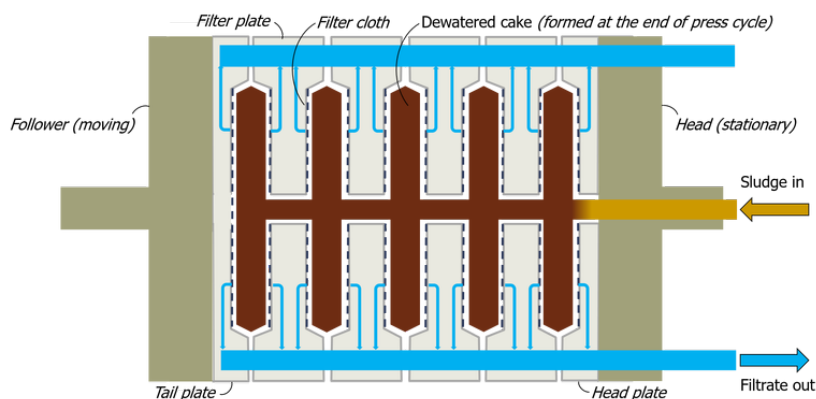


Figure 2.13: Schematic view of filter press (Judd Water & Wastewater Consultants).

A filter press operates with batches of slurry and thus cannot operate continuously. This is a problem for a mining operation where the feed stream enters continuously. If a buffering tank is positioned before the press, a continuous process can be mimicked. The downside of this solution is that large reservoirs are needed when considering processing volumes on a nodule mining operation [46]. Another way to make the system more continuous, is placing multiple filter presses in parallel. When press 1 is loading, press 2 can be unloading, this reduces the necessity of a feeding tank and thereby save space on the mining support vessel[16].

The largest disadvantage of the filter press is the energy consumption[17]. Since the fines only represent a small percentage of the production. It is questionable whether it is cost-effective to use this machine in the dewatering of the nodule slurry.

2.2.3 Thermal drying

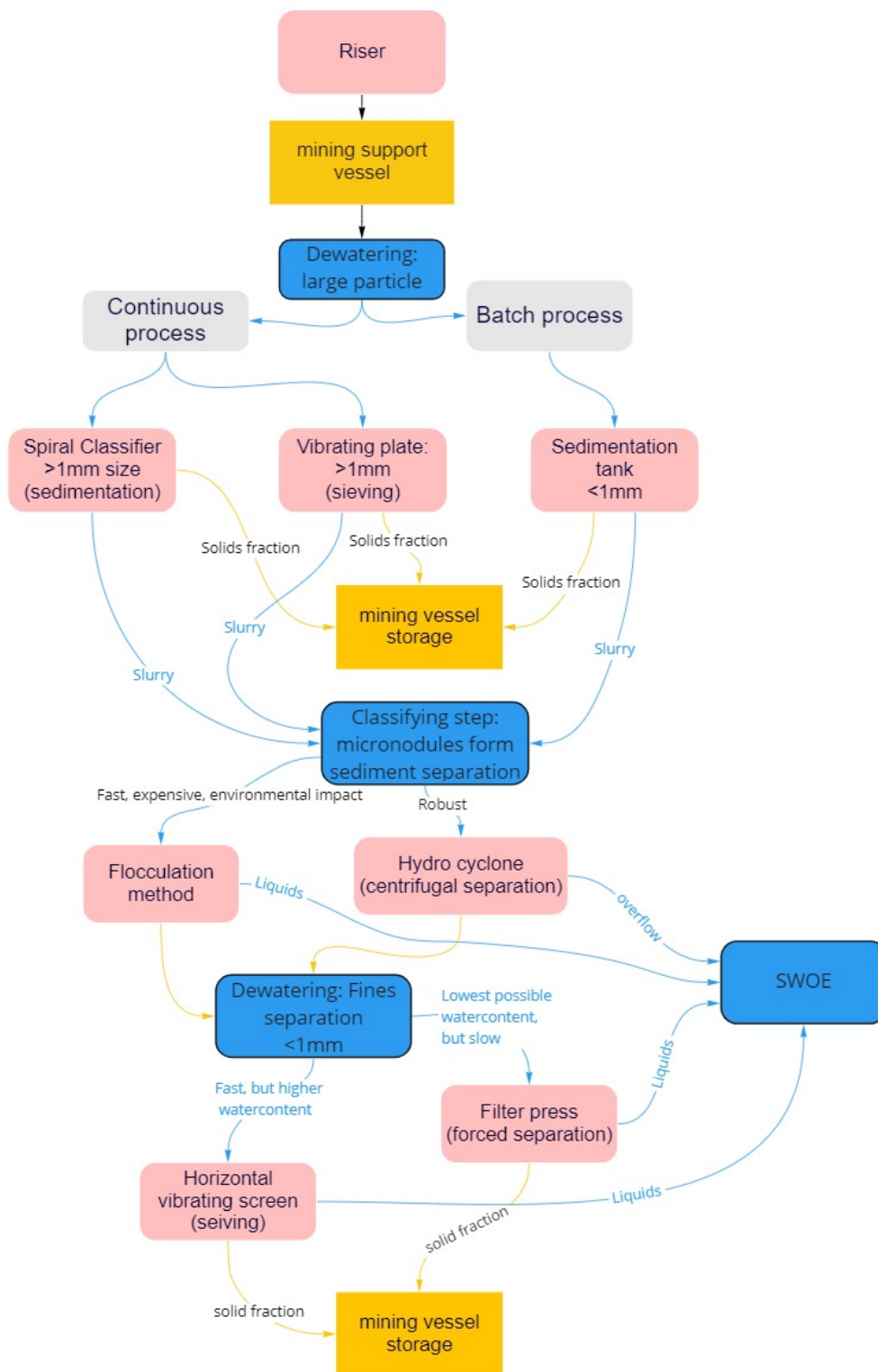
Thermal drying is a process for the dehydration of moist products based on moisture evaporation by heating. This method is used if processes require low moisture content (5%wt), for example iron ore pellet creation [42].

2.2.4 Overview of dewatering strategy at sea

A dewatering flowchart containing the different methods of dewatering from the previous sections is depicted in figure 2.14. The flowchart aims to help create a dewatering system for a manganese nodule mining operation. The flowchart starts at the point where the nodules enter the mining support vessel. A choice is made if the nodules will be processed in bulk or as a continuous process. The availability of space on the ship is the governing parameter in this choice. The next step is removing the free water surrounding the nodules, a coarse separation step where the nodules > 1 mm will be removed from the water. The separated nodules are transported to the mining vessel storage, while the remaining water with fines (nodules fragments and micronodules) and sediment is transported to be further processed.

The next step is classification: the goal is to separate the micronodules from the sediment as much as possible. The most effective way of separation would be a flocculation method. However, due to the costs of chemicals and the potential environmental impact, this method is not recommended. The hydrocyclone is a better option because of its ease of use and robustness. The only drawback is the separation efficiency which cannot prevent that, to some extent, sediment particles will stay in the fines stream and some fines will end up in the discharge stream. After classification, the separated sediment will be transported to the SWOE, and the fines stream will continue to the last step.

The last step is the fines-water separation. For the method of fines separation, it is essential to know to what extent dewatering is necessary. Section 4.3.3 elaborates more on this topic. In this dewatering step, a fine vibrating screen or a filter press could be used. The vibrating screen is the fastest and cheapest method, and the filter press is the most effective dewatering method but is more expensive. The dewatered fines can then be transported to the mining vessel storage, and the removed water will be sent to the SWOE.



miro

Figure 2.14: Detailed flowchart of the possible dewatering process. The pink colour represents the hardware where the separation takes place. The yellow colour represents states the location of the product.

Concept dewatering strategies from the offshore mining industry

Multiple companies are conducting research on the ways of dewatering on the mining support vessel. Unfortunately, these concepts are often kept away from the public domain to not help the competitors. This self-protection makes it difficult to find literature on offshore dewatering installations. Currently, two consortiums have released their information, the research and innovation project: Blue Nodules[7] and Chatham rock phosphate limited[8]. I created an overview of the two dewatering setups in figure 2.15. Chatham rock phosphate did not state the exact overview. This overview is reconstructed by scanning the dewatering setup overview figure (shown in Appendix A.1) from their report. This overview is useful to test the flowchart of figure 2.14.

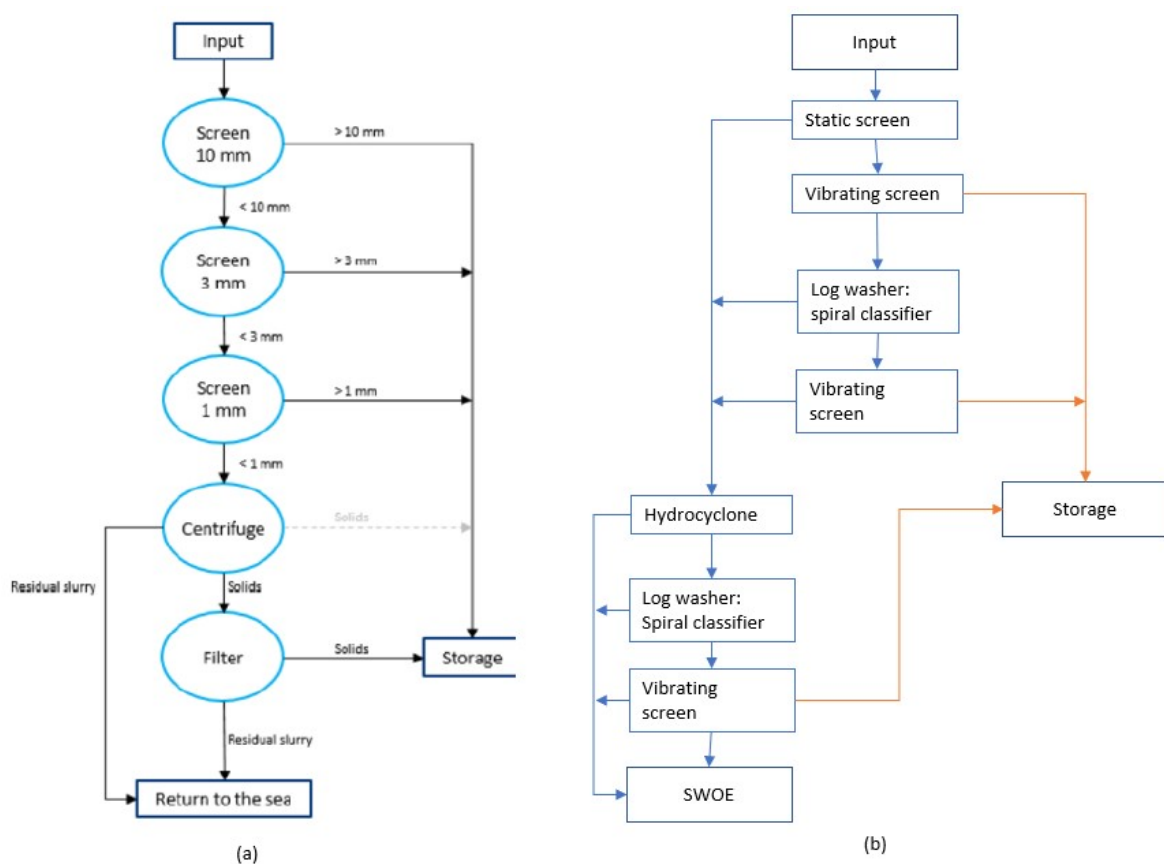


Figure 2.15: (a) Shows the proposed dewatering setup of Blue nodules[7] and (b) Shows the proposed dewatering setup of Chatham Rock Phosphate Limited[8].

2.2.5 Dewatering on land or at sea

Dewatering on land

Multiple land-based industries rely heavily on dewatering. The mining industry can be taken as an example. Most mineral-separation processes involve the use of substantial quantities of water, and the final concentrate has to be separated from a pulp in which the water–solids ratio may be high. Dewatering produces a relatively dry concentrate for shipment[17].

The optimisation goals of dewatering on land can be different than on sea. The upgrading of iron ore is, for example, a high-tonnage industry where cost efficiency plays a critical role[47]. On the sea, the space usage and power consumption are most likely optimised. The amount of reduction in moisture content can be another difference, especially in iron ore processing, where low and even cake moisture content is crucial for the following palletisation[17]. This requirement is stricter than for a deep sea mining operation where the governing dewatering factor is the transportable moisture limit for transport.[7, 30]

Dewatering at sea

On a vessel, the separation processes are more complex due to four challenges. Firstly, the availability of volume and deck space on a ship is limited. Secondly, the slurry inflow is most likely continuous throughout the day (highest TRL as is depicted in figure 2.3), so a batch separation installation is not preferred. thirdly, the motion of the mining vessel makes the fixed environment turn into a dynamic environment which makes specific separation steps like sedimentation inefficient[40, 48]. Lastly, the availability of power is expensive and not limitless onboard a ship which makes filter presses less interesting to use.

2.3 Effects of water on material properties of nodules in bulk

The changing of the bulk properties of polymetallic nodules during transport and in the cargo hold depends moisture content of the nodules and the change in particle size distribution from impacts in the VTS. This chapter focuses on the moisture content in the nodules. The first section of this chapter states the nodule parameters. This section is followed by the three regimes which the nodules encounter on their way from the seabed to the storage.

Single nodules

We start by analysing the physical properties of single nodules. Dreiseitl & Bednarek [18], Neizvestnov et al. [49], Mero [21], Glasby [50], Zenhorst [51], Halbach [52], Wijnands [53] and GSR [26] have published studies on the nodules properties. Table 2.5 displays the results of the material properties of 205 Nodules obtained from the Clarion Clipperton Zone at location H22 (Figure 1.3). To understand this table properly, the physical properties have to be explained first.

- Volumetric density (moist unit weight), $\rho_{situ} [g/cm^3]$, is defined as the ratio between the mass of a nodule, including air and water present, $m_w [g]$, and its volume, $V [cm^3]$.

$$\rho_{situ} = \frac{m_w}{V} \quad (2.1)$$

- Dry nodule density (dry unit weight), $\rho_d [g/cm^3]$, is defined as the ratio between the nodule mass without water, $m_d [g]$, and the total volume (including voids) of nodule $V [cm^3]$.

$$\rho_d = \frac{m_d}{V} \quad (2.2)$$

- Water content, $w [\%]$, is the amount of water contained in a nodule; it is expressed in terms of the mass of water evaporated at 105 °C, $m_w - m_d$, per mass of dried nodule m_d .

$$w = \frac{m_w - m_d}{m_d} \quad (2.3)$$

- Natural water content, $w_n [-]$, is expressed as the mass of water evaporated at 105 °C, $m_w - m_d$, relative to the mass of a wet nodule sample m_w .

$$w_n = \frac{m_w - m_d}{m_w} \quad (2.4)$$

- Porosity, $n [-]$, represents the ratio between the volume of voids (spaces) to the total volume of material.[54]

$$n = w \left(\frac{\rho_d}{\rho_w} \right) \quad (2.5)$$

- Void ratio, e [-], expresses the relationship between the volume of voids and the volume of solids in a nodule.

$$e = \frac{n}{1 - n} \quad (2.6)$$

- Specific (solid particles) nodule density, $[g/cm^3]$

$$\rho_s = \rho_d(1 + e) \quad (2.7)$$

The relevant properties are determined in both shipboard and land-based laboratories. The shipboard analyses include nodule volumetric density and water content, determined immediately after the samples were retrieved.[18]

Table 2.5: Nodule properties of 205 Nodules samples taken from the Clarion Clipperton region, location H22 [18].

Parameter		Unit	Mean	Median	Maximum	Minimum	Av deviation
Water content	w	[%]	46	46	57	36	3.48
Wet density	ρ_{situ}	$[g/cm^3]$	1.97	1.98	2.06	1.83	0.04
Dry density	ρ_d	$[g/cm^3]$	1.35	1.36	1.51	1.18	0.06
Porosity	n	[%]	61	61	66	53	2.21
Void ratio	e	[-]	1.57	1.58	1.96	1.14	0.14
Mineral density	ρ_s	$[g/cm^3]$	3.46	3.52	3.68	2.98	0.13
Natural water content	w_n	[%]	32	32	37	27	1.65

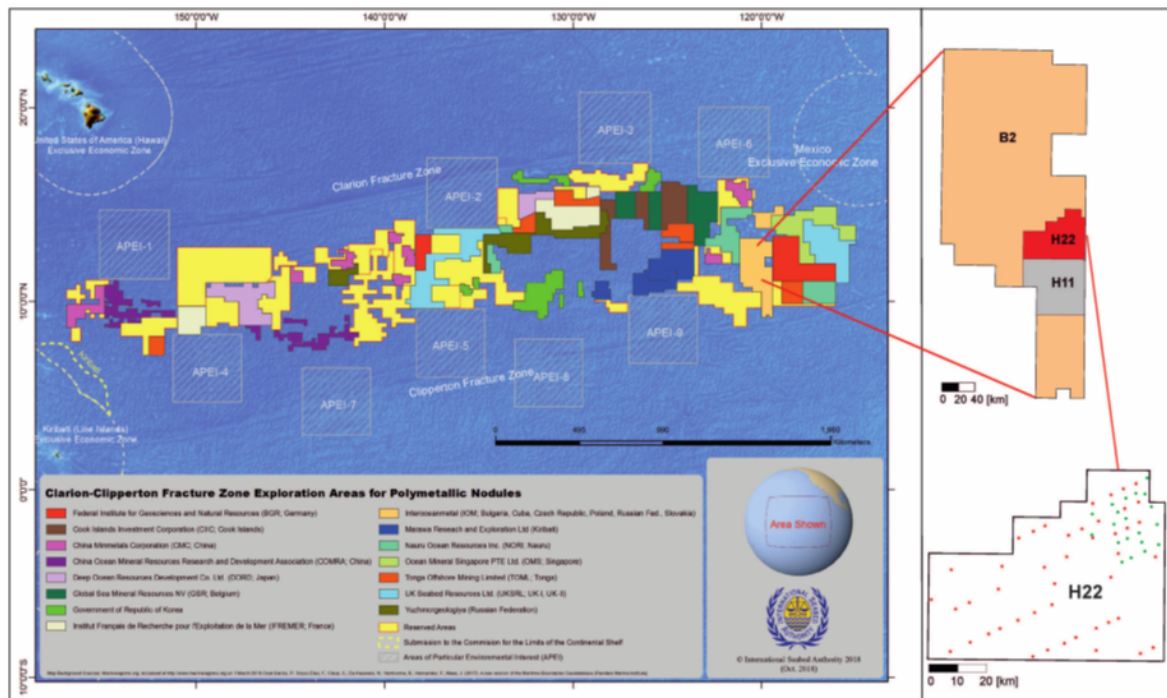


Figure 2.16: The Location of B2 InterOceanmetal Joint Organization (IOM) area and H22 and H11 exploration blocks against the background of Clarion–Clipperton Zone Exploration Areas for Polymetallic Nodules[9].

Definable regimes of nodule processing at sea

In the topside processing of the nodules, three different types of regimes can be defined. The first regime consists of solids in a liquid stream. This regime could be described as a slurry and comprises the material as it enters the production support vessel. Dewatering steps are applied to the slurry, and ‘dry’ bulk is formed. However, this dry bulk is not completely dry; only the free water around the nodule is removed. The nodules themselves are still saturated with water. The last regime might form in the bulk hold of the ship: Due to the bulk handling and weight of the nodules, pressure will build up in the nodules, and the saturated nodules could lose some of the pore water in the time-span of the shipment to the shore [12]. Figure 2.17 displays a schematic overview of the different regimes.

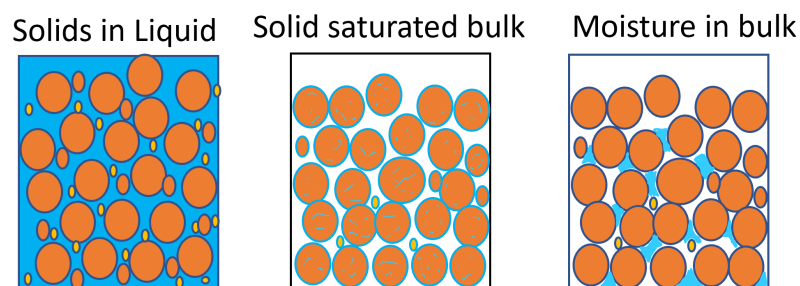


Figure 2.17: Schematic overview of the three regimes which the nodules will encounter during the journey from the riser system to the ship storage.

2.3.1 Solids in slurry

The first “solids in slurry” regime is valid wherever the nodules are in suspension. This regime applies to the nodules larger than 1 mm in and just after the vertical riser transport system and applies to the fines (< 1 mm) until they are removed from the water in the last dewatering step. During this process, several physical processes play an essential role. The settlement velocity equations are the governing equations for the design of the system. To understand this equation, some other equations have to be understood: Mass concentration, volumetric concentration and slurry density. These equations are important for the dewatering stages and the transport through the pipeline: If the values reach levels which are too high, pipelines can clog. Furthermore, sedimentation dewatering systems can have problems with a phenomenon called hindered settling. This will be explained in the next section.

The mass concentrations:

$$c_m = \frac{m_s}{m_{total}} \quad (2.8)$$

Where m_s represents the total mass of the particular solids and m_{total} represents the total mass of all the solids and water combined.

The volume concentration:

$$c_V = \frac{V_s}{V_{total}} \quad (2.9)$$

Where V_s represents the total volume of the particular solids and V_{total} represents the total volume of all the solids and water combined.

Slurry density:

$$\rho_{mix} = c_v * \rho_s + (1 - c_v) * \rho_l \quad (2.10)$$

ρ_{mix} is the density of slurry in g/cm^3 , c_v is the concentration of solids by volume in the slurry in fraction. ρ_s is the density of the solids in g/cm^3 and ρ_l is the density of liquid without solids g/cm^3 .

Settling and hindered settling

The settling rates of particles in a fluid are governed by Stokes' or Newton's laws.[55] Factors that affect sedimentation include: particles size and shape, weight and volume content of solids, fluid viscosity, and specific gravity of solids and liquid. Very fine particles, of only a few micrometers diameter, settle extremely slowly by gravity.

Equation 2.11 shows the settling equation.

$$v_{ts} = \sqrt{\frac{4(\rho_s - \rho_f)gd}{3\rho_f C_D}} \quad (2.11)$$

With v_{ts} is the terminal settling velocity, and C_D is the drag coefficient of flow around a particle. The drag coefficient C_D is sensitive to a regime of the liquid flow round the settling solid particle and this can be expressed by a relationship $C_D = \text{fn}(Re_p)$. Therefore, the terminal settling velocity v_{ts} depends on the particle Reynolds number Re_p (eq 2.12), which itself also depends on the velocity of a particle. An empirical equation or iteration is required to come to a constant value. Terminal settling velocity v_{ts} is used as the first input for

calculation of the particle Reynolds number, in which ν the kinematic viscosity of the liquid, in this case water.[4]

$$Re_p = \frac{v_{ts} * d}{\nu_f} \quad (2.12)$$

The hindered terminal settling velocity v_{th} , this calculated by using Eq.(2.13), as given by Richardson & Zaki [55]. The dependency on the Reynolds factor is expressed in the exponent n , for which Eq. (2.14) was suggested by Wallis [55]. The obtained value of the hindered terminal settling velocity is then used to recalculate the particle Reynolds number Re_p , using Eq. (2.11) again with v_{th} replacing v_{ts} . The cycle repeats until a constant value for the hindered terminal settling velocity v_{th} , this reached.

Hindered settling

$$v_{th} = v_t(1 - c_v)^x \quad (2.13)$$

$$x = \frac{4.7(1 + 0.15Re_p^{0.687})}{1 + 0.253Re_p^{0.687}} \quad (2.14)$$

This settling equation is defined spherical particles. The problem with assumption is that most particles are not perfectly round. Particles which are more flat than round, will have a tendency to settle at a different velocity than spherical particles. This where the shape correction factor shows up. The correction factor, which shows what the particle's diameter would be if it were a spherical shape and so that terminal settling is overestimated.

$$\psi = \frac{v_t}{v_{ts}} \quad (2.15)$$

In which ψ is the correction factor for the shape of a solid particle and the v_t is the settling velocity of a non-spherical solid particle. The correction factor has to be found experimentally for nodules.

2.3.2 Granular behavior

When handling bulk cargo, it is important to know how they behave to have a safe and efficient operation. Solid bulk cargoes are typically loosely packed granular materials. A useful parameter is the bulk density. The bulk density depends on the material properties and loading conditions (grain size distribution, moisture content, drop height, cargo depth, loading rate and time between loading and shipping)[7]. Furthermore, for the modelling granular material like polymetallic nodules, the angle of repose is a valuable parameter.

Angle of repose

The angle of repose is regularly measured in laboratory tests and DEM models as a quick method to determine the flowability of a granular material and to calibrate DEM material parameters, such as the static friction, rolling friction and particle shape[56].

When a bulk solid material is experiencing a free surface flow, its surface forms an angle. This angle, which is referred to as the angle of repose, usually measures the maximum slope

angle of bulk solid material between a horizontal plane and the free surface angle. The angle of repose represents the shear strength of bulk solid materials. According to the Mohr-Coulomb equation, the shear strength of bulk solids materials in a failure plane, τ_s is often approximated by Eq 2.16[57]:

$$\tau_s = \tau_c + \sigma_\alpha \tan(\alpha) \quad (2.16)$$

Where $\tan(\alpha)$ indicates the friction coefficient of the bulk solid. σ_α is the normal stress in the failure plane, and τ_c denotes the cohesion of the bulk material: In other words, τ_c is the shear strength of the bulk material if $\sigma_\alpha = 0$. By increasing σ_α , due to increasing the height of bulk solids material for instance, it is expected that the contribution of τ_c in the shear strength decreases. When τ_c is negligible, angle of repose represents α mainly. Failure will occur once shear stress in an arbitrary cutting plane exceeds the shear strength of the bulk material. The remaining bulk solids in the box forms an angle of repose. This parameter represents the shear stress of bulk material under the force of gravity. Therefore, angle of repose, can be used to investigate the effect of type and moisture content of polymetallic nodules on its free surface flow.

Bulk density and angle of repose from literature

Nodule bulk density, ρ_b [g/cm^3], provides information on the amount (by weight) of nodules that can be placed in a 1 m^3 container. Maximum nodule bulk density, $\rho_{b,max}$ [g/cm^3], is obtained when a container of nodules is shaken and refilled. The bulk density and angle of repose are best determined when many nodules (hundreds of kilograms) are collected by seafloor dredge and delivered onboard [18].

Four dredge-samples were carried out within an expedition in 2014, with 2309 kg of nodules being retrieved onboard. Likely, the three parameters presented in table 2.6 will be not of any practical use because the nodules are recovered via a hydraulic method of collection and transport and thus will degrade during the transport through the vertical transport system [5]. However, they can have a significant relevance as comparison material for bulk properties taken from degraded nodules.

Table 2.6: Bulk properties retrieved from four dredged samples of an expedition in 2014 with 2309 kg of nodules being retrieved[18] using mainly intact nodules. The values can have a significant relevance as comparison material for bulk properties taken from degraded nodules.

Dredge No.	Nodule apparent density ρ_b [g/cm^3]	Maximum nodule bulk density $\rho_{b,max}$ [g/cm^3]	Angle of repose α [deg]
2229 Tp-1	1.136	1.250	33
2229 Tp-1	1.121	1.220	33
3521-1 Tp-1	1.106	1.242	30
3521-1 Tp-2	1.068	1.205	30

Aspect ratio

The shape of the granular material also has influence on the bulk parameters. For the modeling the shape in DEM software, the aspect ratio can be useful tool. The particle elongation is defined as illustrated in figure 2.18, by the ratio b/a (e.g. aspect ratio AR), where b is the length of the minor axis and a is the length of the major axis [58]. For a spherical particle $AR = 1$, the higher the particle elongation the smaller the ratio AR. The ratio is limited to a value of $AR = 0.5$ because the spheres will not touch at lower values. For particles which are needle shaped, which have a $AR < 0.5$, sphero-cylinder modeling could be used.[59]

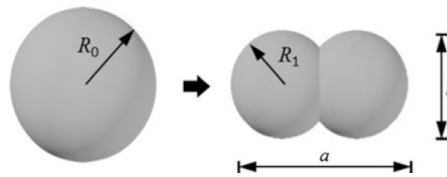


Figure 2.18: Definition of particle aspect ratio AR. For Spherical particles, the Aspect ratio is 1[10].

Particle degradation

From the nodule degradation experiments from van Wijk and de Hoog [5, 35] and Li [60], the conclusion can be drawn that there will be a significant degradation during the transport of the nodules. Particle degradation is known as the breakage of a single particle in multiple pieces or as the mass loss of the parent particle. It is helpful to get an understanding of the different mechanisms of nodule degradation.

Particle degradation can be divided into four failure mechanisms based on the physical effects on the particles[11]. The mechanisms are fragmentation, chipping, attrition and abrasion. The four mechanisms are subdivided into high force fracture mechanisms and low force wear mechanisms. Figure 2.19 shows an overview of the different failure modes. A particle can break by fragmentation, where a crack propagate goes through the particle and will divide the particle into two or more pieces. Fragmentation occurs when a relatively high normal force is exerted on a particle, for example, a centrifugal pump blade on a nodule. Chipping occurs when a relative high tangential force is exerted on the particle. Chips will break loose from the particle. A particle can also degrade by wear mechanisms as attrition or abrasion. Attrition occurs when relatively low normal forces are exerted on the particle, and abrasion occurs when relative tangential forces are exerted. In both mechanisms, the particle loses its mass gradually, but a significant difference is that surface by abrasion is getting smoother and rounds the particle in contrast with attrition.


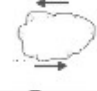
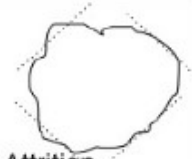
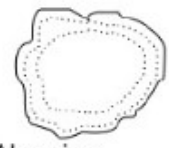
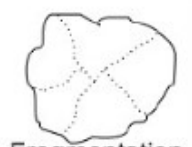

Magnitude	Direction	
	Normal	Tangential
		
Low force <i>"Wear"</i>	 Attrition	 Abrasion
High force <i>"Fracture"</i>	 Fragmentation	 Chipping

Figure 2.19: Particle degradation mechanisms [11].

Particle properties that are of significant influence on particle degradation are: size, shape and (loading) history. A larger particle contains more structural impurities compared to smaller particles. Hereby the particle strength of smaller particles is higher than larger particles. The particle shape influences the stress distribution in the particle. A more irregular particle is more exposed to wear due to its sharp edges. The small edges will experience high local stresses resulting in a higher fracture probability. [61].

2.3.3 Moisture in coarse granular material

Each year, accidents happen, with bulk carriers capsizing or sinking due to excessive moisture levels in the loads. In the period 2009-2015, 11 ships were lost in this way, with 102 crewmen losing their lives. Load liquefaction or dynamic separation were identified as the likely cause of these accidents. The most widely-known cargoes which are susceptible to liquefaction, are mineral concentrates, but also other materials such as fluorspar, certain grades of coal, pyrites, mill scale or sinter/pellet feed are known to be susceptible to liquefaction.[2, 12, 62]

Liquefaction

Liquefaction has been studied thoroughly in soil mechanics literature, mostly in relation to earthquakes. Liquefaction can typically occur in non-cohesive granular soils, which are relatively fine grained, loosely packed and saturated with water [62]. When a load is applied on a loosely packed granular material it tends to compact. When the voids (expressed in figure 2.20 as void ratio, e_v , i.e. the ratio between the volume of voids and the volume of solids) are filled completely with water, the water needs to be expelled in order to allow compaction. If the drainage capacity of the soil is limited, pore pressure, p , will increase as water is relatively incompressible. When the pore pressure rises to a level that all the load, σ_T , is completely carried by the water, the effective stress, σ' , between the grains reduces to

zero.

$$\sigma' = \sigma_T - p \quad (2.17)$$

The shear strength, τ , which prevents the grains to move, is a function of the cohesion, τ_c , and friction, in which the latter depends on the effective stress and the angle of internal friction, α , which is a material parameter depending e.g. on the material roughness.

$$\tau = \tau_c + \sigma' \tan (\alpha) \quad (2.18)$$

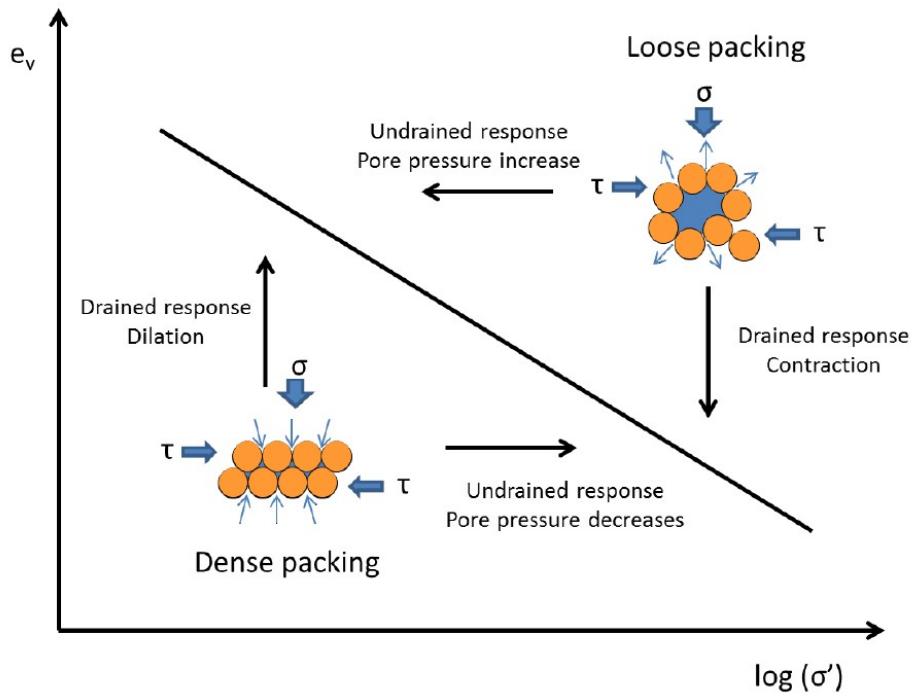


Figure 2.20: Susceptibility to liquefaction is related to the relative density of a material: Loosely packed granular materials tend to contract when loaded. Undrained conditions lead to an increase in pore pressure.

When the effective stress in a non-cohesive granular soil reduces to zero, the grains lose contact, and the soil can no longer resist shear stress and starts behaving like a liquid. Fine-grained, cohesive soils are considered less susceptible to liquefaction as cohesion between the grains provides shear resistance. Coarse-grained soils are also less susceptible to liquefaction as the high permeability allows water to drain and prevents pore pressures to build up. The relative density of granular soils significantly affects the susceptibility for liquefaction. Densely packed granular soils are less susceptible to liquefaction, as the densely packed particles need to dilate to a looser packing in order to move. In order to dilate, water needs to fill the increasing void space, which in case of limited drainage leads to a reduction in pore pressure, increasing the effective stress between the particles and consequently increasing shear strength (Figure 2.20). Partly saturated soils are also less susceptible to liquefaction. As the air which is present in the voids is highly compressible, the increase in pore pressure will be limited.[2]

Solid bulk cargoes are typically loosely packed granular materials. The bulk density depends on the material properties and loading conditions (grain size distribution, moisture content, drop height, cargo depth, loading rate and time between loading and shipping). When the cargo is wet during loading, it might be susceptible to liquefaction. In most cases, the payload is not fully saturated with water when loaded, but it can become saturated due to compaction or drainage. Continuous loading cycles imposed by ship movements can cause the loosely packed cargo to compact. The remaining air in the void spaces between the ore grains is compressed and squeezed out, increasing the water content. When the water content approaches saturation, pore pressures may rise and induce cargo liquefaction. A rolling movement may cause the liquefied cargo to flow to one side of the ship and not completely return with a roll the other way. The progressive shift of cargo may cause the ship to list and eventually to capsize. Although shifting cargo is mostly attributed to liquefaction, it can also occur before the ore is fully liquefied due to a partial loss of shear strength. Failure occurs when the stresses imposed by the cyclic load exceed the shear resistance.

Dynamic separation

For the cargo to undergo dynamic separation, it must have considerable amount of fines particles, high moisture content and experience sufficient forces due to vessel motions. If all of these factors are present, the cargo, that was initially a pile, will compact, pore water pressures will increase, but not to liquefaction levels, causing moisture to be expelled to the cargo surface [12] .

The process of dynamic separation can be seen in figure 2.21.

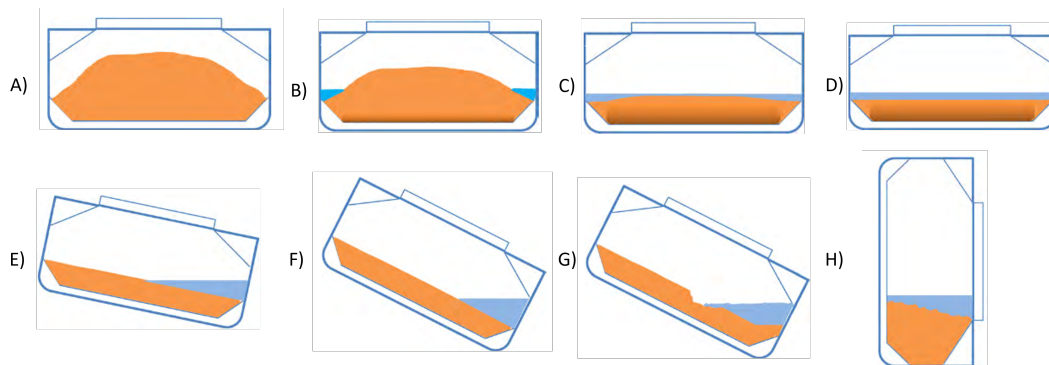


Figure 2.21: Schematic depiction of the steps for dynamic separation.[12]

- A The cargo is loaded into the vessel to form a pile of cargo with a given geometry, bulk density and moisture content.
- B Cargo compaction due to ships motions results in the cargo increasing in its bulk density via compaction and moisture migrating to towards the bottom of the cargo pile. Once the moisture content at any location in the pile reaches a critical level, the dynamic forces on the cargo cause the pore water pressure to increase. This increase in pore water pressure cause moisture to flow to the nearest low pressure, which in the case of the bauxite loaded pile, is to the nearest surface at the pile corner/bulkhead/wall boundary. The flow of water continues resulting in the separation of the cargo moisture

from the solid cargo. The solid cargo at the bottom of the pile is now significantly drier and unsaturated, has gained in strength and is more competent than the as loaded cargo

- C Continuation of moisture separation, cargo slumping and erosion of the cargo pile. Free slurry surface that is perched above the solid cargo extends the full width of the cargo hold.
- D the cargo had dynamically separated to form a flat, solid and competent cargo with a perched free surface slurry layer on top, the ramifications of this scenario are explored further.
- E Full ship's beam free slurry surface causes the vessel to lose initial stability. The vessel develops a list to regain stability. The free slurry surface is now less than ships beam. The bulk of the cargo underneath the slurry layer remains competent and intact.
- F The vessel list now gradually increases as the slurry increases in its solid fraction and density as more particles are entrained in the liquid and solids are deposited to the lower end of the hold.
- G Vessel motions make the slurry slosh and erode the flat competent solid cargo until it becomes undercut. Sloshing of the slurry also increases the solids content and hence density of the slurry, so the vessel list progresses.
- H The competent solid cargo in the upper end of the hold suddenly shifts to the lower end causing a catastrophic roll and capsizing. This sudden avalanche may occur as the angle of repose of the cargo is exceeded due to the vessel's rolling about the heel position and/or by erosion by the sloshing slurry as the compact cargo is undercut and the denser slurry increases the heel angle.

Like liquefaction, the process of dynamic separation can be prevented by ensuring that the cargo has limited fines content and a limited moisture content, as both particle size distribution and moisture content are the main parameters for the occurrence of this phenomenon.

Transportable moisture limit

As mentioned in the last section, there are two ways to reduce the risk of cargo instabilities: Reduce fines or reduce the moisture content. For most bulk cargoes, it is not feasible to reduce the fines. Only the moisture content is a variable parameter. To ensure safe transport of bulk cargo, the transportable moisture limit is created: The Transportable Moisture Limit (TML) of a cargo indicates the maximum moisture content of the cargo which is considered safe for carriage. The actual moisture content of the cargo at the time of loading will be measured and compared with the TML.

The TML is taken as 90% of the moisture content that is necessary for liquefaction to be possible, based on laboratory testing. This means that a safety margin is provided to protect against variations in cargo properties and moisture content, and against measuring errors in determination of the TML or actual moisture content [12].

Test to determine TML

The TML is determined based on the Proctor Fagerberg Test (PFT), a standard compaction test according to ASTM Standard D-698, except lighter hammers are used to achieve the densities that would occur in the ore materials when loaded into the ship. The TML is taken as equal to the moisture content obtained at 80% degree of saturation from the relevant PFT [63]

Result TML test literature

The first TML tests were conducted on a sample of 40 kg nodules, by Bureau Veritas. As a first step, the as-received moisture content was determined. Surprisingly, while looking dry, they still contained a moisture content of 26.2% (after two years of storage in a dry location).

A first set of tests were executed, determining the TML of the nodules to a (first, preliminary) TML value of 35.3%. This value will evolve in the future, after more insight in the mining process is gained[7]. It is interesting to notice the minimal difference between this TML value and the moisture content from the nodule parameters table 2.5: An average moisture content of 46% of intact nodules. This value is higher than the TML but when taking into account the void space between the nodules in bulk, the average moisture content will be lower. It can be concluded that when there are enough fines in the storage hold to fill the voids between the nodules, it is essential that the dewatering stage is thorough to ensure dynamic separation and liquefaction phenomena are avoided.

2.4 Conclusion

What are effective strategies to dewater polymetallic nodules in a confined space on a mining support vessel?

- Figure 2.14 shows an overview of an effective dewatering strategy for nodule harvesting operation.
- The dewatering process of polymetallic nodules results into two streams. The first one is a stream of dewatered solids, because “free” water has been removed from around the nodules using vibrating plates and screens. Hence, the second stream is runoff water, potentially still rich in fines and sediment, of which separation of fines may still be economically viable. However, economic feasibility was not included in the scope of this research. These fines can be removed using hydrocyclones and filter presses.
- The extent to which dewatering processes are necessary depends mainly on the allowable maximum moisture content and the number of fines present in the storage of the mining support vessel and the bulk carriers. Moisture maximum prevents processes such as liquefaction and dynamic separation.

How do the dewatering strategies at sea compare to land based dewatering installations?

- There are four significant differences between dewatering installations on land and at sea.
 - Space on a ship is limited, so the layout must be more compact in comparison to land.
 - The static environment on land has turned into a dynamic environment at sea. This ensures that gravity sedimentation will have problems with the separation of the fines due to flows in the sedimentation tank.
 - The production of the mining vehicle will be continuous, making batch dewatering and separation methods impractical.
 - The mining support vessel has a limited amount of available energy, meaning that choices have to be made with regard to energy efficient methods of dewatering.

What are the physical states and their corresponding aspects to consider when handling polymetallic nodules?

- The research on the material properties on polymetallic nodules is mainly focused on fully intact nodules.
- From the moment the polymetallic nodules are lifted from the seabed, the degradation process starts; On the bulk parameters of degraded polymetallic nodules, there are only few publications available in the public domain.

It is crucial to better understand the characteristics of degraded polymetallic nodules in the context of bulk handling. Optimization of the dewatering and transport installations can be achieved. The next chapter will elaborate on this subject.

3 - Nodule properties

This chapter further elaborates on the particle properties given in chapter 2.3.

3.1 Polymetallic nodules sample

Royal IHC provided a container with around 50 kg of polymetallic nodules from the GSR licence area. These nodules have been used in earlier research, focused on the degradation of nodules in transport from the seabed to the sea surface. Resulting in broken and damaged nodules. Therefore these are a good representation of nodules coming from the VTS.

The degraded nodules provide an unique opportunity to gain an understanding of the bulk behavior of the nodules once they have arrived on the ship.

When taking into account the test data from De Hoog and Van Wijk, it can be stated that nodules will become tougher when they are reduced in size [5, 35]. Therefore, the nodules likely degrade to a particular uniform grain size, which is how they enter the mining support vessel.

Since it is not clear what the actual particle size will be after the VTS, it is necessary to run the experiments several times with different grain sizes.

A sieving analysis is done on the provided sample of polymetallic nodules. The smallest nodules <30 mm will be separated by sieves which were available in the dredging laboratory, depicted in table 3.1. The larger nodules >30 mm are sieved by hand, a method less destructive than sieving. The particles are placed in bins and assigned a letter ranging from A, representing the largest particles (>70mm) to K, representing the smallest particles (<0.5 mm). A particle size distribution of the nodules sample is added in appendix B.1.

Table 3.1: Classification nodules.

Classification	Size of nodules [mm]	Weight [g]	Classification	Size of nodules [mm]	Weight [g]
A	70- 100	4860.4	G	4 - 10	1452
B	50 - 70	10550	H	2.8 - 4	166.9
C	30 - 50	19248.8	I	1 - 2.8	483.9
D	25 - 30	1866.6	J	0.5 - 1	526.1
E	16 - 25	8766.6	K	<0.5	655.3
F	10 - 16	4425.1			



Figure 3.1: Before and after sieving.

3.2 Density measurements

Particle properties with a relation to the density are relevant to the design of the harvesting operation. From these values it can be determined what the scale of the operation should be to meet production targets. As shown in chapter 2.3, several authors have researched particle properties, however, they showed different results for the density. Therefore the density experiments are repeated and compared with the literature. The method and results of the measurements are given in the following section.

Research questions of this chapter:

- How do the densities of the IHC nodules compare to the nodules from other sites of which experiments are published in available literature?

3.3 Methods

For the in-situ/saturated density measurements, it is essential to first fully saturate the nodules. This is necessary because otherwise, when measuring the volume, water can still enter the pores of the nodules. As a result, the volume of the nodule will be underestimated. The saturation process is achieved by immersing the nodules in a container of water for a longer period of time, 48 hours is a good length of time for this process. Since it is possible that air still remains trapped underneath the nodules, it is important to turn over the nodules occasionally. After the process of saturating, the weight and volume is measured. This is done simultaneously when a measuring beaker is placed on a scale. Calibrate the scale to zero when the beaker with water is placed on the scale, and write down the water level h_0 . After this step, the nodules are placed in the beaker, and the weight and water level is documented again as h_1 . The in-situ density is determined by dividing the mass by the volume. This method is schematically represented by figure 3.2

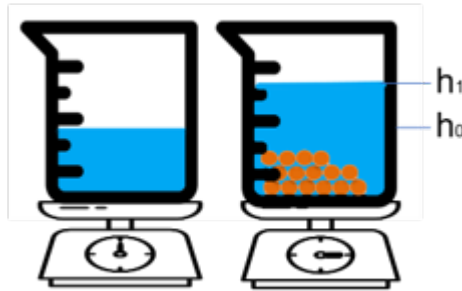


Figure 3.2: Schematic overview of volume and mass measurement of a batch of nodules.

To determine the dry density, it is important to also have a dry mass of the nodules. This is accomplished by placing the nodules in the oven for 24 hours at 105 °C. With this temperature, the moisture evaporates, and there is little chance of burning minerals. Appendix figure B.2 shows the oven settings. Weight measurements were taken during the drying process. This was unfortunately not possible during the night hours, therefore there is a data gap after 8 hours. The next day, hourly measurements were taken again. This will be discussed in more detail in the results.

Measurements

Four batches of about 1 kg with different grain sizes were prepared. Table 3.2 shows the grain sizes involved. There are 2 reasons for going for these batch measurements: Firstly, reduction of measurement error while reading the volume. The reading error will automatically become smaller when the volume difference is larger. Secondly, there is immediately an average density by measuring several particles at once. The goal was to compare these results to the literature and see if the current condition of the nodules is similar to nodules that have been out of the ocean for a shorter period of time. The decision was made to also measure individual nodules separately for extra verification and control of the measuring equipment.

The choice was made to put two extra batches in the oven just before the closing time of the building. The first 8 hours were already documented with the other batches; the additional batches were placed in the oven to record the part after 10 hours of oven time.

With the results of saturated density, dry density, and volume, a number of parameters can be calculated: Water content, porosity, void ratio, mineral density and natural water content. The formulas and explanations of these parameters can be found in theory section 2.3.

3.4 Results

The results of the density measurements are presented in table 3.2 Further processing is presented in table 3.3. The average saturated density was 1.911 g/cm^3 with a 95% confidence interval of 0.035 g/cm^3

Table 3.2: Measurements for density.

	Size [mm]	Mass saturated [g]	Mass dry [g]	Volume [ml]
Batch	70+	960.1	684.4	510
	50-70	1195.6	840.4	602
	30-50	1179.3	817	620
	10-30	1097.6	775	600
	4-10	163.3	109.1	85
Single nodules	50-70	94.5	67.2	49
	50-70	98	68.5	52
	30-50	58.7	40.8	30
	30-50	34.4	25	18

Table 3.3: Particle properties.

	Size [mm]	Watercontent ω [%]	Saturated density ρ_{situ} [g/ml]	Dry density ρ_d [g/ml]	Porosity η [-]	Void ratio e [-]	Mineral density ρ_s [g/ml]	Natural water content ω_n [%]
Batch	70+	40.3	1.88	1.34	0.54	1.18	2.92	28.7%
	50-70	42.3	1.99	1.40	0.59	1.44	3.41	29.7%
	30-50	44.3	1.90	1.32	0.58	1.41	3.17	30.7%
	10-30	41.6	1.83	1.29	0.54	1.16	2.79	29.4%
	4-10	49.7	1.92	1.28	0.64	1.76	3.54	33.2%
Single nodules	50-70	40.6	1.93	1.37	0.56	1.26	3.10	28.9%
	50-70	43.07	1.89	1.32	0.57	1.31	3.04	30.1%
	30 -50	43.9	1.96	1.36	0.60	1.48	3.37	30.5%
	30 -50	37.6	1.91	1.39	0.52	1.09	2.91	27.3%

Figure 3.3 shows the water removal starting with 1 hour interval measured during working hours. For clarity, the data points of each batch are linked. During the night there was no possibility to measure, this explains the gap in the measurements. The graph shows that the most water evaporates in the first 8 hours, after that it approaches zero. It can also be seen that batches with larger nodules lose their moisture more slowly than smaller nodules.

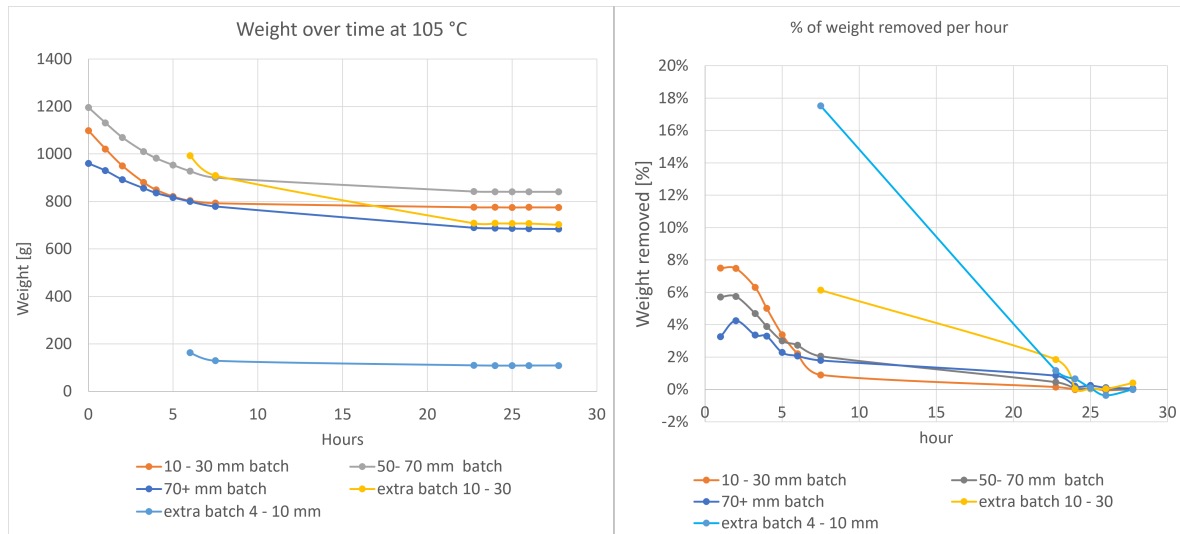


Figure 3.3: Moisture dissipation during the time in the oven.

Comparison with literature

Figure 3.4 shows density measurements from the last decades. In the research of Mero [21] and Gasby [50] only the mineral density is shown. The mineral density shows significant differences up to 30%.

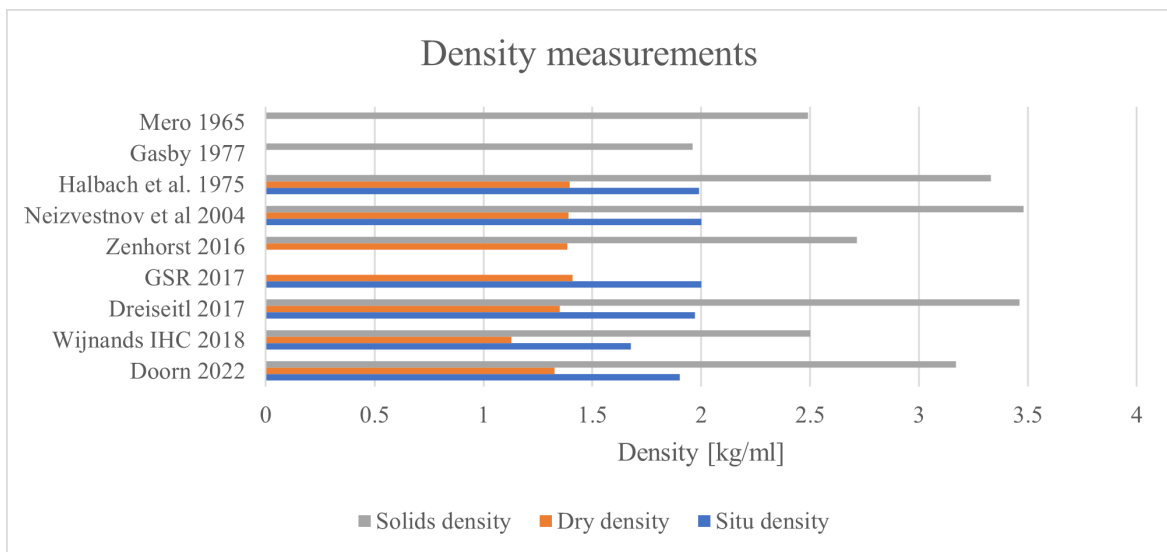


Figure 3.4: Density measurements from the literature.

3.5 Discussion

There has been a significant difference between the studies on the properties of nodules in the last few decades. Two possible explanations for this difference: Firstly, the origin of the nodules. The area of the CCZ here they were grown is 5000 km^2 ; this may cause

density differences. However, it is strange if large differences occur when the nodules come from neighbouring areas. This difference is well seen with Wijnands [53] and Zenhorst [51] compared to Neizvestnov [49] and Dreiseitl [18]. All the nodules come from areas near area H22 of Figure 2.16.

Secondly, the time of measurement. The densities of the nodules of Dreiseitl and GSR were measured after they had just been lifted from the seabed. These measurements are influenced by mineralization and pore seawater density [18]. The lab density measurements did not take this into account and this could have led to a discrepancy in the results.

The measurements of Zenhorst en Wijnands were conducted in a lab environment after being out of the ocean for a longer period of time.

It is also noteworthy that the thesis author gets different density values than Wijnands [53], who uses the same nodules. It is very likely that the difference came about when measuring the volume. It is very important to remove the free water from the nodules; otherwise, the volume will be overestimated. However, the opposite is also true. When the nodules are out of the water for too long, the density will be lower because pore water has been lost. To eliminate this saturation problem, using a tomography scanning method would provide a better solution.

3.6 Conclusion and recommendation

To reflect back on the research question of this chapter: *How do the densities of the IHC nodules compare to the nodules from other sites of which experiments are published in available literature?*

The measurements conducted on the nodules from IHC provided a saturated density of 1.911 g/cm^3 with a 95% confidence interval of 0.035 g/cm^3 . This density value is very similar to those examined in neighbouring areas, within 5% difference to the nodules measured in the research of Dreiseitl[18], GSR[64] and Neizvestnov[49]. There is a larger difference with other studies, up to 30%. This is possibly caused by measuring errors, different nodule harvest locations and the moment of measuring: immediately after the nodules were lifted from the seabed or after a longer period in a lab environment.

Recommendation

It is important to use another method to determine the volume to rule out measurement errors completely; a tomography scan would provide a solution.

4 - Measuring particle shape

For the design of bulk handling equipment, computational modelling with discrete element method (DEM) is frequently used. The particles are usually modelled as spheres to decrease computational power. In recent years, 3D scanning of objects has increased in popularity for DEM applications. This chapter aims to determine a method of scanning polymetallic nodules for future use in DEM software and find out more about the shape characteristics of polymetallic nodules. In this section the following research question will be answered:

Research questions of this chapter:

- Is photogrammetry with Qlone an effective method for scanning polymetallic nodules?

4.1 Methodology

Determining the characteristic particle shape is done by scanning the organic shapes. There are different possible scanning methods, each with its benefits and drawbacks, as is described in this section. 2D profiling using industrial and commercial cameras combined with shape extraction scripting techniques can be employed to model digital 2D particle shapes. It is a method that can handle small particles and does not require expensive hardware. However, this approach is limited to two-dimensional DEM applications, as profiles extracted from a single 2D picture do not provide enough information for the creation of 3D particles.

When it comes to 3D shape recreation, scanning using a portable laser scanner was used by Paixão et al.[65] to model railway ballast rock particles. Such setup uses three high definition cameras and eight LEDs around the cameras. The particle shapes and sizes are obtained with the aid of retro-reflective targets placed on the object and/or the surrounding area. Coetzee [66] employs a rotary laser scanner that uses a stationary camera setup and particles placed on a rotating platform to capture the object from all sides. Feng et al.[67] incorporates Computed Tomography (CT) scanner results to extract particle shapes while a box with particles rotated around its axis. Then Spherical Harmonic Function (SHF) is employed to reconstruct multiple particle shapes simultaneously.

Unfortunately, all the aforementioned scanning methods have at least one serious drawback, which makes particle creation complicated: they either require expensive hardware, cannot handle small particles, are inaccurate, or cannot capture three-dimensional shapes. For this purpose, an alternative approach is used that is yet to see a widespread application in DEM methodology - specifically scanning is performed using a photogrammetry technique, which will be discussed in more detail in the upcoming section.

Photogrammetry

Instead of relying on conventional particle scanning methods, scanning using photogrammetry has been chosen for modelling nodules and nodule fragments. Photogrammetry is the science of making measurements from photographs. Application include: Areas which include the creation of large maps from multiple pictures, terrain scanning and three-dimensional object recreation.

So far, photogrammetry has not been very widely applied for DEM particle modelling, but it is expected to gain popularity in the future with more advancement in the field. First

applications have already been observed in the literature; specifically, it has been applied by Paixão et al.[65] to reconstruct railway ballast particles and to evaluate mesh deviations from scanning results acquired using a conventional laser scanning technique.

As a scanning method for particles, photogrammetry has three benefits over different scanning methods:

- Accuracy: Photogrammetry can provide results at a level of accuracy that is similar to what can be achieved with special 3D scanning hardware[65].
- Object size: It is capable of scanning small objects up to five millimeters.
- Accessibility: Photogrammetry uses conventional camera hardware for scanning. An average quality phone camera setup is enough for modelling 3D objects. This hardware is readily available to most people already, which means that in most cases, no special and/or expensive hardware is needed to perform the scanning.

Just as any modelling and scanning approach, photogrammetry also has its drawbacks. Specifically, it is a prolonged and fairly labour-intensive process. Considering both the strengths and weaknesses of photogrammetry, it comes out as an excellent option for modelling 3D representations for scanning the nodules and the nodule fragments.

4.2 Method

This thesis focuses on two different photogrammetry methods to scan the nodules. The first method uses computer based image processing software called 3DF Zephyr. First, the photogrammetry setup of S. Pargalgauskas[68] was used. A nodule is placed in a high contrast environment and pictures are taken from up to 500 angles. Afterwards, the photos are uploaded to the computer to create a 3D scan via 3DF Zephyr's software package.

However, this method has two downsides:

- The processing steps to scan one particle take anywhere from 240 min for a beginner to 75 min for a skilled operator[68]
- It is difficult to scan the bottom of an object. Nodules have to be placed on a flat surface from where no picture can be taken.

As a result, a different method was chosen: A phone application called Qlone. Qlone is a so-called rapid modeling application. This app reduces the processing time from hours to minutes. Furthermore, this application has the option to rotate an object so that the bottom can also be modeled properly, unlike with 3DF Zephyr

The downside of Qlone is the quality of the scan. However, it is unclear how much this matters for the main purpose: Retrieving parameters like shape factor, sphericity and angularity, because the processing time of Qlone is significantly shorter

Setup for Qlone

- Phone with camera
- Computer for processing 3D scan

- Turning table.
- Led panel for lighting.
- Printed mat with size indication for larger and smaller particles.

Additional:

- Movable phone holder

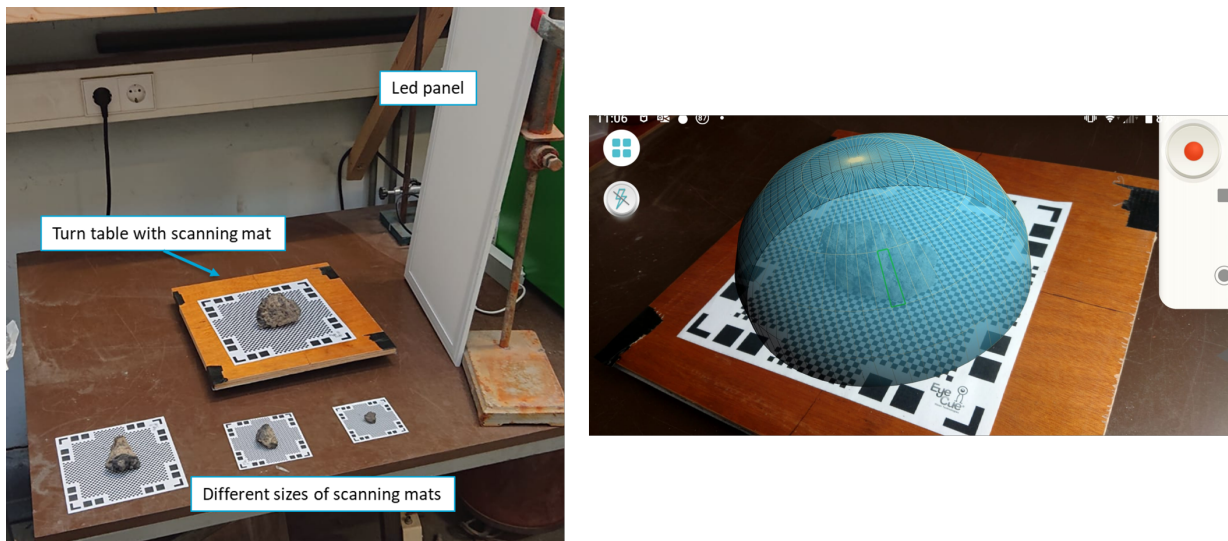


Figure 4.1: The left image shows the setup, and the right image shows the scanning process.

Scanning procedure

- Open the Qlone application and activate the led panel.
- Follow the instructions on the application
- After scanning the nodule, turn the nodule upside down
- Rescan the nodule.
- Export scan to STL format
- Reduce the STL file according to the size of the scan mat used.

4.3 Results

Visual inspection shows no differences between the actual nodule and the scanned illustrated STL file in figure 4.2. Further validation of the scan's accuracy was accomplished by making a 3D print of the scanned nodule and comparing this with the actual nodule.

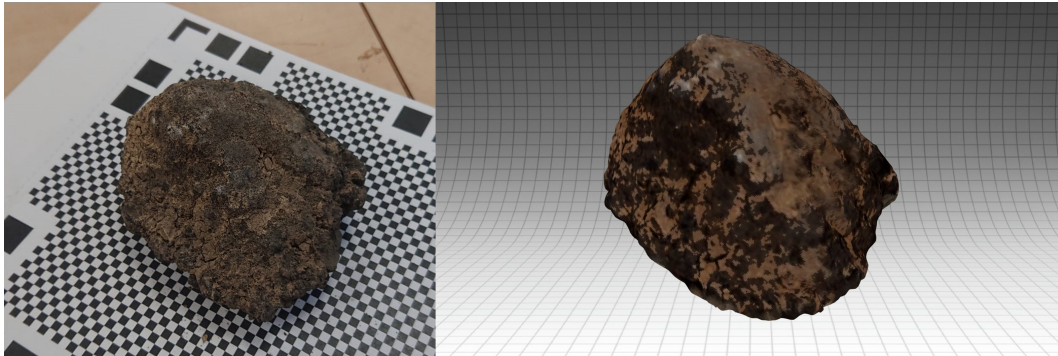


Figure 4.2: Qlone digital scan.

Validation

An Ultimater 2+ was used to 3D print 2 scans. The biggest available nodule and the smallest. The biggest to validate complex angles and the smallest to validate printing accuracy. The 3D scan resulted in a STL file and was converted to g-code with slicer software: Cura. This slicer software prints the nodules at full scale. When these nodules are printed, they are compared to the real ones. Caliper measurements show a maximum deviation of 3.4% on the small nodule and 2.5 % on the large nodule. Figure 4.3 shows the 3D printed nodules to the original nodules. Table 4.1 shows the measurements.

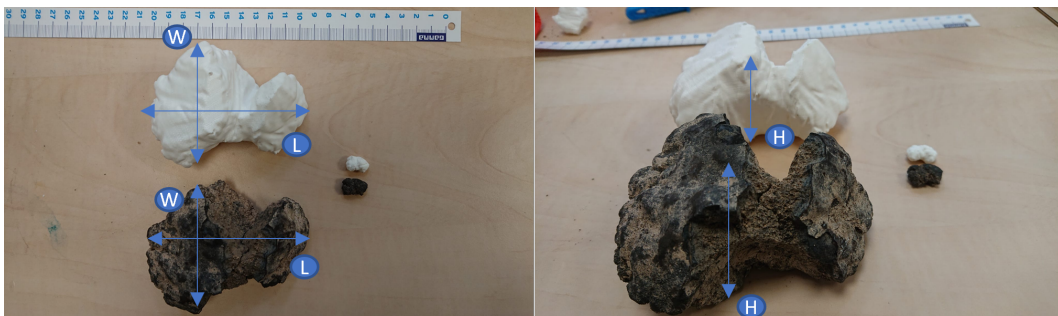


Figure 4.3: Comparison Qlone 3D printed scan and nodules with dimensions.

Table 4.1: Validation Qlone.

	Dimension	Real [mm]	3D print [mm]	Difference [%]
Large nodule	L	99.5	102	2.5
	W	73	72.5	0.7
	H	53	53.5	0.9
Small nodule	L	16.1	15.83	1.7
	W	10.24	9.91	3.2
	H	8.8	8.5	3.4

4.4 Discussion

A trade-off between accuracy and scanning speed is inevitable when scanning granular material. With a program like 3DF Zephyr, it is possible to scan nodules with high accuracy. However, scanning and processing in 3DF Zephyr is time consuming. A quick scan application such as Qlone has an accuracy within 1 cm with scans that can be made within 5 minutes.

4.5 Conclusion and recommendations

To reflect back on the research question: *Is photogrammetry with Qlone an effective method for scanning polymetallic nodules?*

A rapid modeling application like Qlone Has proven a scanning speed of 5 minutes for a single nodule and an accuracy of less than 5 mm in all directions. Concluding that the quality of Qlone is sufficient to recreate shapes of nodules and nodule fragments in a digital environment.

Software like Qlone seems suitable to determine the sphericity, angularity and roundness of polymetallic nodules. Opening the opportunity for improved modelling in which a large number of scans of actual nodules serves as input for a design of bulk handling equipment model. The remainder of this thesis, however, focuses on further experimental measurements with degraded nodules provided by IHC, for there is no current literature on the following experiments executed with nodules as such.

5 - Measuring the angle of repose

The angle of repose represents the shear stress of bulk material under the force of gravity as stated in chapter 2.3.2. According to Mohajeri[57], the angle of repose results are helpful to categorize flow properties. It is used commonly to design silos and hoppers. In an application-oriented study of Salehi[69], silo discharge of wood chips material is improved by using angle of repose tests.

Research questions of this chapter:

- What is the angle of repose of degraded polymetallic nodules and how is it influenced by moisture content?

5.1 Introduction

In this research, the angle of repose is measured following the ledge test procedure, also found in literature as the “shear box” [70] and “rectangular container test” [71]. During a ledge test, a container with a movable door is filled with bulk solids. After opening the movable door, the bulk solid flows out of the container. Once the flow halts and the bulk reaches a state of static equilibrium, the angle of repose is measured between the horizontal plane and the free surface angle. Figure 5.1 shows a schematic overview of the ledge test method. Ledge tests are mainly used for particle calibration in DEM software. The Angle of repose provides an insight in the particle-particle interaction according to Lommen[72].

Mohajeri [57] used the ledge test for iron ore samples and he observed higher values for samples with moisture than for dryer samples. However, the particle size in his research is considerably smaller than with the polymetallic nodules.

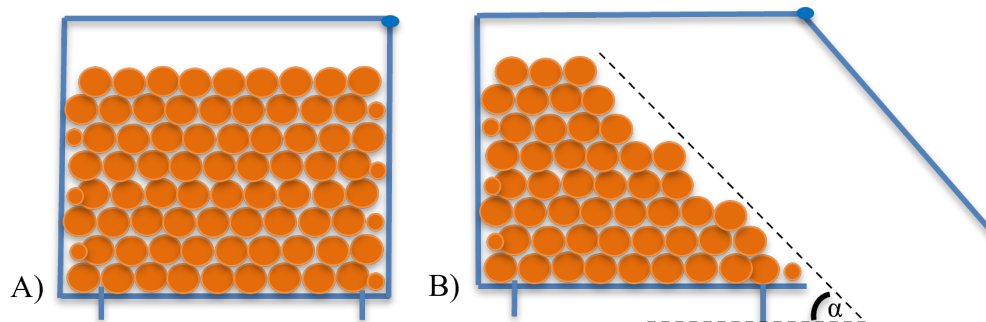


Figure 5.1: Schematic overview of angle of repose. α represents the angle of repose.

5.2 Methods

First, it was determined which nodules were suitable for this test setup. Literature describes that the particles used should fit at least ten times the width of the apparatus [57]. Because the test apparatus is 200mm x 200mm x 250mm, the maximum desired particle size for this test was less than 20 mm per particle. Due to this criterion, it was decided to perform this test with particles of category F (10-16 mm), of which there were enough particles to fill the volume of the tester.

Measurements

This section explains how the angle of repose test is conducted.

- The test setup is placed on the table and a GoPro Hero 4 camera is put in front of the apparatus. A bin was placed next to the ledge test apparatus to catch outflow of nodules. A levelling tool was used to ensure that the apparatus is levelled.
- A batch that fills the test device was determined. The mass of this sample is 4915 grams. The particles were placed in heat resistant bins and were put in the oven to remove the remaining water content.
- After drying the nodules, the measurement started: It was repeated nine times with dry nodules. A photo was taken each time the nodules were placed in the apparatus and after the test was completed.
- A Matlab script is used to get the angle of repose from the picture. The script creates two lines, one of which must be placed on the slope and the second line may be placed horizontally at the base. The angle of repose is determined between these two lines. The script can be found in appendix B.3
- After the measurement, the nodules were placed in a bucket with water to re-saturate for 48 hours.
- Nine saturated tests were conducted with the same procedure.

Because nodules degrade, potentially resulting in a 'rounding effect', the experiment is subsequently done in reverse order. Another nine tests were conducted with saturated nodules, whereafter they were completely dried for 24 hours. The last nine tests were conducted with these dry nodules. The measurement is repeated for dry and saturated nodules totalling 36 ledge tests.



Figure 5.2: Two views of the angle of repose setup.

Camera calibration

The angle of the Gopro used in the angle of repose test shows a distorted image from reality. Figure 5.3 shows the natural curvature of a GoPro HERO4. At the center of the lens, distortion is lowest. Thus it is important that the angle of repose is measured mainly in the center of the image.

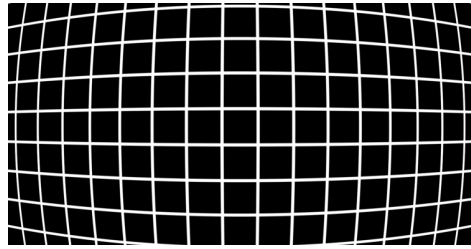


Figure 5.3: Gopro camera distortions [13].

5.3 Results

The mean value for the angle of repose for nodules of size 10-16 mm was $49.5 \pm 1.46^\circ$ for the saturated batch and $49.6 \pm 1.1^\circ$ for the dry batch with a confidence level of 95%. The distribution of the results is represented in a box and whisker plot in figure 5.4. The raw data is presented in appendix B.3.

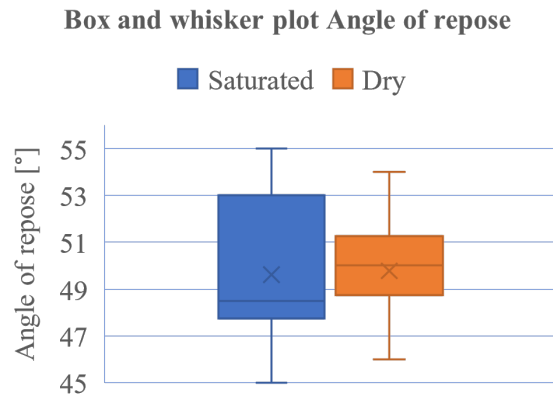


Figure 5.4: Results of 18 angle of repose test with dry nodules and 18 tests of saturated nodules.

5.4 Discussion

The results in section 5.3 show that the mean values of the angle of repose of dry and saturated nodules are within each others error margin. The difference is statistically insignificant. The only changed variable, moisture content, has no significant influence on the angle of repose of polymetallic nodules.

Concluding that the shape of the particles is governing in the angle of repose and not the adhesive effects of the moisture content of the particles. As described in section 2.3.2, Dreiseitl[18] has done angle of repose tests with intact nodules, resulting in an angle of repose

30°. It seems that the angle of repose becomes smaller as the particle size increases from comparing Dreiseitl with the measurement. However, it is recommended to confirm this with additional tests on more various nodule sizes.

5.5 Conclusion and recommendations

This chapter treats the question: *What is the angle of repose of degraded polymetallic nodules and how is it influenced by moisture content?*

- The angle of repose for polymetallic nodules of the size range 10 - 16 mm nodules is $49.5 \pm 1.46^\circ$. The results were obtained by using the ledge tester.
- The data shows that the difference between saturated and dry material is insignificant.

Recommendations

- Depending on the chosen VTS, the nodule sizes will be different, ranging from 20 mm with hydraulic transport to possibly bigger nodule sizes with air lift. Additional tests should be conducted on many larger and smaller batches of particle sizes for a complete picture.
- According to Hashemi [73], there are 9 different methods to determine the angle of repose, with different results for every type of test. Be aware that these angles of repose are not one to one comparable with the angle of repose resulting from the ledge tester.
- Although the ledge test has proven sufficient to compare the angle of repose of saturated and dry nodules, the design and simulations of the transport and storage operation could benefit from an additional draw down angle of repose test. In this type of test, a batch of nodules is placed on a hatch. Subsequently, the hatch is opened and the accumulation of the nodules on a surface is followed over time resulting in an angle of repose. One advantage of the draw-down test is information obtained on the time it takes to develop a steady angle of repose. Two disadvantages are: More degradation of the samples, and a larger required nodule quantity in comparison with the ledge test.

6 - Measuring the sliding/rolling friction angle

This chapter provides an overview of the sliding and rolling coefficient of friction of degrade polymetallic nodules on a steel and rubber surface. The coefficient of friction is derived from the friction angle, which will be elaborated more in the introduction. The following research questions will be answered.

Research questions of this chapter:

- What is the sliding/rolling friction angle of nodules placed on a steel slide and on a rubber conveyor system when considering different compaction states?
 - What is the effect of the particle size on the rolling/sliding friction angles?
 - What is the effect of moisture content on rolling/sliding friction angles?
 - What is the effect of adhesion forces of clay on rolling/sliding friction angles?
- How does normal force influence the rolling/sliding friction angle?
- What effect does the sliding nodules have on the sliding surface roughness?

6.1 Introduction

When the polymetallic nodules leave the water, they undergo dewatering steps and will be exposed to horizontal and vertical transport to reach the storage hold. These height differences will likely be bridged using chutes and conveyor belts. The angles of these conveyors must be placed in such a way that no congestion occurs in the system. Furthermore, optimization of the transport system is also essential because this operation takes place at sea, where space is at a premium. However, no literature is found of the friction angles of polymetallic nodules. This is a research gap that will be addressed in this chapter.

Coefficient of friction

The first recorded studies on friction are dated in fifteenth century and belong to Leonardo da Vinci (1452-1519). Two hundred years later, his observations became two of the well-known laws of sliding friction introduced by Guillaume Amontons (1663-1705), namely:

- Friction force is directly proportional to the applied load.
- Friction force is independent of the apparent area of contact.

Leonardo da Vinci introduced also the concept of coefficient of friction (μ) as the ratio of the friction force F_f to normal load N :

$$\mu = \frac{F_f}{N} \quad (6.1)$$

The easiest set-up to understand static friction consists in a body placed on an inclined plane as depicted in figure 6.1.

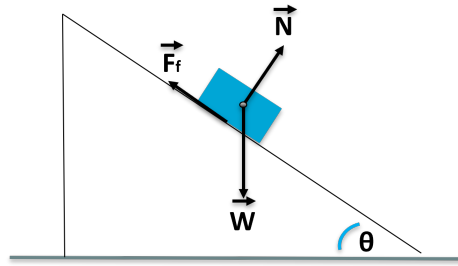


Figure 6.1: Forces acting on a body on an inclined plane.

The force which maintains the body in rest on the tilted plane is the static friction force. The force needed to initiate gross sliding is the maximum static friction force F_s . The dynamic friction force F_d is the force required to sustain motion. The coefficient of friction can be also defined as the tangent of the angle of the inclined plane. The body will remain in rest for an angle less than a certain value θ and it will start sliding down if the inclination angle exceeds θ . Writing the load balance equations for the body from figure 6.1, the coefficient of static friction is given by equation 6.2:

$$\mu_s = \frac{F_s}{N} = \frac{W * \sin \theta}{W * \cos \theta} = \tan \theta \quad (6.2)$$

The coefficient of static friction is typically larger than the dynamic one, but it can be also equal to the coefficient of dynamic friction [14]. The graph of figure 6.2 depicts the static friction regime with the dynamic regime. When the angle corresponding to the peak of this graph is known, it can be taken into account in the design of a transport system.

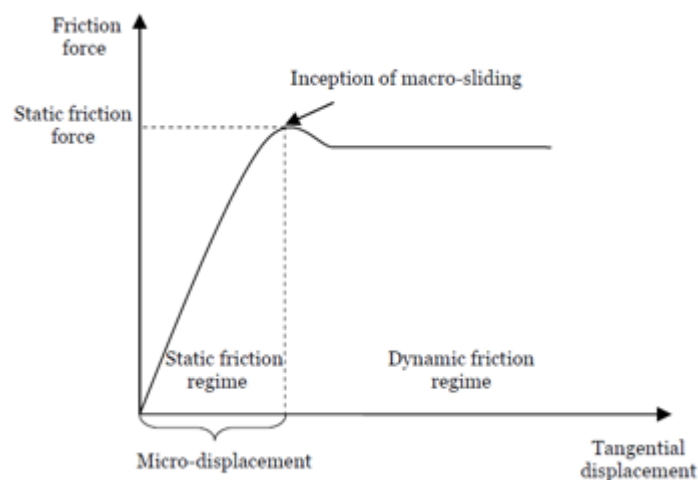


Figure 6.2: Static friction and dynamic friction[14].

Relevance

If a conveyor belt is placed under an angle, the angle has to be smaller than the maximum static friction angle to prevent the load from sliding/rolling in the wrong direction. When the

product is transported downwards, the angle must be greater than the static friction angle to prevent blockages.

Because there is no information on the coefficient of friction of polymetallic nodules, it was decided to perform sliding experiments.

6.2 Methods

Design of Experiment

An inclining surface can be used to measure the coefficient of static friction. A literature survey reports that the coefficients of static friction of polymetallic nodules were not yet determined. Based on the two assumptions in bulk solids handling: namely, particles can be in a very loose state, and particles are in a highly compacted state [74], the coefficients of static friction are measured for the contact between discrete particles and a steel surface, and for the contact between bonded particles and a steel surface.

Inclined surface tester

The device used to measure the static friction of particles is depicted in figure 6.3. This tester employs a motor to enable the inclination of the bottom surface with respect to an axis. The angle between the inclining surface and horizontal surface is denoted as inclination angle, and can be automatically measured with the accuracy of $\pm 0.05^\circ$.

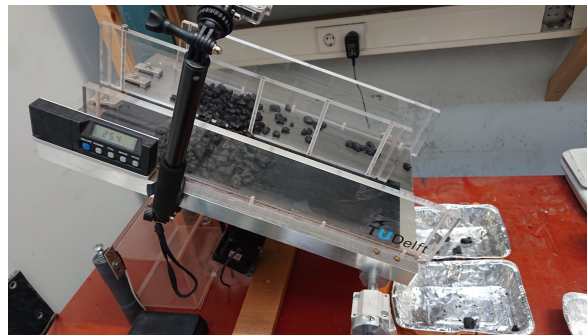


Figure 6.3: Inclined surface tester in operation.

Figure 6.4 shows the inclined surface tester setup when using saturated particles: 1) Gopro hero 4 with to capture the moment of sliding and the corresponding angle. 2) Device that measures the angle of the surface tester. 3) Control panel of inclined surface tester, consisting of a switch for turning the device on and off, a switch for the direction of the surface tester and a rotating speed adjuster. 4) Sliding surface. 5) Nodule catch tray. 6) Removal of free water around nodules. 7) Re-saturation tray.

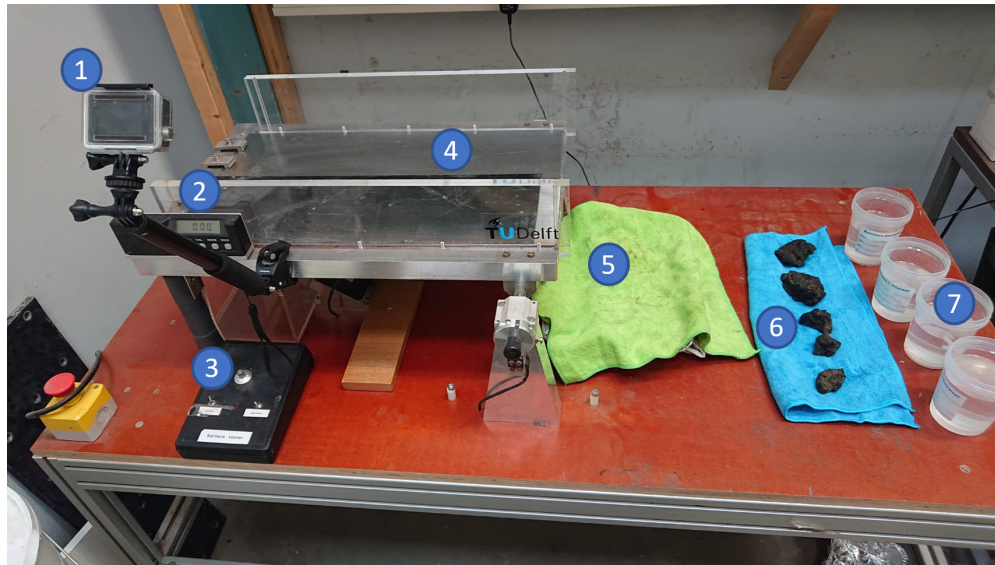


Figure 6.4: Inclined surface tester for a saturated test.

Procedure

As mentioned in the previous section, bulk material can be in a loose state and in a highly compact state. In order to assess this for polymetallic nodules, the decision was made to test this in five different nodule configurations and on a steel (S235) surface and rubber(Ethylene Propylene Diene Monomer) surface.

Figure 6.5 shows the different configurations:

1. The single nodule test, to see when a single nodule starts to roll or slide.
2. Bulk-free, where nodules are placed against each other on the plate and it is examined when the first particles start to move, when the majority of the particles moves and when the last particles move.
3. Confined nodules, a group of nodules is enclosed and they can only move simultaneously. This gives a more compact particle configuration.
4. Added mass rolling configuration, a weight is added to a sledge and placed on top of a load of the nodules. This increased normal force should indicate a compacted state.
5. Added mass sliding configuration is the same as added mass rolling, only here the nodules are confined in a mould, therefore they cannot roll and sliding is the only possibility.

The tests are conducted with dry nodules, saturated nodules, and nodules which are rolled in CCZ sediment, appendix B.4 elaborates on the CCZ sediment. The surface roughness of the rubber and the steel was measured after testing the single nodules and the confined bulk nodules. The following section will elaborate more on the different setups.

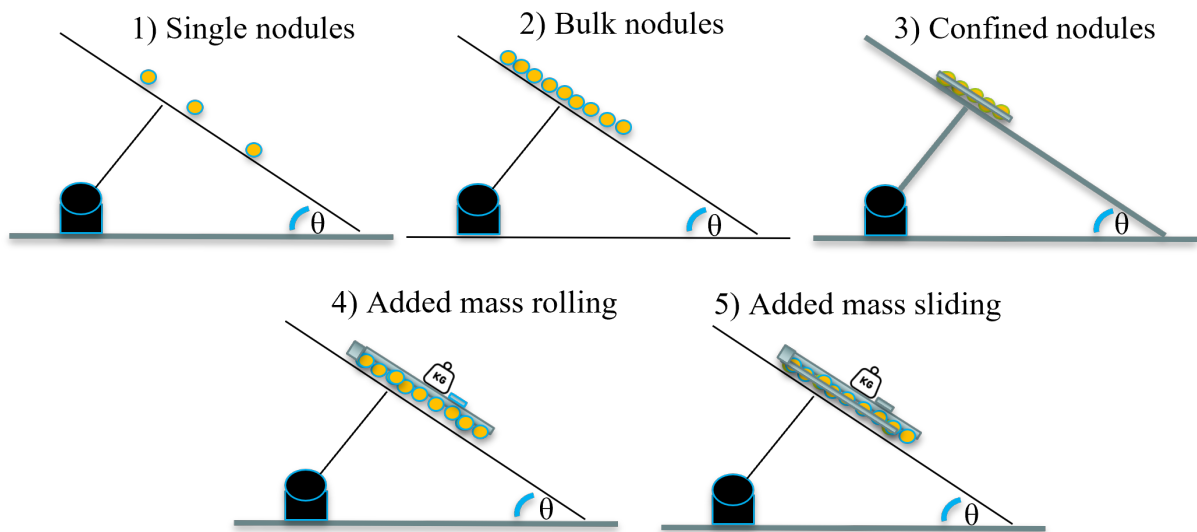


Figure 6.5: Overview of the inclined surface tester experiments. The surfaces which were used for the tests were steel and rubber. Furthermore, the tests were conducted with dry, saturated and CCZ clay-rolled nodules

Single nodule test

The single nodule test was initially carried out with two different nodule sizes, namely the C(30-50mm) and B(50-70mm) groups. This test yielded 18 data points for the dry tests. The test was then repeated with saturated nodules and with nodules that had been placed deep-sea sediment(CCZ clay). Furthermore, this test was carried out simultaneously for steel and rubber. After these initial tests, it was decided to repeat this test for a smaller particle size, namely E(16-25mm). This yielded additional data points for the dry tests. The mode of movement, rolling or sliding, was noted in correspondence with the angle for all tests.

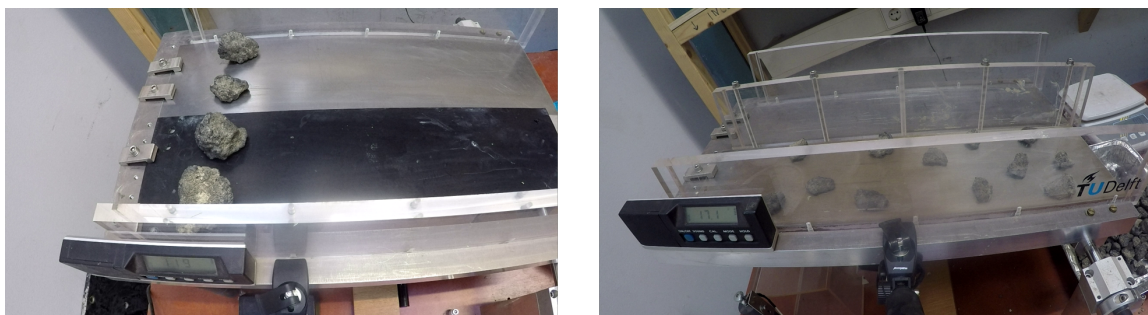


Figure 6.6: Single nodule test setting, left side shows the 50 - 70 mm class, the right side shows the 16-25 mm class.

Bulk-free nodules

The free bulk tests were formed following the example of Chen[75]. Eight batches of nodules were created with four different particle sizes: B,C,E and F. Half of these nodules were put underwater for 48 hours to ensure complete saturation. The other half was placed in the oven to ensure that they were completely dry. Subsequently, eight tests were conducted with

each batch being tested twice on rubber and twice on steel. This gave a total of eight test results for dry and saturated. After the previously mentioned tests had been carried out, the saturated nodules were placed in a container with CCZ sediment and tests were carried out again. This also produced eight results for rubber and steel. For each test, the initial angle, bulk angle and final angle were written down. Figure 6.6 shows two test setups, the left setup shows the B group of nodules and the right side shows the E group. Figure 6.8 shows the batches of particles.

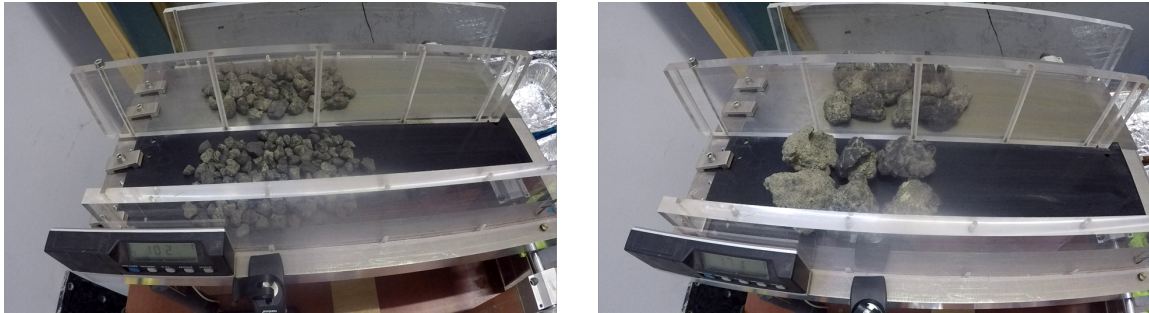


Figure 6.7: Bulk-free example, left shows the E (16-25 mm) batch and the right side shows the B(50-70 mm) class.

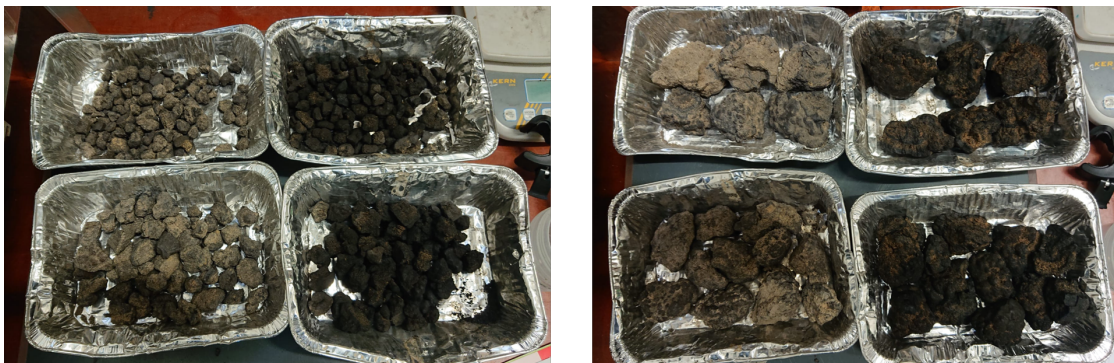


Figure 6.8: The batches of nodules used in the bulk-free tests are shown here. Top left shows the F(10-16 mm)batch, E(16-25 mm) batch on the bottom left side. B(50-70 mm) batch on the top right and the C(30-50 mm) batch on the bottom left. Particle sizes had a dry and a saturated batch.

Confined nodules

The confined bulk tests were conducted in the same way as the free bulk tests. The only difference in the confinement of the batch of nodules, a paper ring was placed around the nodules, so individual particles cannot roll/slide away. The paper ring had a coating that makes it water-resistant. This allows all tests to be carried out without the ring influencing the result. Figure 6.9 shows the setup.

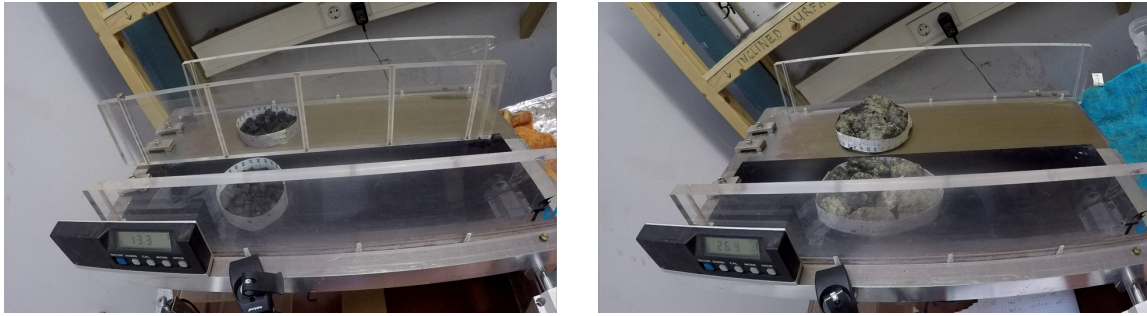


Figure 6.9: Bulk confined example.

Added mass rolling

The added mass test idea originates from a study by Blue nodules [7]. In which the expected production values were used to determine the weight of the nodules on a conveyor belt system. Analysis showed that the conveyor system needed to withstand 434 kg/m^2 of nodules. It is interesting to simulate this on the inclined surface tester. The question that arose was: How do the nodules behave at a higher normal force?

An extra weight is used to simulate this normal force on the sliding surface, figure 6.10 shows a schematic of the test setup in comparison to reality. To accommodate the extra weight, a sledge was 3D printed out of PLA. The sledge and weight can be viewed in figure 6.11. The printed parts can be found in appendix B.11. The weight of the plate was 3 kg , this weight matched the dimensions of the surface tester and results in a represents a mass of around 330 kg/m^2

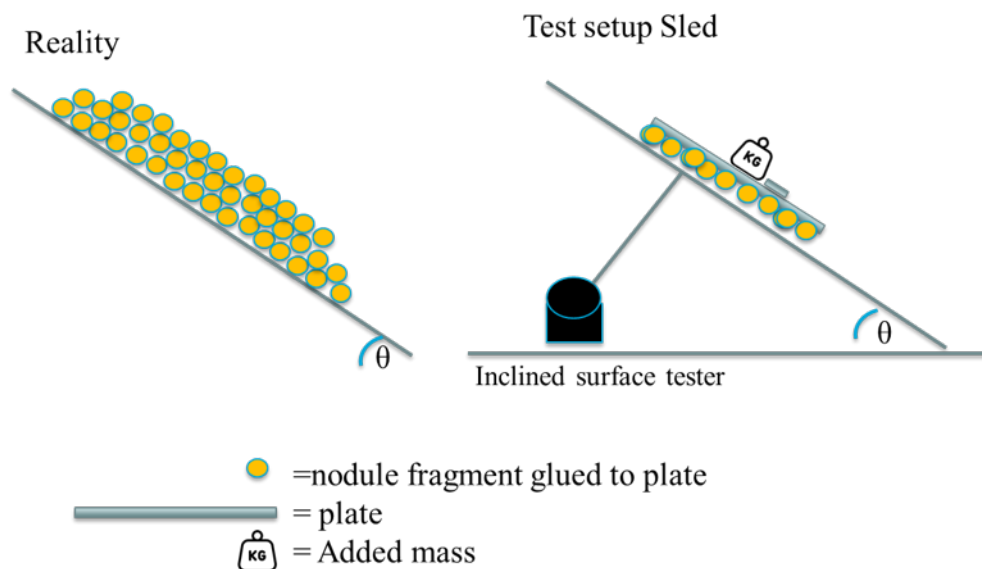


Figure 6.10: Added mass test schematic.

This test focuses on the rolling behavior of the nodules. The nodules were placed on the tester in the same way as with the bulk-free tests, after the placing of the nodules, the sledge

is placed on top. The experiment was repeated at least 4 times with dry, saturated and extra CCZ clay nodules, on rubber and steel.

Added mass sliding

A method of clamping the nodules was used to record pure sliding behaviour. Plaster and glue were used for this; appendix B.4.5 shows the creation process of these nodule plates. Furthermore, these tests were conducted the same way as the added mass rolling tests.



Figure 6.11: 3D printed sled for the added weight test and the gips/glued blocks of nodules.

6.3 Results and discussion

The results and the interpretation of the results of the sliding and rolling tests are presented in this section.

Single nodule tests

Figure 6.12 displays the results of the single nodule tests: The left side of the image shows the test results on rubber, and the right side shows the results of the tests on a steel plate. Table 6.1 shows the amount of tests, the mean and the 95% confidence level. Histograms of these tests can be found in Appendix B.6.

- **The tests on Rubber:** It was observed that the primary mode of movement was rolling. This resulted in a large dispersion of the sliding/rolling angle. It was challenging to show evident differences, the data between dry, saturated and extra clay has much overlap. However, it can be observed that the average result of the clay tests was higher than in the other two groups. This suggests that the adhesive forces of clay influence the individual nodules.
- **The tests on Steel:** The primary mode of movement was sliding. Furthermore, the same can be said as for rubber: The adhesive forces of the clay result in a larger friction angle. The steel plate started to show signs of corrosion after the first saturated nodule tests. Even with cleaning, this could not be prevented. A surface roughness meter was used to measure the level of degradation; more information will be presented in

the next section. The roughness tests showed that after the initial degradation, no further degradation occurred. It could be possible that the sliding tests themselves had a smoothing effect. For the sake of completeness, it was decided to repeat a number of experiments. The results for dry nodules deviated significantly from the original tests, which is why they were divided into rough and smooth.

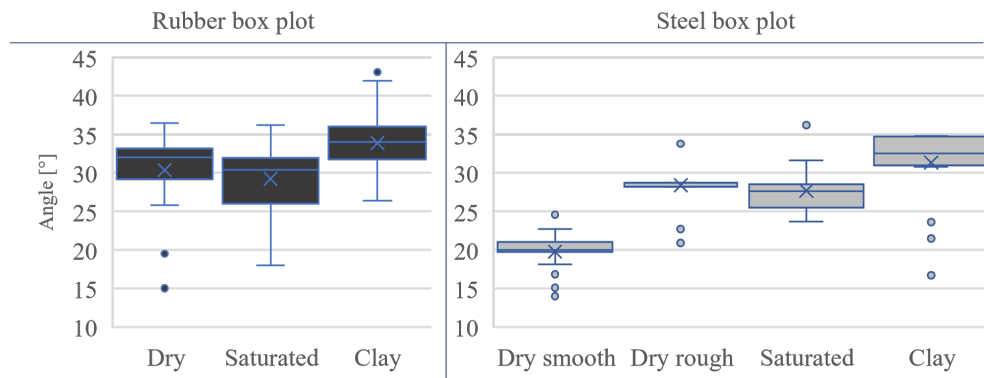


Figure 6.12: Single nodule box and whisker plot: Rubber on the left side and steel on the right side.

Table 6.1: Single nodule test.

Rubber		Dry	Saturated	Clay
Count [-]		18	16	46
Mean [°]		30.4	29.2	33.9
Confidence Level(95.0%) [°]		2.7	2.7	1.2
Steel	Dry smooth	Dry rough	Saturated	Clay
Count [-]	39	23	16	21
Mean [°]	19.8	28.4	27.7	31.3
Confidence Level(95.0%) [°]	0.8	1.5	1.7	2.2

Surface roughness

Corrosion on the steel plate was soon visible after the first saturated tests. This corrosion affected the roughness, and it was decided to keep half of the plate as smooth as possible by using sandpaper. This created different roughness levels on the plate. By comparing the roughness, it was then possible to see how much effect rust formation would have on the plate.

Subsequently, the surface roughness was measured over the steel and rubber plates. Three roughness values could be distinguished: Smooth steel, rough steel and rubber. With an average roughness of 0.46, 1.16 and 1.35 μm respectively. Appendix B.4.4 explains how these values were established

It is interesting to compare these three values with the tests which were already conducted on them. Figure 6.13 has plotted these values of the dry single nodule test against the roughness, and an apparent regression was found. The mode of motion limits this regression; most particles on rubber rolled down the tester. Therefore, it is plausible that increasing the surface roughness would not lead to a higher Friction angle after a specific roughness value. More research needs to be conducted to find this roughness value.

Another limiting factor to this regression plot is the use of rubber. Rubber has a much lower young's modulus and thus deforms when an increased normal force is applied. However, this deformation is minimal at low normal force, as in the single nodule test. Appendix B.10 shows the roughness measurements.

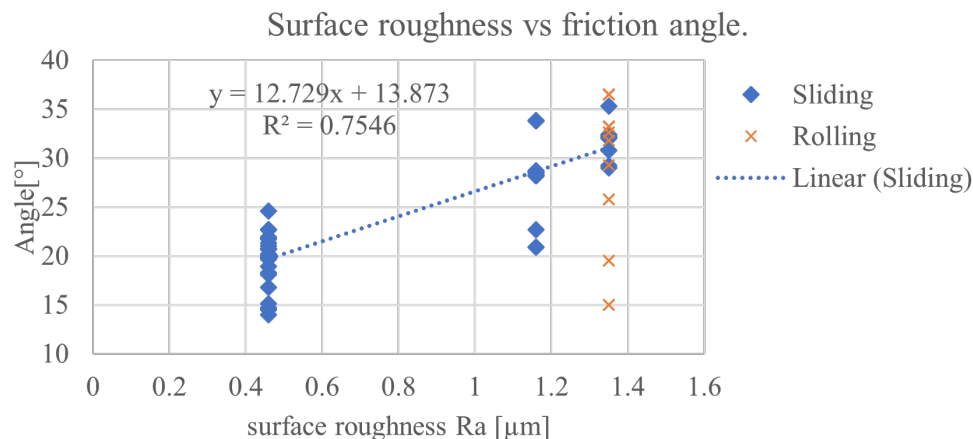


Figure 6.13: Surface roughness of 3 different surface roughness values and the corresponding friction angle: steel smooth (0.46 μm), steel rough (1.16 μm) and rubber (1.35 μm).

Bulk-free tests

The results of the bulk-free tests are shown in figure 6.14. The categories, dry, saturated and clay, are divided into three angles: The initial angle is when the first nodule moves. The bulk angle is when the most significant part starts to move, and the final angle is when the last nodules begin to move.

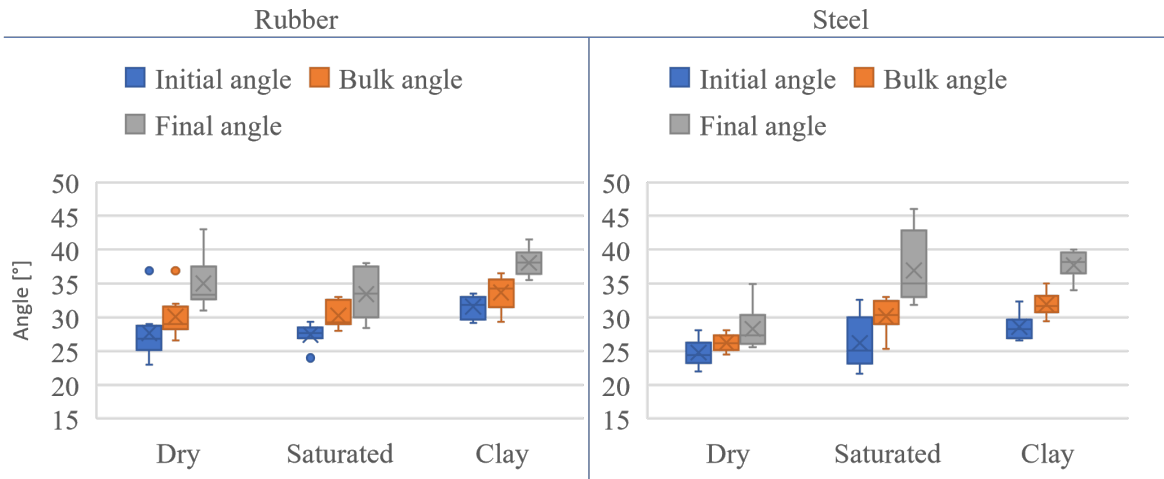


Figure 6.14: Box plot of free bulk tests, all test were repeated 8 times.

Table 6.2: Bulk angle of bulk-free test.

Rubber	Dry	Saturated	Clay
Count [-]	8	8	8
Mean [°]	30.1	30.2	33.7
Confidence Level(95.0%) [°]	2.7	1.6	2.1
Steel	Dry	Saturated	Clay
Count [-]	8	8	8
Mean [°]	26.2	30.2	31.9
Confidence Level(95.0%) [°]	1.0	2.1	1.5

- **Rubber:** The initial angle for clay is higher than the other categories. This could be caused, as in the single nodule test, by the desire of the loose particles to stay together due to the adhesive forces of clay.
- **Steel:** Two outliers of the final angle of the saturated nodules are visible. These were 2 small flat nodule fragments which were adhered to the steel plate. When these are not taken into account, it is visible that clay has the highest friction angles. This again complies with the data from the other experiments.

Confined bulk tests

Figure 6.15 shows the results of the confined bulk test; furthermore, Appendix B.8 shows the histograms.

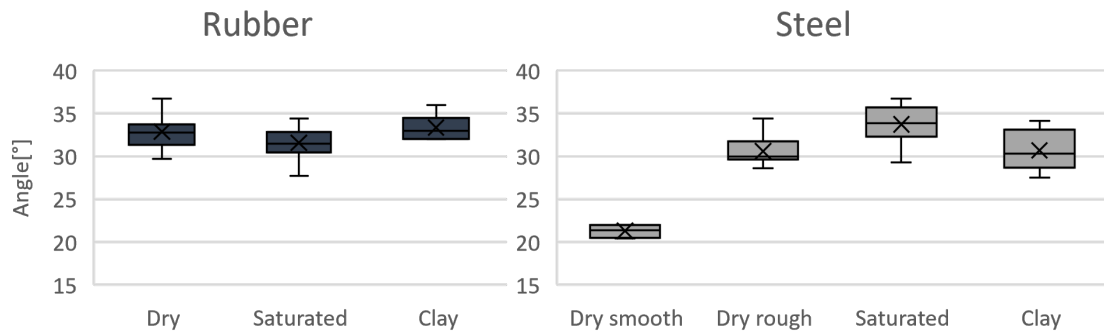


Figure 6.15: Confined bulk box and whisker plot.

Table 6.3: Confined bulk table.

Rubber		Dry	Saturated	Clay
Count [-]		13.0	14.0	6.0
Mean [°]		32.9	31.6	33.3
Confidence Level(95.0%) [°]		1.1	1.0	1.6
Steel	Dry smooth	Dry rough	Saturated	Clay
Count [-]	4.0	17.0	14.0	6.0
Mean [°]	21.3	30.6	33.7	30.7
Confidence Level(95.0%) [°]	1.3	0.8	1.3	2.6

- **Rubber:** There is little difference between dry, saturated, and clay. However, there is a slight difference between the mean values of dry and saturated, about 2°. This could mean a layer of moisture between the nodules and the gliding surface, which makes them slide more easily.
- **Steel:** There is a difference in the average values of saturated, dry and clay. This is the opposite of the difference with rubber. It could be possible that the moisture on steel has a suction effect on the surface, causing the nodules to stick to the surface. However, this would be expected with nodules surrounded by clay due to the high watercontent and adhesion properties. Also in this test, the degradation in the steel plate is visible with dry nodules. It can be concluded that dry nodules are greatly affected by the smoothness of the sliding surface.

Particle size vs friction angle

As indicated in the methods, the single-nodule, free-bulk and confined-bulk tests were also differentiated by particle sizes. Figure 6.16 shows the results. With steel, there is a slight increase in the friction angle as the size of the nodules increases. With rubber, the measured data is too close to be interpreted as a correlation.

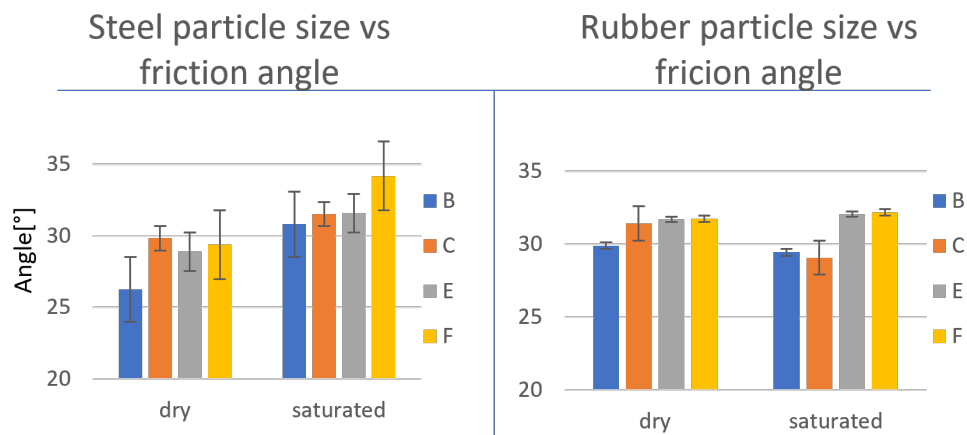


Figure 6.16: Friction angle vs particle size.

Added mass rolling and sliding

The box and whisker plot of the added mass tests on rubber and on steel is displayed in figure 6.17. The blue boxes represent the sliding tests and the orange plots represent the rolling tests. Figure 6.18 shows the corresponding histogram of the tests. The results will be discussed in the following order: Rubber rolling, rubber sliding, steel rolling, steel sliding and finally a comparison will be made.

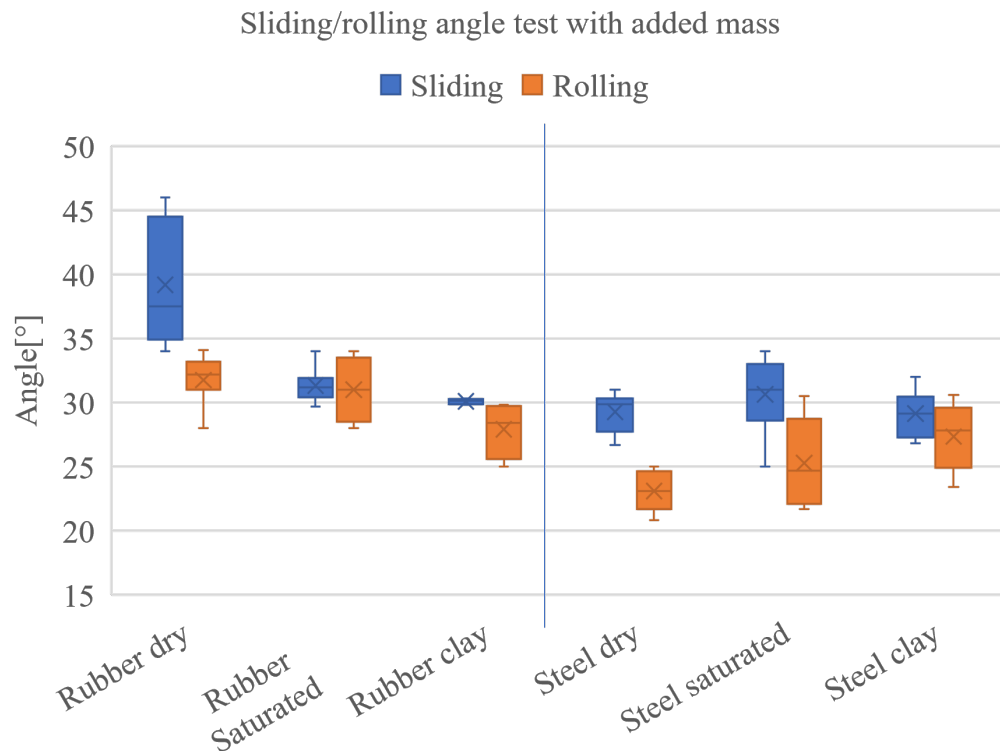


Figure 6.17: Added mass box and whisker plot, for rolling and sliding test together.

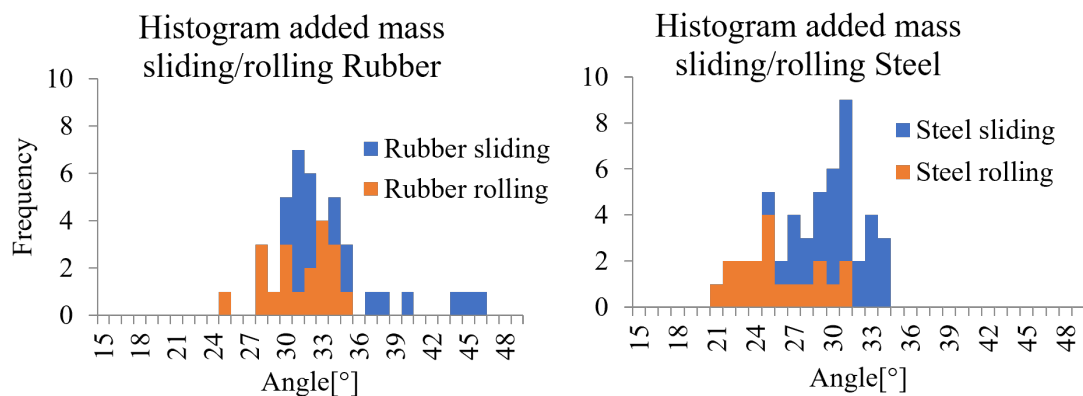


Figure 6.18: Histogram added mass, rolling and sliding.

- **Rubber rolling:** The addition of moisture has little effect on when nodules roll on rubber. However, it is surprising that the results of the clay tests have lower values. These nodules may have acquired a more rounded shape through previous tests.
- **Rubber sliding:** A high friction angle was obtained in the dry tests. The average angle is almost 7° higher than with saturated and clay. This is probably because the extra weight causes compression in the rubber. The angular nodules will plough through the soft surface giving rise to the deformation term of friction. The magnitude of the force

is strongly dependent on the geometry of the ploughing body and the hardness of the softest body[14, 15]. Therefore, this phenomenon is an exception to the friction rule given earlier that the friction angle is independent of the size of the surface. This also explains the large spread in the dry test data, three different blocks were used here, all of which had slightly different nodule fragments. Figure 6.19 shows schematically what happens when a hard surface slides over a rubber surface. The saturated and extra clay nodules did not have this behavior, moisture was probably trapped between the sliding surface and the nodules[15]. This created a layer that made the nodules slide more easily.

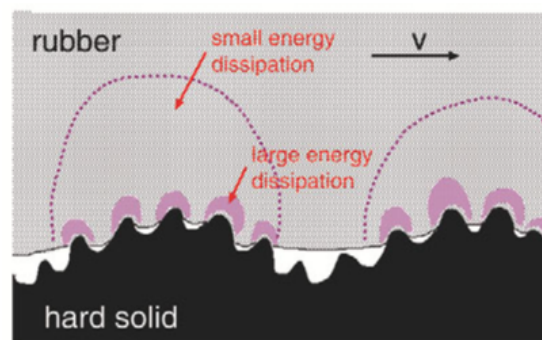


Figure 6.19: Interaction between a hard solid surface and rubber [15].

- **Steel rolling:** There is almost a linear relationship from dry to saturated to clay. The low value of dry could be explained by contamination of the sliding surface. When the nodules are placed on the test track, minimal degradation of the nodules takes place. Circular particles from the nodules or dried clay can end up underneath the nodules. The result of this can be that these small particles have a bearing effect on the whole and therefore cause a small friction angle.

With saturated nodules, this effect will be less because the micro-particles will remain attached to the nodules. the same applies to clay. With clay, there is also adhesive force between the nodules and the sliding surface.

- **Steel sliding:** There is no significant difference between dry, saturated or clay and Abrasion of the nodules is clearly visible as can be seen in figure 6.20. This means that the nodule breaks down locally due to too much shear stress. Clay and moisture are likely pushed out of the contact between the nodules and the steel plate by the high normal force. The Sliding marks on the steel originate from the nodules; the marks are not visible with the surface roughness meter.



Figure 6.20: Abrasion marks on steel plate and on the plaster mold.

Combined results

Stacked histograms all of the test on rubber and steel are depicted in figure 6.21 and appendix B.12. The tests on rubber look normally distributed and steel is more of a peak. This is probably due to the mode of movement. On rubber, the nodules tend to roll more quickly. This gives a considerable spread. On steel, the nodules slide more quickly

Furthermore, The sample variance of the dry tests on rubber is remarkably higher than the other variances. The sliding tests with extra weight caused this difference: An interlocking effect occurred, which increased the friction angle considerably.

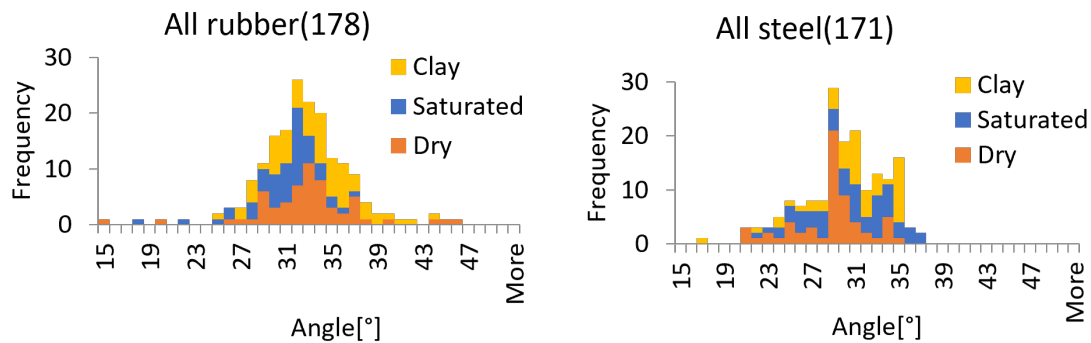


Figure 6.21: The histogram of all the tests conducted on rubber and steel.

Table 6.4: The statistics and histogram of all the tests. All values have angle[°] as unit. The corresponding coefficient of friction can be found in appendix B.13.

<i>Statistics steel</i>	<i>All</i>	<i>Dry</i>	<i>Saturated</i>	<i>Clay</i>
Mean	29.53	28.28	30.07	30.38
Standard Error	0.28	0.42	0.48	0.53
Standard Deviation	3.71	3.27	3.76	3.82
Sample Variance	13.77	10.71	14.11	14.56
Confidence Level(95.0%)	0.56	0.85	0.97	1.07

<i>Statistics rubber</i>	<i>All</i>	<i>Dry</i>	<i>Saturated</i>	<i>Clay</i>
Mean	32.21	32.48	30.54	33.24
Standard Error	0.31	0.63	0.46	0.46
Standard Deviation	4.17	4.88	3.25	3.78
Sample Variance	17.42	23.78	10.57	14.29
Confidence Level(95.0%)	0.62	1.27	0.91	0.91

6.4 Conclusion

In this section, the research questions of this section will be answered. The answers will be supported by table 6.5 the box and whisker plots in figure 6.22 and figure 6.23.

What is the **sliding/rolling friction angle** of nodules placed on a steel slide or a rubber conveyor system when considering different compaction states?

- Rubber: The nodules are more likely to roll than slide. The average angle of movement resulting from 178 data points is equal to $32.21 \pm 0.62^\circ$ which corresponds to a coefficient of friction of 0.63 ± 0.01 . Figure 6.22 shows all rubber results.
- Steel: Sliding is the main mode of movement. The average angle of movement resulting from 171 data points is equal to $29.53 \pm 0.56^\circ$ which corresponds to a coefficient of friction of 0.57 ± 0.01 . Figure 6.23 shows the results for steel.

What is the effect of the particle size on the rolling/sliding friction angles?

- The particle size affects the roll and friction angle to some extent. When the particles are smaller, they are relatively more affected by adhesive forces of water and clay. This results in an increase in friction angle. When the nodules are in a higher compaction state, the difference between nodules sizes is negligible.

What is the effect of **moisture content** on rolling/sliding friction angles?

- Rubber: When comparing dry nodule experimental results with saturated nodule experimental results, it is apparent that the dry friction angle, at $32.48 \pm 1.27^\circ$, is 2° higher than the saturated friction angle with $30.54 \pm 0.91^\circ$.

All saturated tests have average friction angles, independent of the compaction state, within 2 degrees of each other.

- Steel: Dry nodules have a friction angle of $28.28 \pm 0.85^\circ$ and the saturated nodules have a friction angle of $30.07 \pm 0.97^\circ$, this is also equal to 2° , just as for rubber. However, it must be pointed out that the values in the confidence interval are very close to each other. Furthermore, there are significant differences between the different types of saturated tests. The confined nodule tests have provided significantly higher friction angles than single nodules tests. Furthermore, the friction angle drops with the added mass tests. This is presumably an effect of the small adhesive force of water at a low normal force/low compaction state.

What is the effect of **adhesion forces of clay** on rolling/sliding friction angles?

- Rubber: The adhesive force of clay is well represented in the tests without additional weight. On average, these values are all 3° higher than for saturated nodules. The difference arises in the added mass tests, where it is visible that the friction angle has become smaller. This likely happens because the clay layer between the rubber and the nodules has a lubricating effect when the normal force is increased.
- Steel: Just like rubber, the adhesive force of clay can also be seen in the tests without added weight. In the added weight tests, it became clear that the limit of the shear force of nodules had been reached and that an abrasive wear took place. So the clay did not influence this friction angle.
- One side note needs to be addressed about the clay test, the results are highly dependant on the moisture content of the clay, if the clay gets more dry, the adhesive forces will rise. During this test, the clay was kept at a high moisture content to represent the expected condition under water.

How does **normal force** influence the rolling/sliding friction angle?

- Rubber: the increased normal force causes more compression in the rubber and this increases the sliding resistance, but only in dry conditions. When there is moisture or clay between the surfaces, this effect is less noticeable.
- Steel: due to the increased normal force, The moisture is pushed away from the contact points with the steel plate. Therefore, the difference between the dry, saturated and clay tests is almost negligible. Furthermore, the angles are comparable to the tests without extra mass.

What effect do the sliding nodules have on the sliding surface roughness?

- There is a correlation ($R^2 = 0.75$) between the surface roughness and the friction angle of the nodules. Nodules are more likely to break themselves than to make grooves in a plate. Corrosion has a significant impact on the friction angle of the nodules. However, it is possible that the nodules in large numbers have an abrasive effect and thus neutralise the corrosion.

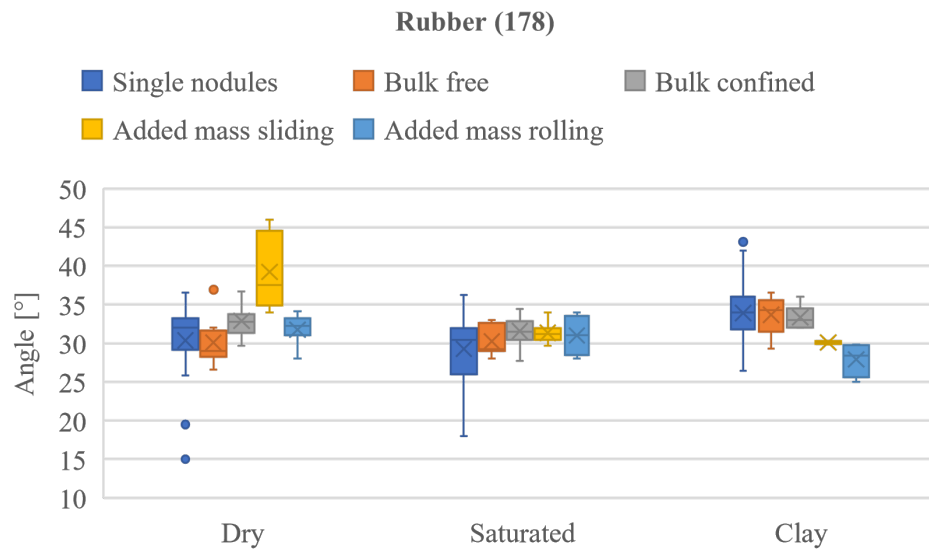


Figure 6.22: Box and whisker plot of all inclined surface tester with rubber as surface. Input values and count can be found in table 6.5.

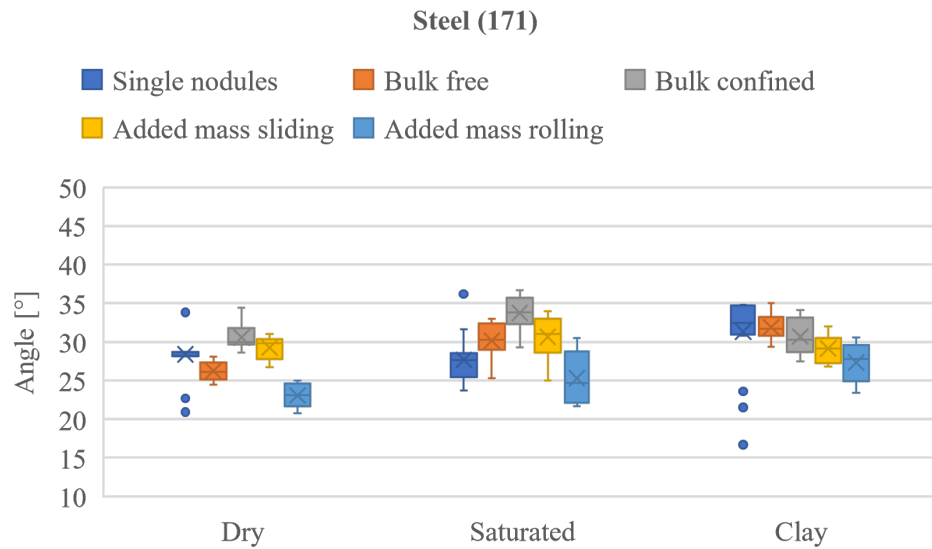


Figure 6.23: Box and whisker plot of all inclined surface tester with steel as surface.

Table 6.5: Summary of of inclined surface tester results.

	<i>Rubber</i>			<i>Steel</i>		
Single nodule	<i>Dry</i>	<i>Saturated</i>	<i>Clay</i>	<i>Dry</i>	<i>Saturated</i>	<i>Clay</i>
Count	18	16	46	23	16	21
Mean [°]	30.4	29.2	33.9	28.4	27.7	31.3
Confidence Level(95.0%) [°]	2.7	2.7	1.2	1.5	1.7	2.2
Bulk free	<i>Dry</i>	<i>Saturated</i>	<i>Clay</i>	<i>Dry</i>	<i>Saturated</i>	<i>Clay</i>
Count	8	8	8	8	8	8
Mean [°]	30.1	30.2	33.7	26.2	30.2	31.9
Confidence Level(95.0%) [°]	2.7	1.6	2.1	1.0	2.1	1.5
Bulk confined	<i>Dry</i>	<i>Saturated</i>	<i>Clay</i>	<i>Dry</i>	<i>Saturated</i>	<i>Clay</i>
Count	13	14	6	17	14	6
Mean [°]	32.9	31.6	33.3	30.6	33.7	30.7
Confidence Level(95.0%) [°]	1.1	1.0	1.6	0.8	1.3	2.6
Added mass sliding	<i>Dry</i>	<i>Saturated</i>	<i>Clay</i>	<i>Dry</i>	<i>Saturated</i>	<i>Clay</i>
Count	9	9	4	6	17	8
Mean [°]	39.2	31.3	30.1	29.3	30.6	29.1
Confidence Level(95.0%) [°]	3.6	1.0	0.3	1.7	1.5	1.5
Added mass rolling	<i>Dry</i>	<i>Saturated</i>	<i>Clay</i>	<i>Dry</i>	<i>Saturated</i>	<i>Clay</i>
Count	11	4	4	6	5	8
Mean [°]	31.7	31.0	27.9	23.1	25.3	27.4
Confidence Level(95.0%) [°]	1.2	4.1	3.6	1.7	4.4	2.1

7 - Design implications

In this master thesis, lab tests were used to clarify the behaviour of degraded polymetallic nodules in a dry and saturated environment. First, the densities of the nodules were examined. Subsequently, tests were carried out to determine the angle of repose. This chapter describes why the angle of repose is an essential parameter for the design of bulk holds and bulk handling equipment like grabs. Moreover, tests were performed to determine the friction angles of nodules on rubber and steel. This parameter is important to consider during the design of the conveyor belts and slides on a ship, as lastly described in this chapter.

7.1 Storage & transport

An example of a dry offload system in the dredging industry is provided in this section, the system has much in common with a nodule harvest operation. Figure 7.1 depicts a dry offloading method of a trailing hopper dredge with the use of a bucket wheel and a conveyor belt. The hopper of this vessel has been filled with sand but is also designed to handle gravel. Gravel (2-32 mm [76]) is likely of similar particle size as the nodules if these are hydraulically transported to the surface. The application of the bucket wheel in combination with a conveyor belt could be a possible solution for the transport from the MSV hopper to the transport ship.

The output of the bucket wheel is primarily determined by the amount of material it can carry. An important design parameter, in this case, is the angle of repose of the material: With a low angle of repose, the bucket can be filled to the brim; With a high angle of repose, a pile will form above the brim of the bucket, increasing production. Furthermore, the power of the wheel must be able to cope with this production.

When a bucket is at the top of the wheel, the production will slide out from the bucket; a friction angle determines when the material starts to slide: With a high friction angle, the material will fall out later, and with a low angle, it will start sliding earlier. A collection tray must be placed above the conveyor belt to distribute the material uniformly and ensure that the material reaches the conveyor belt.

In the process of emptying the hopper, the bucket wheel will sink deeper into the ship in order to maintain production. This increases the angle of the conveyor belt behind it. The angle of repose and the friction angle indicate the maximum angle that can be achieved.



Figure 7.1: Example of a bucket wheel self offload system on a trailing hopper dredge to offload material in a dry state (Reimerswaal dredging).

8 - Conclusion and recommendation

This thesis is divided into theory and experimental sections, as stated in the introduction. The theory mainly focused on the topside processes and nodule properties, and the experiments focused on the characteristics of degraded polymetallic nodules in the context of bulk handling. The main conclusions are reproduced here.

8.1 Theory

What are effective strategies to dewater polymetallic nodules in a confined space on a mining support vessel?

- The dewatering process of polymetallic nodules results into two streams. The first one is a stream of dewatered solids, because “free” water has been removed from around the nodules using vibrating plates and screens. Hence, the second stream is runoff water, potentially still rich in fines and sediment, of which separation of fines may still be economically viable. However, economic feasibility was not included in the scope of this research. The fines can be removed using hydrocyclones and filter presses.
- The extent to which dewatering processes are necessary depends mainly on the allowable maximum moisture content and the number of fines present in the storage of the mining support vessel and the bulk carriers. Moisture maximum prevents processes such as liquefaction and dynamic separation.

How do the dewatering strategies at sea compare to land based dewatering installations?

- There are four significant differences between dewatering installations on land and at sea.
 - Space on a ship is limited, so the layout must be more compact in comparison to land.
 - The static environment on land has turned into a dynamic environment at sea. This ensures that gravity sedimentation will have problems with the separation of the fines due to flows in the sedimentation tank.
 - The production of the mining vehicle will be continuous, making batch dewatering and separation methods impractical.
 - The mining support vessel has a limited amount of available energy, meaning that choices have to be made with regard to energy efficient methods of dewatering.

What are the physical states and their corresponding aspects to consider when handling polymetallic nodules?

- The research on the material properties on polymetallic nodules is mainly focused on fully intact nodules.
- From the moment the polymetallic nodules are lifted from the seabed, the degradation process starts; On the bulk parameters of degraded polymetallic nodules, there are only few publications available in the public domain .

It is crucial to better understand the characteristics of degraded polymetallic nodules in the context of bulk handling. Optimization of the dewatering and transport installations can be achieved. The next section will elaborate on this subject.

8.2 Experiments

How do the **densities** of the IHC nodules compare to the nodules from other sites of which experiments are published in available literature?

- The measurements conducted on the nodules from IHC provided a saturated density of 1.911 g/cm^3 with a 95% confidence interval of 0.035 g/cm^3 . This density value is similar to those examined in neighbouring areas, within 5% difference to the nodules measured in the research of Dreiseitl[18], GSR[64] and Neizvestnov[49]. There is a larger difference with other studies, up to 30%. This is possibly caused by measuring errors, different nodule harvest locations and the moment of measuring: immediately after the nodules were lifted from the seabed or after a longer period in a lab environment.

Recommendation:

- It is important to use another method to determine the volume to rule out measurement errors completely; a tomography scan would provide a solution.

Is photogrammetry with Qlone an effective method for scanning polymetallic nodules?

- A rapid modeling application like Qlone Has proven a scanning speed of 5 minutes for a single nodule and an accuracy of less than 5 mm in all directions. Concluding that the quality of Qlone is sufficient to recreate shapes of nodules and nodule fragments in a digital environment.

Recommendation

- Software like Qlone seems suitable to determine the sphericity, angularity and roundness of polymetallic nodules. Opening the opportunity for improved modelling in which a large number of scans of actual nodules serves as input for a design of bulk handling equipment model. The remainder of this thesis, however, focuses on further experimental measurements with degraded nodules provided by IHC, for there is no current literature on the following experiments executed with nodules as such.

What is the **angle of repose** of degraded polymetallic nodules and how is it influenced by moisture content?

- The angle of repose for polymetallic nodules of the size range 10 - 16 mm nodules is 49.5 ± 1.46 . The results were obtained by using the ledge tester.
- The data shows that the difference between saturated and dry material is insignificant.

Recommendations:

- Depending on the chosen VTS, the nodule sizes will be different, ranging from 20 mm with hydraulic transport to possibly bigger nodule sizes with air lift. Additional tests should be conducted on many larger and smaller batches of particle sizes for a complete picture.
- According to Hashemi[73], there are 9 different methods to determine the angle of repose, with different results for every type of test. Be aware that these angles of repose are not one to one comparable with the angle of repose resulting from the ledge tester.

- Although the ledge test has proven sufficient to compare the angle of repose of moist and dry nodules, the design and simulations of the transport and storage operation could benefit from an additional draw down angle of repose test. In this type of test, a batch of nodules is placed on a hatch. Subsequently, the hatch is opened and the accumulation of the nodules on a surface is followed over time resulting in an angle of repose. One advantage of the draw-down test is information obtained on the time it takes to develop a steady angle of repose. Two disadvantages are: More degradation of the sample, and a greater required nodule quantity in comparison with the ledge test.

What is the **sliding/rolling friction angle** of nodules placed on a steel slide or a rubber conveyor system when considering different compaction states?

- Rubber: The nodules are more likely to roll than slide. The average angle of movement resulting from 178 data points is equal to $32.21 \pm 0.62^\circ$ which corresponds to a coefficient of friction of 0.63 ± 0.01 . Figure 6.22 shows all rubber results.
- Steel: Sliding is the main mode of movement. The average angle of movement resulting from 171 data points is equal to $29.53 \pm 0.56^\circ$ which corresponds to a coefficient of friction of 0.57 ± 0.01 . Figure 6.23 shows the results for steel.

What is the effect of **moisture content** on rolling/sliding friction angles?

- Rubber: When comparing dry nodule experimental results with saturated nodule experimental results, it is apparent that the dry friction angle, at $32.48 \pm 1.27^\circ$, is 2° higher than the saturated friction angle with $30.54 \pm 0.91^\circ$.

All saturated tests have average friction angles, independent of the compaction state, within 2 degrees of each other.

- Steel: Dry nodules have a friction angle of $28.28 \pm 0.85^\circ$ and the saturated nodules have a friction angle of $30.07 \pm 0.97^\circ$, this is also equal to 2° , just as for rubber. However, it must be pointed out that the values in the confidence interval are very close to each other. Furthermore, there are significant differences between the different types of saturated tests. The confined nodule tests have provided significantly higher friction angles than single nodules tests. Furthermore, the friction angle drops with the added mass tests. This is presumably an effect of the small adhesive force of water at a low normal force/low compaction state.

What effect do the sliding nodules have on the sliding surface roughness?

- There is a correlation ($R^2 = 0.75$) between the surface roughness and the friction angle of the nodules. Nodules are more likely to break themselves than to make grooves in a plate. Corrosion has a significant impact on the friction angle of the nodules. However, it is possible that the nodules in large numbers have an abrasive effect and thus neutralise the corrosion.

8.3 main research question

With the information from the previous chapters, the answer to the main question can be given with a high level of confidence:

What is the effect of moisture on the granular characteristics of polymetallic nodules in the context of bulk handling?

- Considering the angle of repose tests and the sliding and rolling friction angle, it is evident that the difference between dry and fully saturated nodules is minimal. For the friction angle: The maximum deviation between dry, saturated and CCZ clay is 8 % on steel and 9 % on rubber, corresponding to $\pm 2^\circ$. For the angle of repose, the difference between dry and saturated is negligible. It is concluded that the moisture content only contributes minimal level to bulk behaviour of nodules.

Recommendation

Overall, the shape and surface roughness influenced this research greatly. The shape influenced the rolling behaviour, and the angle of repose and the surface roughness influenced the sliding friction. Unfortunately, it is not yet clear what the actual shape of the nodules will be: The abrasive wear during vertical transport from the seabed could cause a rounding effect.

Furthermore, it would be interesting to calibrate DEM software using the already conducted tests. This could contribute to possible design choices.

A - Literature

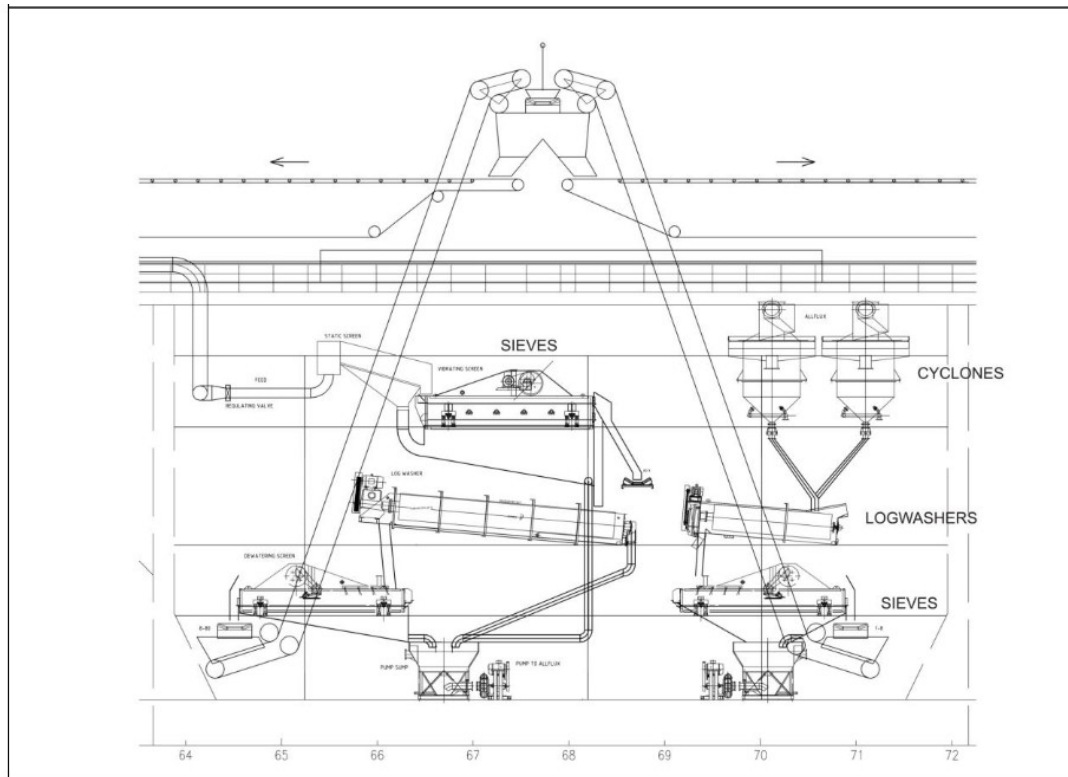


Figure 22: Separation plant concept. Sediment is processed through sieves, logwashers and cyclones. No chemicals are used.

Figure A.1: Dewatering setup Chatham Rock Phosphate Limited[8].

B - Experimental methods

B.1 PSD and properties

PSD can be created to represent a collection of different sized particles. In a PSD, the particle diameter is plotted against the cumulative weight percentage. A sieving analysis is done on the provided sample of polymetallic nodules to make a PSD curve: When the nodule does not fit through the sieve, it will be assigned to this size class. After the sieving is done, all the classes are weighted. Next, the cumulative percentage can be determined for each class and this can be plotted into a figure to make a PSD curve.

Table B.1: PSD input values.

Classification	Size of nodules [mm]	Sieve size [mm]	Weight [g]	Percentage of soil retained at each sieve [%]	Percent Finer [%]
	100+		0	0.00	100
A	70- 100	100	4860.4	9.17	90.834
B	50 - 70	70	10550	19.90	70.939
C	30 - 50	50	19248.8	36.30	34.640
D	25 - 30	30	1866.6	3.52	31.120
E	16 - 25	25	8793	16.58	14.538
F	10 -16	16	4425.1	8.34	6.193
G	4 - 10	10	1452	2.74	3.455
H	2.8 - 4	4	166.9	0.31	3.140
I	1 - 2.8	2.8	483.9	0.91	2.228
J	0.5 - 1	1	526.1	0.99	1.236
K	<0.5	0.5	655.3	1.24	0.000
Sum			53028.1	100.0000	

The PSD and the related Histogram are presented in figure B.1. It is evident that it is the class of 50 to 70 mm that has the largest share of the container. The small dip at the 30 mm size can be explained by the small sieve interval.

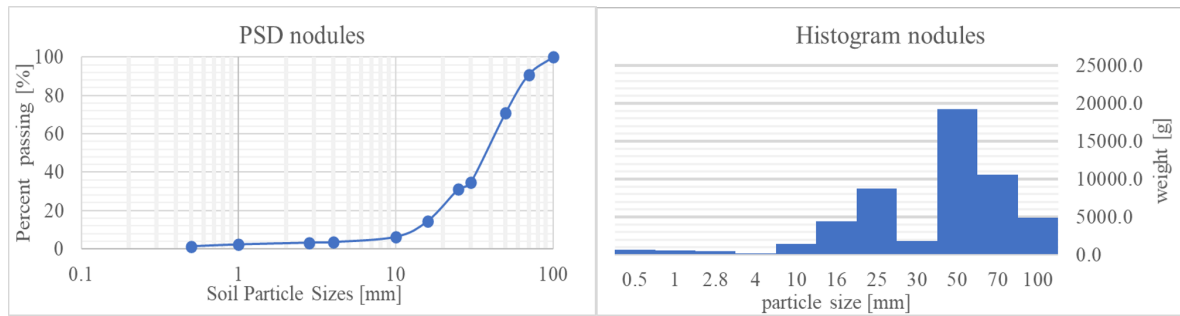


Figure B.1: Particle size distribution and a histogram.

B.2 Particle properties

Figure B.2 shows the settings of the UF260 oven which was used to dry the nodules.

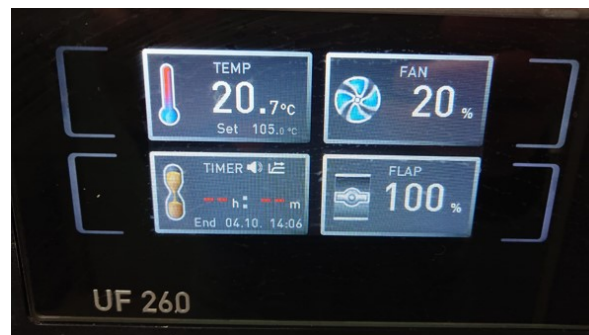


Figure B.2: Settings of the oven: Temperature is set at 105°C, ventilation at 20%, timer at 24 hours and ventilation flap was set to 100% to remove moisture from the oven.

Requirements for density measurements

- Oven capable of reaching 105°C for more than 24 hours
- Scale
- Heat-resistant trays
- Measuring beaker
- Fully saturated nodules

B.3 Angle of repose

This section starts with a roadmap used while conducting the angle of repose tests—followed by an image of the Matlab tool and the corresponding code, which was used to read out the angle of repose. Finally, the data and the histogram are shown.

1. Let batch of nodules saturate in water for 48 hours.
2. Remove free water

3. Setup camera
4. Place nodules inside test device
5. Check if test device is levelled.
6. Take photo of setup
7. Remove door
8. Take photo of test
9. Place batch of nodules back in bin and repeat from step 4
10. Repeat tests with batch of dry nodules.

Angle of repose Matlab script

Figure B.3 shows the processing of the result photos. Followed by the Matlab script used for determining the angle.

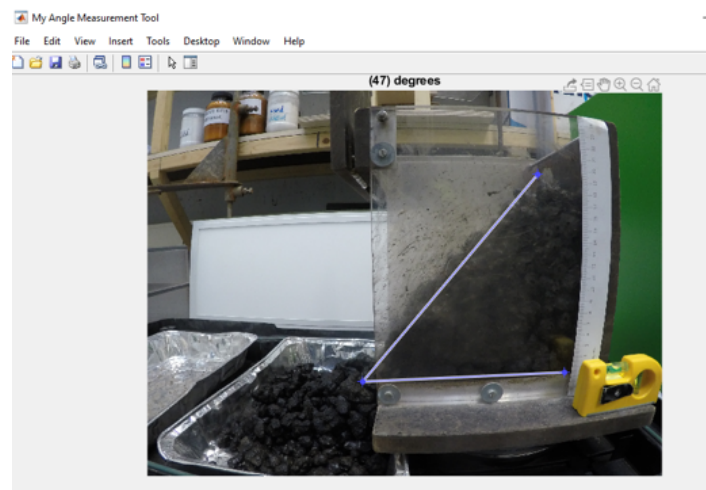


Figure B.3: Shows a saturated angle of repose test with the angle measurement tool in matlab.

```

1  function my_angle_measurement_tool(im)
2  % Create figure, setting up properties
3  figure('Name','My Angle Measurement Tool',...
4         'NumberTitle','off',...
5         'IntegerHandle','off')
6
7  % Display image in the axes % Display image
8  imshow(im)
9
10 % Get size of image.
11 m = size(im,1);
12 n = size(im,2);
13
14 % Get center point of image for initial positioning.
15 midy = ceil(m/2);
16 midx = ceil(n/2);
17
18 % Position first point vertically above the middle.
19 firstx = midx;
20 firsty = midy - ceil(m/4);
21 lastx = midx + ceil(n/4);
22 lasty = midy;
23
24 % Create a two-segment right-angle polyline centered in the image.
25 h = impoly(gca,[firstx , firsty ; midx , midy ; lastx , lasty] , 'Closed' , false);
26 api = iptgetapi(h);
27 initial_position = api.getPosition()
28
29 % Display initial position
30 updateAngle(initial_position)
31
32 % set up callback to update angle in title.
33 api.addNewPositionCallback(@updateAngle);
34 fcn = makeConstrainToRectFcn('impoly',get(gca,'XLim'),get(gca,'YLim'));
35 api.setPositionConstraintFcn(fcn);
36 %
37
38 % Callback function that calculates the angle and updates the title.
39 % Function receives an array containing the current x,y position of
40 % the three vertices.
41 function updateAngle(p)
42 % Create two vectors from the vertices.
43 % v1 = [x1 - x2, y1 - y2]
44 % v2 = [x3 - x2, Y3 - y2]
45 v1 = [p(1,1)-p(2,1) , p(1,2)-p(2,2) ];
46 v2 = [p(3,1)-p(2,1) , p(3,2)-p(2,2) ];
47 % Find the angle.
48 theta = acos(dot(v1,v2)/(norm(v1)*norm(v2)));
49 % Convert it to degrees.
50 angle_degrees = (theta * (180/pi));
51 % Display the angle in the title of the figure.
52 title(sprintf('(%1.0f) degrees',angle_degrees))

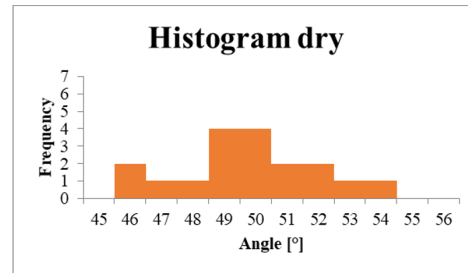
```

my_angle_measurement_tool.m

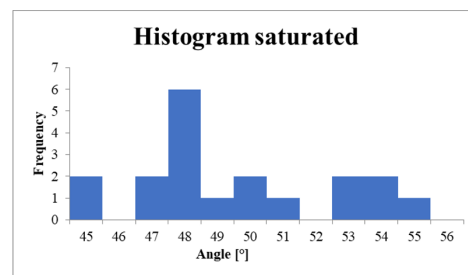
Data angle for repose test

The two tables on the left of figure B.4 show the measurement results of the dry and saturated tests. Next to the table are the histograms and the most important statistics. An error occurred on test 16 of the dry tests, therefore, this test is removed from the results.

Saturated		Dry	
ex nr:	Angle [°]	ex nr:	Angle [°]
1	48	1	48
2	54	2	46
3	50	3	46
4	53	4	50
5	45	5	47
6	48	6	52
7	45	7	50
8	53	8	51
9	49	9	51
10	47	10	49
11	50	11	52
12	48	12	50
13	47	13	53
14	55	14	50
15	48	15	49
16	54	17	49
17	51	18	54
18	48	19	49
average	49.6	average	49.8



Mean	49.5
Standard Error	0.69
Median	48
Confidence Level(95.0%)	1.46



Mean	49.78
Standard Error	0.52
Median	50
Confidence Level(95.0%)	1.10

Figure B.4: Angle of repose histogram and test results.

B.4 Rolling and sliding friction angle

info CCZ clay

The Royal Netherlands Institute for Sea Research (NIOZ) provided 2 kg of deep sea sediment out of the CCZ. This sediment helps simulate realistic scenarios where the nodules just left the seabed with the sediment still attached. Figure B.5 shows how the clay was used. First, the clay was dissolved in water to increase the watercontent. Hereafter, the nodules were placed in the bath with sediment and water. Lastly, the nodules were stirred around in a sieve to remove some of the excess clay particles; this process would recreate the effect of a riser system on the nodules



Figure B.5: CCZ sediment used to simulate sediment effects on nodules.

B.4.1 Single nodule test

Figure B.6 displays the results of the single nodule tests: The left graphs side of the image shows the test results on rubber, and the right side shows the results of the tests on a steel plate

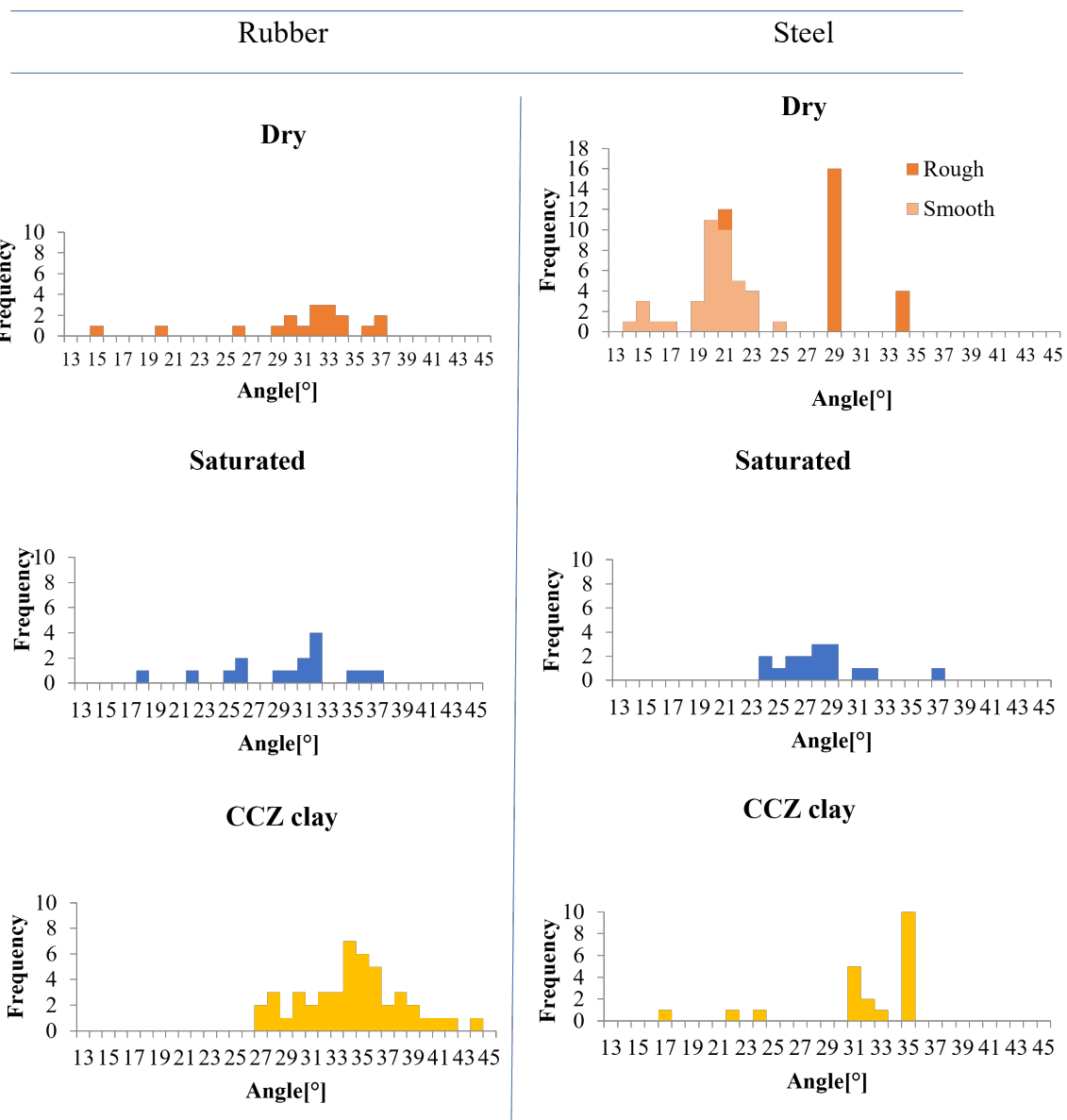


Figure B.6: Single nodules histogram.

B.4.2 Bulk tests free

Figure B.7 shows the results of the Bulk free tests. The decision is made to switch the dry results with the saturated results to increase the contrast between the results. It can be seen that there is a difference between clay and dry on steel. Furthermore, it is noticeable that there is little difference between the various tests on rubber.

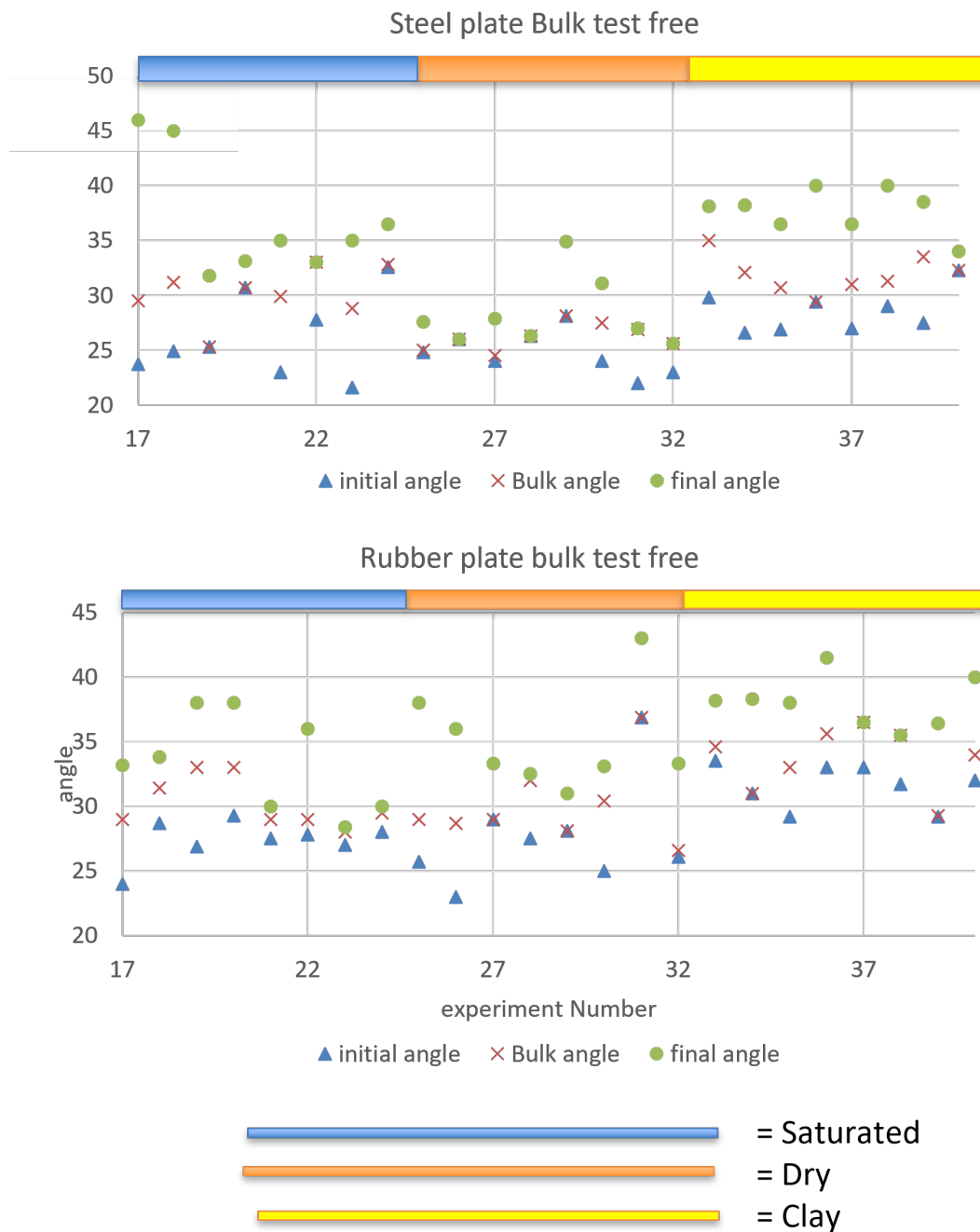


Figure B.7: Bulk free data plotted.

B.4.3 Confined bulk tests

In figure B.8 displays the results of the single nodule tests: The left graphs side of the image shows the test results on rubber, and the right side shows the results of the tests on a steel plate.

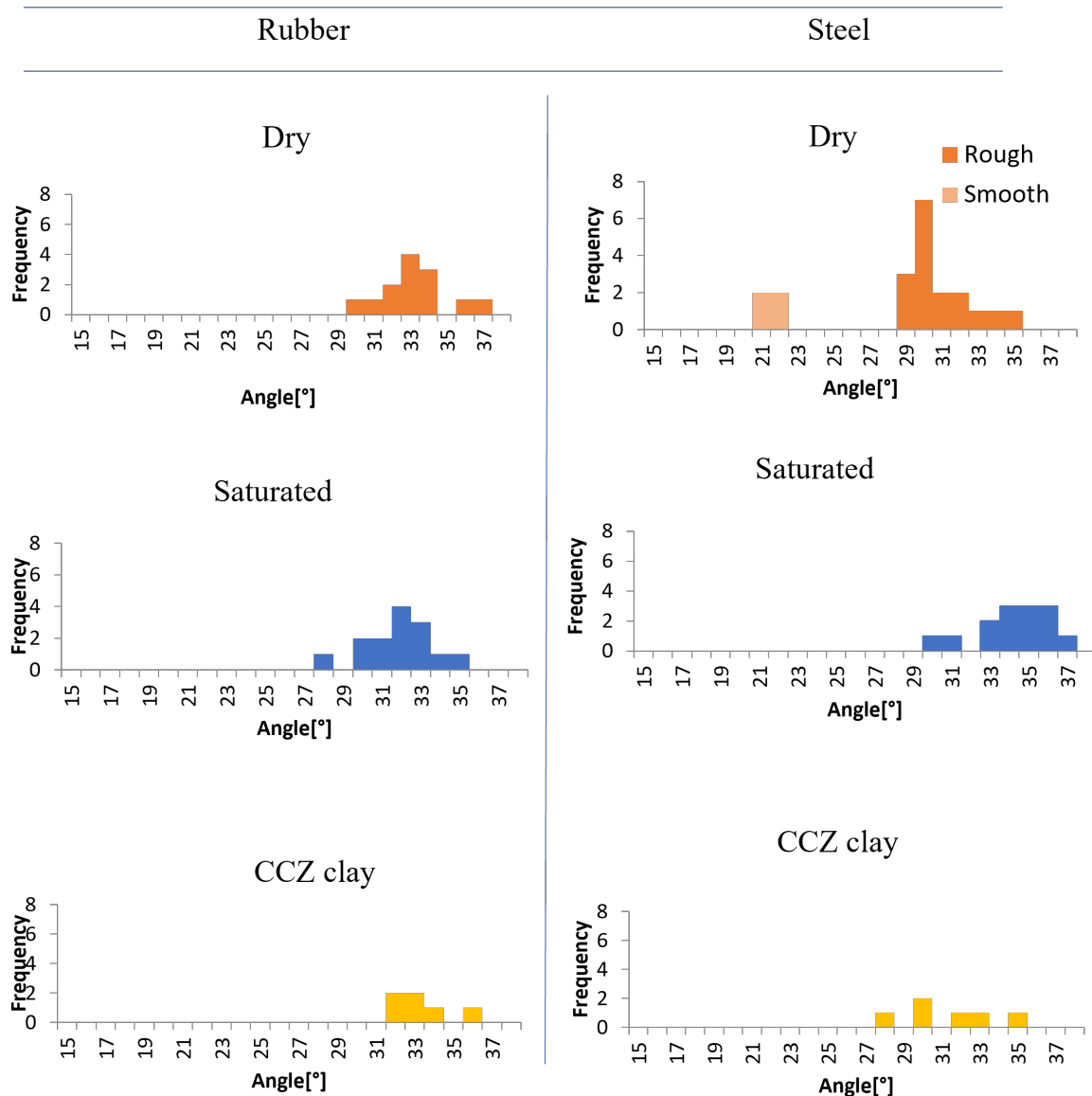


Figure B.8: Confined bulk histogram.

B.4.4 Surface roughness measurements

Surface roughness, often shortened to roughness, is a component of surface texture. It is quantified by the deviations in the direction of the normal vector of a real surface from its ideal form. If these deviations are large, the surface is rough; if they are small, the surface is smooth.

Equation B.1 shows average roughness, Ra , which is the most widely used one-dimensional roughness parameter. Where l_r is the evaluation length and $z(x)$ is deviation about the center line.

$$Ra = \frac{1}{l_r} \int_0^{l_r} |z(x)| dx \quad (\text{B.1})$$

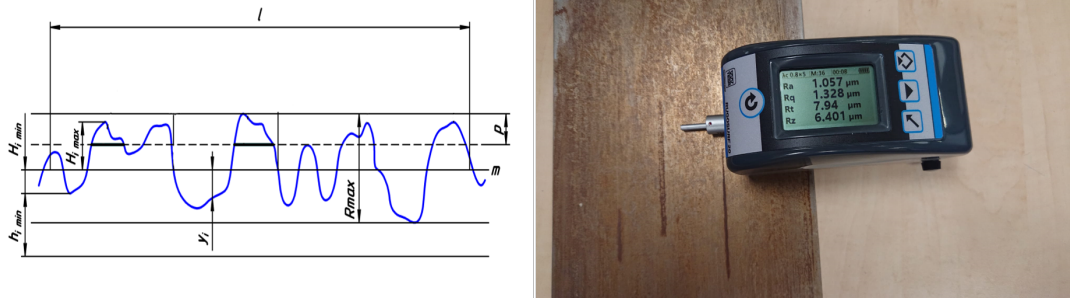


Figure B.9: The left graph shows a example of cross section of a surface. The right figure shows the measuring device.

Figure B.10 shows the measurements of the roughness meter. The plate is divided into 5 cm by 3 cm squares, and a measurement is taken in each square. Furthermore, these tests were carried out on the 8th of December and then repeated on the 23rd of December. Sliding tests were conducted between these two test data. The difference between the two tests is marginal. Therefore, it can be stated that the degradation of the plate did not continue; the plate has reached a stable condition.

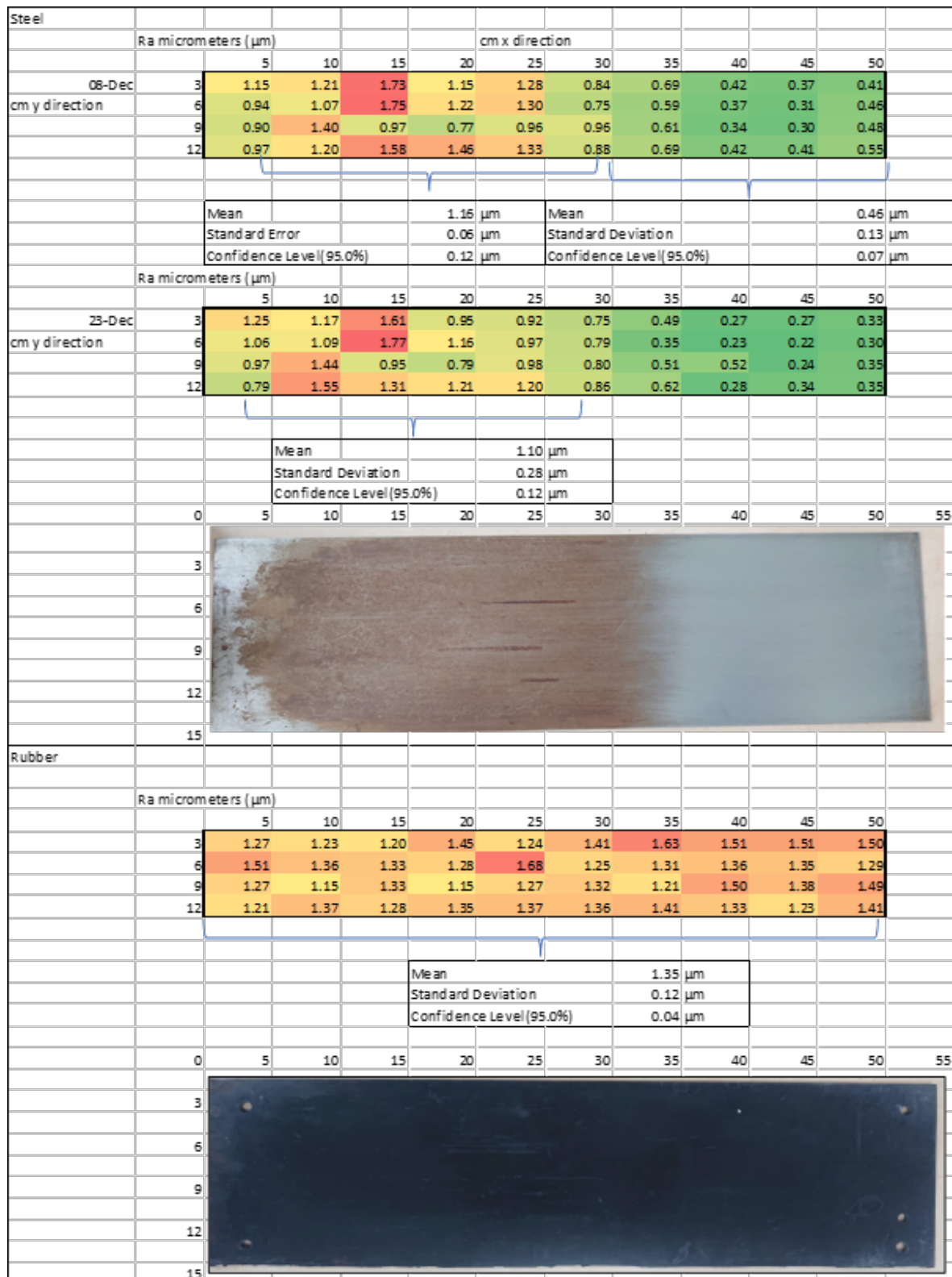


Figure B.10: Surface roughness results.

Table B.2 shows the raw data of the dry nodules tests on the smooth and rough side of the steel and the rubber plate.

Table B.2: Input data for figure 6.13.

Smooth steel			Rough steel			Rubber		
test nr	Ra [μm]	Angle[°]	Test nr.	Ra [μm]	Angle[°]	Test nr.	Ra [μm]	Angle[°]
1	0.46	21.9	1	1.16	22.7	Sliding		
2	0.46	21.9	2	1.16	20.9	1	1.35	35.3
3	0.46	14.7	3	1.16	28.5	2	1.35	30.8
4	0.46	24.6	4	1.16	28.5	3	1.35	29.2
5	0.46	14	5	1.16	28.7	4	1.35	32
6	0.46	20	6	1.16	33.8	5	1.35	29
7	0.46	15.1	7	1.16	33.8	6	1.35	32.2
8	0.46	18.3	8	1.16	28.2	7	1.35	32
9	0.46	20.2	9	1.16	28.2	8	1.35	32.4
10	0.46	21.8	10	1.16	28.2	Rolling		
11	0.46	21.7	11	1.16	28.2	9	1.35	15
12	0.46	18.9	12	1.16	28.2	10	1.35	33.2
13	0.46	14.5	13	1.16	20.9	11	1.35	33.2
14	0.46	14.5	14	1.16	28.5	12	1.35	31.8
15	0.46	16.8	15	1.16	28.5	13	1.35	25.8
16	0.46	21.3	16	1.16	28.7	14	1.35	29.3
17	0.46	18.1	17	1.16	33.8	15	1.35	36.5
18	0.46	21	18	1.16	33.8	16	1.35	36.5
19	0.46	20.7	19	1.16	28.2	17	1.35	19.5
20	0.46	20.7	20	1.16	28.2	18	1.35	32.6
21	0.46	20.7	21	1.16	28.2			
22	0.46	20.7	22	1.16	28.2			
23	0.46	19.7	23	1.16	28.2			
24	0.46	19.7						
25	0.46	19.8						
26	0.46	19.8						
27	0.46	19.8						
28	0.46	22.7						
29	0.46	22.7						
30	0.46	20.7						
31	0.46	20.7						
32	0.46	20.7						
33	0.46	20.7						
34	0.46	19.7						
35	0.46	19.7						
36	0.46	19.8						
37	0.46	19.8						
38	0.46	19.8						
39	0.46	22.7						

B.4.5 Added mass tests

This section will show the results of the added mass tests and information about the design of the sledge.

3D printed sledge

With the use of Solidworks, a solid modeling computer-aided design (CAD), a sledge has been designed and printed for the Added weight test in section 6.2

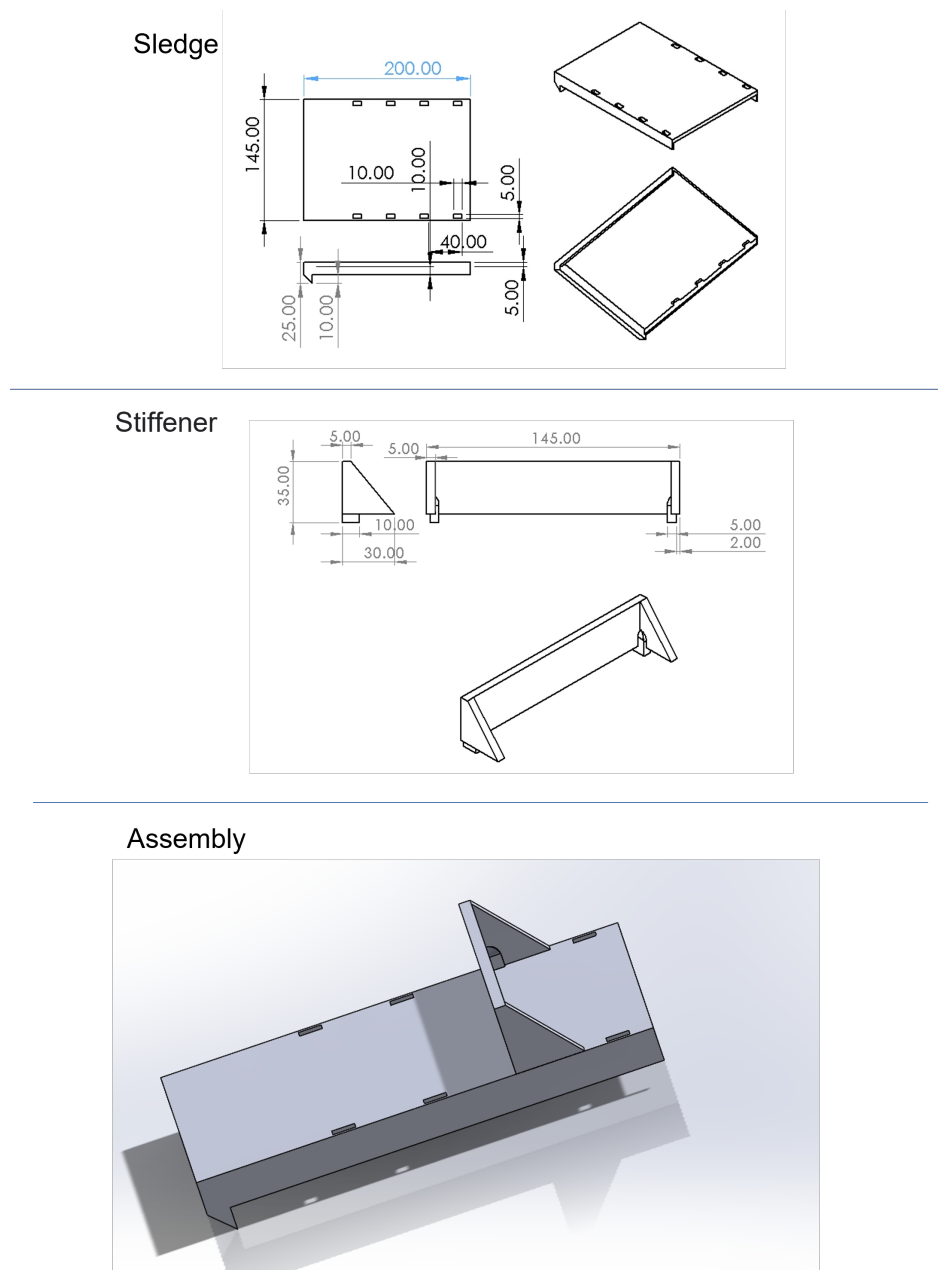


Figure B.11: 3D model of sledge for added weight testing.

B.4.6 All tests combined

A histogram of all sliding and rolling experiments is given in figure B.12

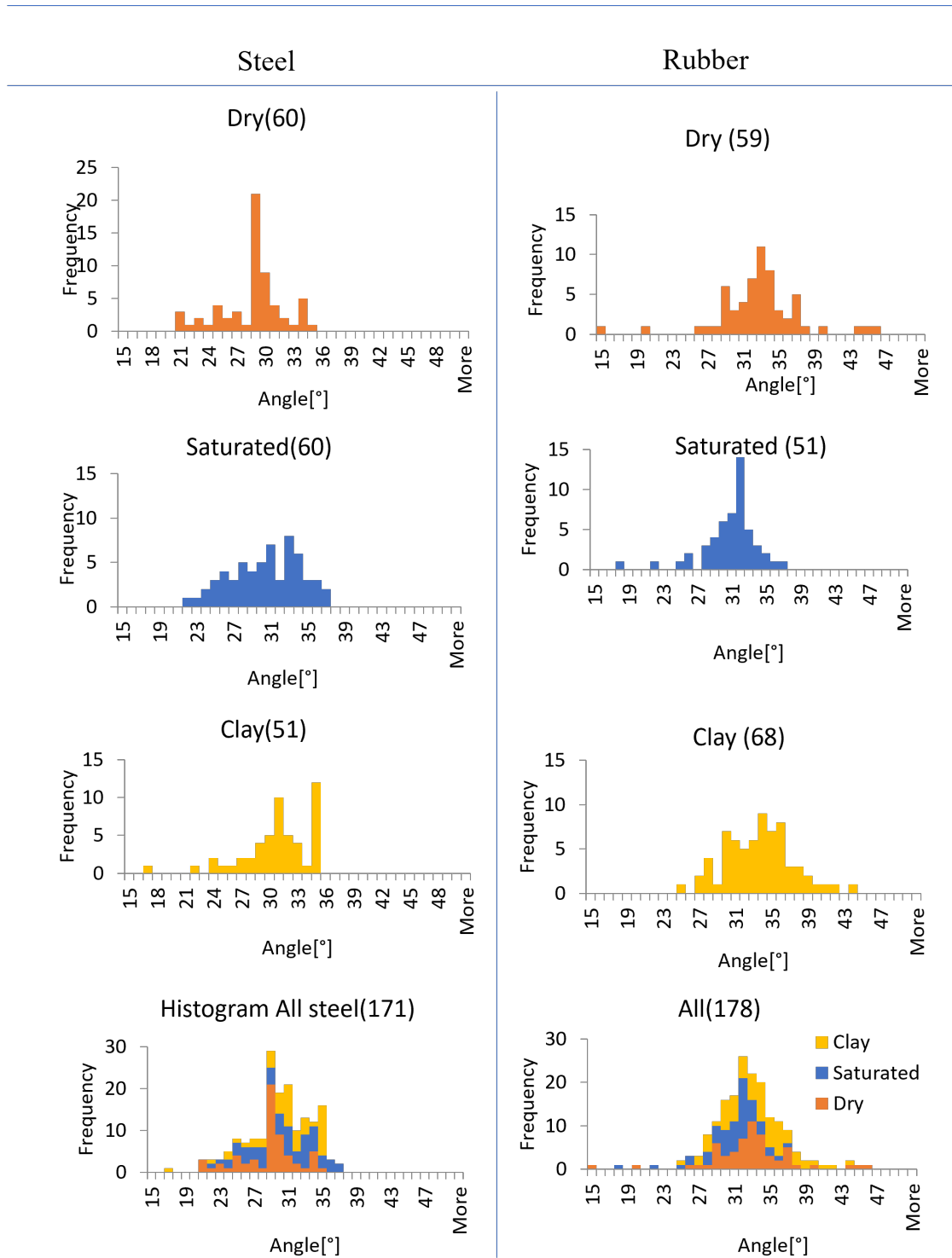


Figure B.12: Histogram of all the tests combined.

<i>Statistics Steel</i>	<i>All</i>	<i>Dry</i>	<i>Saturated</i>	<i>Clay</i>
Mean	0.57	0.54	0.58	0.59
Standard Error	0.005	0.01	0.01	0.01
Standard Deviation	0.06	0.06	0.07	0.07
Sample Variance	0.25	0.19	0.25	0.26
Confidence Level(95.0%)	0.01	0.01	0.02	0.02

<i>Statistics rubber</i>	<i>All</i>	<i>Dry</i>	<i>Saturated</i>	<i>Clay</i>
Mean	0.63	0.64	0.59	0.66
Standard Error	0.01	0.01	0.01	0.01
Standard Deviation	0.07	0.09	0.06	0.07
Sample Variance	0.31	0.44	0.19	0.25
Confidence Level(95.0%)	0.01	0.02	0.02	0.02

Figure B.13: Table with friction factor instead of angle.

Bibliography

- [1] O. Hefferman, “Deep-sea dilemma: Mining the ocean floor could solve mineral shortages – and lead to epic extinctions in some of the most remote ecosystems on Earth,” *Nature*, vol. 571, 2019. [Online]. Available: <https://media.nature.com/original/magazine-assets/d41586-019-02242-y/d41586-019-02242-y.pdf>
- [2] L. A. Van Paassen, P. J. Vardon, and P. Jeffrey, “Cargo liquefaction in bulk carriers: a review,” in *Yearbook Mijnbouwkundige Vereeniging 2015*, Delft, 2015. [Online]. Available: <https://www.researchgate.net/publication/299217743>
- [3] A. M. Lang, S. Dasselaar, K. Aasly, and E. Larsen, “Blue Nodules Deliverable report D3.4 Report describing the process flow overview,” The European Union framework programme for research and innovation, Tech. Rep., 2019. [Online]. Available: https://blue-nodules.eu/download/public_reports/public_reports/Blue-Nodules-688975-D3.4-Report-describing-the-process-flow-overview-FINAL.pdf
- [4] S. A. Schulte, “Vertical transport methods for Deep Sea Mining,” Master’s thesis, TU Delft, Delft, 6 2013.
- [5] E. de Hoog, J. M. van Wijk, J. T. Wijnands, and A. M. Talmon, “Degradation of polymetallic nodules during hydraulic transport under influence of particle-wall and particle-particle interaction,” *Minerals Engineering*, vol. 155, 2020.
- [6] Rollier, “Vibrating Dewatering screens.” [Online]. Available: <https://rollier.com/portfolio-items/vibrating-dewatering-screens-series-ess/>
- [7] A. Vrij and S. Boel, “Blue Nodules Deliverable report D4.5 Mining Platform Deliverable Report: Final (revised),” The European Union framework programme for research and innovation, Tech. Rep., 2020.
- [8] Chatham Rock Phosphate Limited, “Marine Consent Application and Environmental Impact Assessment Volume One,” Tech. Rep., 2014.
- [9] M. Wasilewska-Błaszczuk and J. Mucha, “Possibilities and limitations of the use of seafloor photographs for estimating polymetallic nodule resources—case study from IOM area, Pacific ocean,” *Minerals*, vol. 10, no. 12, pp. 1–21, 12 2020.
- [10] Y. Xie, Z. Yang, and D. Barreto, “The Influence of Particles’ Aspect Ratio on the Shear Behaviour of Granular Materials,” in *Springer Proceedings in Physics*, vol. 188, 12 2017, pp. 253–264.
- [11] R. Pitchumani, O. Zhupanska, G. Meesters, and B. Scarlett, “Measurement and Characterization of Particle Strength Using a New Robotic Compression Tester,” *Powder Technology*, vol. 143, pp. 56–64, 6 2004.
- [12] Global Bauxite Working Group, “Report on Research into the Behaviour of Bauxite during Shipping,” Tech. Rep., 2017.
- [13] “Action Cam Lens Distort, a grid representing the natural curvature of a GoPro HERO4.” [Online]. Available: <https://www.manula.com/manuals/fxhome/ignite-pro/5/en/topic/action-cam-lens-distort>

- [14] E. Deladi, “Static friction in rubber-metal contacts with application to rubber pad forming processes,” Ph.D. dissertation, University of Twente, Enschede, 2006.
- [15] B. Lorenz, B. Persson, S. Dieluweit, and T. Tada, “Rubber friction: Comparison of theory with experiment,” *The European physical journal. E, Soft matter*, vol. 34, pp. 1–11, 12 2011.
- [16] K. Sanjay, A. Rauf Sheik, P. Sahu, G. Kuttikrishnan, R. Ananda Gidugu, and M. Atmanand, *Studies on techniques for dewatering of polymetallic manganese nodules*. Shanghai: ISOPE, 11 2020. [Online]. Available: <https://onepetro.org/ISOPEIOPEC/proceedings-abstract/ISOPE20/All-ISOPE20/ISOPE-I-20-1109/446248>
- [17] B. A. Wills and J. A. Finch, *Wills mineral processing technology: an introduction to the practical aspects of ore treatment and mineral recovery*, 8th ed. Oxford: Elsevier/Butterworth-Heinemann, 2016.
- [18] I. Dreiseitl, “About geotechnical properties of the deep seabed polymetallic nodules,” in *18th International Conference on Transport and Sedimentation of Solid Particles.*, Prague, Czech Republic, 2017. [Online]. Available: <https://www.researchgate.net/publication/319876340>
- [19] Green Car Congress, “BloombergNEF: battery metals rebounding; by 2030, annual Li-ion battery demand to pass 2TWh,” 7 2021. [Online]. Available: <https://www.greencarcongress.com/2021/07/20210701-bnef.html>
- [20] IEA, “The Role of Critical World Energy Outlook Special Report Minerals in Clean Energy Transitions,” Paris, Tech. Rep., 2021. [Online]. Available: <https://www.iea.org/reports/the-role-of-critical-minerals-in-clean-energy-transitions>
- [21] J. L. Mero, “Chapter 11 Economic Aspects of Nodule Mining,” *Elsevier Oceanography Series*, vol. 15, no. C, pp. 327–355, 1977.
- [22] K. A. Miller, K. F. Thompson, P. Johnston, and D. Santillo, “An Overview of Seabed Mining Including the Current State of Development, Environmental Impacts, and Knowledge Gaps,” University of Exeter, Exeter, United Kingdom, Tech. Rep., 2018. [Online]. Available: <https://www.frontiersin.org/article/10.3389/fmars.2017.00418>
- [23] J. R. Hein, “Manganese nodules,” in *Encyclopedia of Earth Sciences Series*. Springer Netherlands, 2016, vol. Part 2, pp. 408–412.
- [24] ISA, “Polymetallic nodule mining technology: Current trends and challenges Ahead,” National institute of ocean technology, Chennai India, Tech. Rep., 2008. [Online]. Available: <http://www.isa.org.jm/files/documents/EN/Workshops/Feb2008/Backgrd.pdf>
- [25] U. von Stackelberg and H. Beiersdorf, “The formation of manganese nodules between the Clarion and Clipperton fracture zones southeast of Hawaii,” *Marine Geology*, vol. 98, no. 2-4, pp. 411–423, 6 1991.
- [26] Global Sea Mineral Resources NV, “Environmental Impact Statement,” Tech. Rep., 2018.

- [27] J. van Wijk, "Vertical Hydraulic Transport for deep sea mining a study into flow assurance," Ph.D. dissertation, TU Delft, 2016.
- [28] P. Weaver, c. Mohn, J. Tougaard, K. Gustavson, M. Koepcke, S. Wegeberg, L. De Jonge, and M. Lavaleye, "Blue Nodules Deliverable report D5.1 Report on inventory of environmental pressures Deliverable Report," The European Union framework programme for research and innovation, Tech. Rep., 2016.
- [29] H. Sup, K. Hyung-Woo, Y. Taekyung, C. Jong-Su, L. Tae Hee, and L. Jong-Kap, "Technologies for Safe and Sustainable Mining of Deep-Seabed Minerals," in *Environmental Issues of Deep-Sea Mining: Impacts, Consequences and Policy Perspectives*, R. Sharma, Ed. Cham: Springer International Publishing, 2019, pp. 95–143. [Online]. Available: https://doi.org/10.1007/978-3-030-12696-4_5
- [30] P. Hu, M. Placidi, H. Santo, and R. Shenoi, "Feasibility study on manganese nodules recovery in the Clarion-Clipperton Zone," Tech. Rep., 2012. [Online]. Available: <https://www.researchgate.net/publication/270570430>
- [31] S. Liao, "A buoyancy vertical transport system of deep-sea mining," *Journal of Ocean Engineering and Science*, vol. 5, no. 3, pp. 294–295, 9 2020.
- [32] R. Helmons, "Lecture Vertical Transportation," TU Delft, 2019.
- [33] T. Brockett, "Nodule collector subsystem," international Seabed Authority, Kingston, Tech. Rep., 10 1999.
- [34] W. Ma, C. van Rhee, and D. Schott, "Technological and profitable analysis of airlifting in deep sea mining systems," *Minerals*, vol. 7, no. 8, 8 2017.
- [35] J. M. van Wijk, S. Haalboom, E. de Hoog, H. de Stigter, and M. G. Smit, "Impact fragmentation of polymetallic nodules under deep ocean pressure conditions," *Minerals Engineering*, vol. 134, pp. 250–260, 4 2019.
- [36] J. M. van Wijk and E. de Hoog, "Size reduction of CCZ polymetallic nodules under repeated impact fragmentation," *Results in Engineering*, vol. 7, p. 100154, 9 2020.
- [37] J. S. Chung, International Society of Offshore and Polar Engineers., and H. Thiel, *Deep seabed mining environment : preliminary engineering and environmental assessment*. International Society of Offshore and Polar Engineers, 2002.
- [38] S. E. Volkmann and F. Lehnen, "Production key figures for planning the mining of manganese nodules," *Marine Georesources and Geotechnology*, vol. 36, no. 3, pp. 360–375, 4 2018.
- [39] M. Knight, J. Wates, and L. du Plessis, "Application of hydrocyclone technology to tailings storage facilities to reduce water consumption," in *Proceedings of the 15th International Seminar on Paste and Thickened Tailings*. Australian Centre for Geomechanics, Perth, 2012, pp. 233–241.
- [40] Y. Park, C. Yoon, Y. Kim, D. Lee, J. Park, and International Society of Offshore and Polar Engineers., "Separation of Manganese Nodules from Solid-liquid Mixture Using

Hydrocyclone,” Korea Institute of Geoscience and Mineral Resources, KIGAM, Daejeon, Tech. Rep., 7 2007.

- [41] T. Sparks and G. Chase, “Section 1 - Filtration – Introduction, Physical Principles and Ratings,” in *Filters and Filtration Handbook (Sixth Edition)*, T. Sparks and G. Chase, Eds. Oxford: Butterworth-Heinemann, 2016, pp. 1–54. [Online]. Available: <https://www.sciencedirect.com/science/article/pii/B9780080993966000010>
- [42] A. S. Patra, D. Makhija, A. K. Mukherjee, R. Tiwari, C. R. Sahoo, and B. D. Mohanty, “Improved dewatering of iron ore fines by the use of surfactants,” *Powder Technology*, vol. 287, pp. 43–50, 1 2016.
- [43] L. Besra, B. P. Singh, P. S. Reddy, and D. K. Sengupta, “Influence of surfactants on filter cake parameters during vacuum filtration of flocculated iron ore sludge,” *Powder Technology*, vol. 96, no. 3, pp. 240–247, 5 1998.
- [44] M. Le Roux, Q. P. Campbell, M. S. Watermeyer, and S. De Oliveira, “The optimization of an improved method of fine coal dewatering,” *Minerals Engineering*, vol. 18, no. 9, pp. 931–934, 8 2005.
- [45] K. Keller and W. Stahl, “Vibration dewatering,” *Chemical Engineering and Processing: Process Intensification*, vol. 33, no. 5, pp. 331–336, 11 1994.
- [46] Y.-C. Park, C.-H. Yoon, D.-K. Lee, and S.-K. Kwon, “Design of Hydrocyclone for Solid Separation,” Korea Institute of Geoscience and Mineral Resources, Tech. Rep., 2005. [Online]. Available: <http://onepetro.org/ISOPEOMS/proceedings-pdf/OMS05/All-OMS05/1846390/isope-m-05-023.pdf>
- [47] R. Salmimies, J. Kallas, B. Ekberg, and A. Häkkinen, “Scale Growth in the Dewatering of Iron Ore,” *International Journal of Mining Engineering and Mineral Processing*, vol. 1, no. 2, 8 2012.
- [48] Z. H. Wu, Y. J. Hu, D. J. Lee, A. S. Mujumdar, and Z. Y. Li, “Dewatering and drying in mineral processing industry: Potential for innovation,” *Drying Technology*, vol. 28, no. 7, pp. 834–842, 7 2010.
- [49] J. Neizvestnov and A. Kondratenko, “Engineering Geology of the ClarionClipperton Ore Province in the Pacific Ocean,” Nauka, Sankt Petersburg, Tech. Rep., 2004.
- [50] G. P. Glasby, *Marine Manganese Deposits*. Elsevier Science & Technology, 1977.
- [51] J. Zenhorst, “Degradation of poly-metallic nodules in a dredge pump Section of Dredging Engineering,” Master’s thesis, TU Delft, Delft, 2016.
- [52] P. Halbach and R. Fellerer, “The Metallic Minerals of the Pacific Seafloor,” *GeoJournal*, vol. 4, no. 5, pp. 407–421, 1980. [Online]. Available: <http://www.jstor.org/stable/41142465>
- [53] J. T. M. Wijnands, “Particle Degradation during Vertical Transportation Contribution of Abrasive Wear on Polymetallic Nodule Degradation,” Master’s thesis, TU Delft, Delft, 2018. [Online]. Available: <http://repository.tudelft.nl/>.

- [54] S. Miedema, *The Delft Sand, Clay & Rock Cutting Model.*, 3rd ed. Delft: TU delft Open, 10 2019.
- [55] V. Matousek, “Dredge pumps and slurry transport. Lecture notes OE44035. TU Delft,” Delft, 2004.
- [56] A. Phillip Grima and P. Wilhelm Wypych, “Discrete element simulations of granular pile formation,” *Engineering Computations*, vol. 28, no. 3, 4 2011.
- [57] M. Mohajeri, “Grabs and Cohesive Bulk Solids: Virtual prototyping using a validated co-simulation,” Ph.D. dissertation, TU Delft, Delft, 2021. [Online]. Available: <https://doi.org/10.4233/uuid:b232e542-4881-4b02-8677-a7b1dd37b6b0>
- [58] Z. X. Yang, J. Yang, and L. Z. Wang, “On the influence of inter-particle friction and dilatancy in granular materials: a numerical analysis,” *Granular Matter*, vol. 14, no. 3, pp. 433–447, 2012. [Online]. Available: <https://doi.org/10.1007/s10035-012-0348-x>
- [59] R. Kumar, W. Ketterhagen, A. Sarkar, J. Curtis, and C. Wassgren, “Breakage modeling of needle-shaped particles using the discrete element method,” *Chemical Engineering Science: X*, vol. 3, 8 2019.
- [60] Y. Li, K. Liang, H. Dai, and C. Zhang, “Degradation of Polymetallic Nodules in Deep-Sea Multi-Stage Lifting Motor Pump,” *Minerals*, vol. 11, no. 6, 2021. [Online]. Available: <https://www.mdpi.com/2075-163X/11/6/656>
- [61] J. Bridgwater, “Chapter 3 Particle Breakage due to Bulk Shear,” *Handbook of Powder Technology*, vol. 12, pp. 87–116, 1 2007.
- [62] R. W. Boulanger, M. Asce, and I. M. Idriss, “Liquefaction Susceptibility Criteria for Silts and Clays,” *Journal of Geotechnical and Geoenvironmental Engineering*, pp. 1413–1426, 2006.
- [63] K. A. Kwa, “A soil mechanics study into the liquefaction of shipped metallic ores,” School of Civil Engineering, University of Sydney, Tech. Rep., 2017. [Online]. Available: <https://www.researchgate.net/publication/320164068>
- [64] Global Sea Mineral Resources NV, “Environmental Impact Statement,” DEME Group, Tech. Rep., 4 2018.
- [65] A. Paixão, R. Resende, and E. Fortunato, “Photogrammetry for digital reconstruction of railway ballast particles – A cost-efficient method,” *Construction and Building Materials*, vol. 191, pp. 963–976, 12 2018.
- [66] C. J. Coetzee, “Calibration of the discrete element method and the effect of particle shape,” *Powder Technology*, vol. 297, pp. 50–70, 9 2016.
- [67] Z. K. Feng, W. J. Xu, and R. Lubbe, “Three-dimensional morphological characteristics of particles in nature and its application for DEM simulation,” *Powder Technology*, vol. 364, pp. 635–646, 3 2020.
- [68] S. Pargalgauskas, “The Influence of Particle Shape on the Sliding Wear of the Con-vox Pattern Surface A DEM Study,” Master’s thesis, TU Delft, 2021.

- [69] H. Salehi, M. Poletto, D. Barletta, and S. Larsson, “Predicting the silo discharge behavior of wood chips - A choice of method,” *Biomass and Bioenergy*, vol. 120, pp. 211–218, 1 2019.
- [70] T. Roessler, C. Richter, A. Katterfeld, and F. Will, “Development of a standard calibration procedure for the DEM parameters of cohesionless bulk materials – part I: Solving the problem of ambiguous parameter combinations,” *Powder Technology*, vol. 343, pp. 803–812, 2 2019.
- [71] S. M. Derakhshani, D. L. Schott, and G. Lodewijks, “Micro–macro properties of quartz sand: Experimental investigation and DEM simulation,” *Powder Technology*, vol. 269, pp. 127–138, 1 2015.
- [72] S. Lommen, M. Mohajeri, G. Lodewijks, and D. Schott, “DEM particle upscaling for large-scale bulk handling equipment and material interaction,” *Powder Technology*, vol. 352, pp. 273–282, 6 2019.
- [73] H. M. Beakawi Al-Hashemi and O. S. Baghabra Al-Amoudi, “A review on the angle of repose of granular materials,” *Powder Technology*, vol. 330, pp. 397–417, 5 2018.
- [74] A. W. Roberts and S. J. Wiche, “Prediction of lining wear life of bins and chutes in bulk solids handling operations,” *Tribology International*, vol. 26, no. 5, pp. 345–351, 10 1993.
- [75] G. Chen, “Surface wear reduction of bulk solids handling equipment using bionic design,” Ph.D. dissertation, TU Delft, delft, 2017.
- [76] T. C. Blair and J. McPherson, “Grain-size and textural classification of coarse sedimentary particles,” *Journal of Sedimentary Research*, vol. 69, pp. 6–19, 1 1999.